TECHNISCHE UNIVERSITÄT WIEN
Vienna | Austria

DIPLOMARBEIT

High Power Polarized vs. Low Power Direct EDXRF

ausgeführt am

Atominstitut der Technischen Universität Wien
Stadionallee 2
1020 Wien

unter der Anleitung von
ao. Univ.Prof.i.R. Dipl.-Ing. Dr.techn. Peter Wobrauschek

durch
Ing. Peter Allinger, BSc
Lorettostraße 11
7053 Hornstein

Wien, 9. Dezember 2015

Abstract

The goal of this master thesis was to perform a direct comparison between modern and compact low power X-ray tubes and water cooled high power X-ray tubes with and without a secondary target. For future industrial applications a low power system would meet a great demand as a mobile and adaptable analysis system, if the achievable results can stand in competition to conventional and stationary high power facilities. For this reason such a low power system has been developed during one of my earlier project works. This facility consists of a AMPTEK Mini-X X-ray tube [1] with a maximum power of 4 watt in combination with a silicon drift detector (SDD) from KETEK [2] and is opposed by a water cooled SEIFERT 2.2 kilowatt high power tube with an optional secondary target made of molybdenum. Both tubes utilize a silver anode material.

During this thesis several improvements to the control software and the set-up were conducted. Some examples include the addition of a video stream window to display the webcam feed, an added KLM marker function for easier evaluation, a new mount and a prism for the high power tube and many more. Furthermore a user manual was composed to serve future users as a reference.

The efficiency of the low power system was verified by direct comparison in four different tests against the high power system with and without secondary target. Apart from a general test regarding geometry and count rates and two resolution tests, the last method was selected in regard to possible future applications in industrial forging or mill products.

Zusammenfassung

Ziel dieser Arbeit war es, einen direkten Vergleich zwischen modernen und kompakten Niederleistungsröhren im Watt Bereich und wassergekühlten Hochleistungsröhren mit und ohne Sekundärtarget durchzuführen. Für zukünftige industrielle Anwendungen wäre ein mobiles, anpassungsfähiges System wünschenswert, welches durch Niederleistungsröhren erreicht werden könnte, sofern die erreichbaren Ergebnisse mit stationärer Technik in Konkurrenz treten können. Dazu wurde in meiner vorangegangenen Projektarbeit eine solche Niederleistungsmesseinheit geschaffen, um diesen Vergleich durchführen zu können. Diese besteht aus einer AMPTEK Mini-X Röntgenröhre [1] mit einer Leistung von 4 Watt in Kombination mit einem Silizium Drift Detektor (SDD) von KETEK [2]. Dem gegenüber steht eine wassergekühlte SEIFERT 2.2 Kilowatt Hochleistungsröhre mit optionalem Sekundärtarget aus Molybdän. Beide Röhren verwenden eine Silberanode.

Im Laufe der Arbeit mussten zahlreiche Verbesserungen sowohl an der selbst geschriebenen Software, als auch am Aufbau durchgeführt werden. So erfolgte zum Beispiel die Einbindung eines Videofensters zur Anzeige der Webcam, eine KLM Marker Funktion um bessere Auswertung zu ermöglichen, eine neue Halterung und ein Prisma für die Hochleistungsröhre und vieles mehr. Darüber hinaus enstand ein Benutzerhandbuch, um zukünftigen Anwendern eine Hilfestellung zu geben und als Nachschlagewerk zu dienen.

Es wurden vier verschiedene Tests ausgewählt, um die drei oben erwähnten Methoden, also Niederleistungsröhre, Hochleistungsröhre mit Sekundärtarget und ohne, direkt vergleichen zu können. Neben der grundlegenden Geometrie und erreichbaren Zählraten dieser Methoden und zwei verschiedenen Tests zur Überprüfung der Auflösung, konnte in Zusammenarbeit mit der Industrie eine Anwendung im Bereich der Seigerungsverteilung in Schmiede- oder Walzerzeugnissen durchgeführt werden.

Acknowledgments

First and foremost I would like to thank *Ao.Univ.Prof.i.R. Dipl.-Ing. Dr.techn. Peter Wobrauschek* for his support and supervision during this thesis and his willingness to allow me great freedom in my time management.

Furthermore I wish to thank *Ao.Univ.Prof. Dipl.-Ing. Dr.techn. Christina Streli* and all the other members for welcoming me to the group and for many nice discussions and coffee breaks.

My special thanks goes to mister *Walter Klikovich* for his fast and precise work on all the many, many parts of this thesis that had to be fabricated along the way.

In addition I would like to thank *Andrzej Pelczar, Rainer Essbüchl, Maximilian Zach* from the electrical engineering department who helped and instructed me on several problems.

I would also like to give my gratitude to the people from *Breitenfeld Edelstahl AG*, *Dipl.-Ing. Andreas Graf, Ing. Wolfgang Spreitzhofer* and especially *Michael Handler* for their support in sample acquisition and many helpful discussions.

Last but not least I want to express my gratitude towards my family and my girlfriend for their support and patience with me. I could not have done it without them.

Contents

Chapter 1

Introduction

This work examines the method of high power energy dispersive X-ray fluorescence analysis (EDXRF) using a secondary target to obtain polarized radiation, resulting in a sophisticated background reduction when working in a triaxial orthogonal setup, but comes at the expense of beam power and very poor efficiency and compares it to modern, low power, peltier cooled x-ray tubes.

Both methods certainly have their specific advantages and disadvantages and present the user with a number of possibilities and exploits to optimize and improve their capabilities in energy dispersive x-ray fluorescence spectrography.

In the following chapters I will give a short introduction to the used setup and equipment, a detailed theoretical background on various EDXRF specific topics, such as x-ray tubes, electron and x-ray surface interaction, silicon drift detectors, spectroscopic filters, the use of a secondary target, misleading spectrographic artifacts and finally the results of several measurements designed to compare the methods mentioned above.

In addition the software package for motion control, measuring cycle and spectrum evaluation was modified and extended during this thesis to provide the user with additional tools and provide a better user experience. Controllable conditions for sample illumination and CCD camera imaging was achieved by modern electronic devices and can now be adjusted directly through the software.

Chapter 2

Theory

120 years ago in 1895 Wilhelm Conrad Röntgen started with his announcement of the discovery of X-rays in his publication "'*Über eine neue Art von Strahlen*"' [3] a century full of important discoveries and inventions around a whole new field of physics. For this achievement he was awarded the first Nobel price in physics in 1901 [4]. Only two years later another Nobel price was shared by Pierre and Maria Sklodowska Curie for their joint researches on the phenomena and Henri Antoine Becquerel for the discovery of spontaneous radioactivity [5]. 1913 William David Coolidge used one of his achievements, the ductile tungsten, to create the Coolidge X-ray tube [6]. His invention favors a tungsten filament cathode and a water cooled target anode to create continuous high power X-rays and his concept it still used in modern tubes.
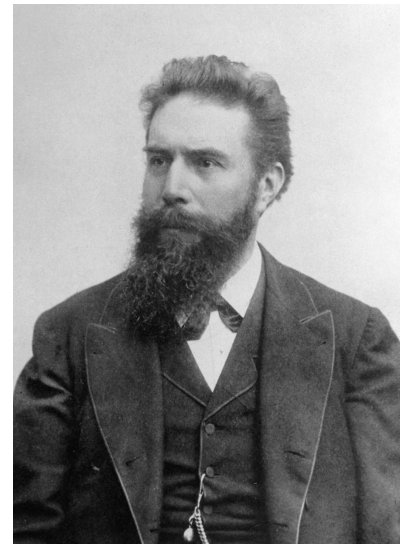
Figure 2.1: W. C. Röntgen

In the same year Henry Moseley concluded in his work "'*The high frequency spectra of the elements*"' [7], that the wavelength of the characteristic X-rays is dependent on the atomic number of the elements, which is commonly known as Moseley's law. Inspired by the work of Max von Laue on the diffraction of X-rays by crystals for which he was awarded the Nobel price in physics in 1914 [8], sir Lawrence Bragg and

his father sir William Bragg received the Nobel price in physics one year later [9] for their services in the analysis of crystal structure by means of X-rays during which they derived the famous Bragg equation $n \cdot \lambda = 2d \cdot sin(\theta)$.

Three more important discoveries contributed to the basic theory of x-ray physics and were awarded a Nobel price. Charles Glover Barkla (Nobel price in physics 1917 [10]) discovered the characteristic X-rays of the elements and thus encouraged Niels Bohr (Nobel price in physics 1922 [11]) to formulate Bohrs atomic model as well as the so called Aufbauprinciple [12] and the quantum mechanical correspondence principle that justifies the classical approach in the limit of large quantum numbers. Manne Siegbahn (Nobel price in physics 1924 [13]) finally introduced a common formalism, the Siegbahn notation, for describing the spectral lines characteristic for each element and shell transition.

The following sections will provide the reader with a short introduction to the creation of X-rays, their interaction with matter, their detection and the final section will cover the methods of quantitative X-ray analysis. It shall be mentioned that the description of most of the theoretical background is closeley related to the excellent books: *Handbook of Practical X-ray Fluorescence Analysis* [14], *Handbook of X-Ray Spectrometry* [15] and *Elements of Modern X-ray Physics* [16].

2.1 Creation of X-rays

X-rays are located between the ultraviolet and gamma regime of the spectrum with a bit of an overlap on both sides from approximately 80nm(15eV) to 1fm (1.2MeV). The main physical phenomena used to create x-rays are radioactive decay (subsection 2.1.2) and the interaction of electrons with matter (subsection 2.1.1) or magnetic fields (subsection 2.1.3).

Wavelength

| 1 μm | 100 nm | 10 nm | 1 nm | 100 pm | 10 pm | 1 pm | 100 fm |

visible light   soft X–rays   gamma rays

ultraviolet light   hard X–rays

| 1 eV | 10 eV | 100 eV | 1 keV | 10 keV | 100 keV | 1 MeV | 10 MeV |

Photon energy
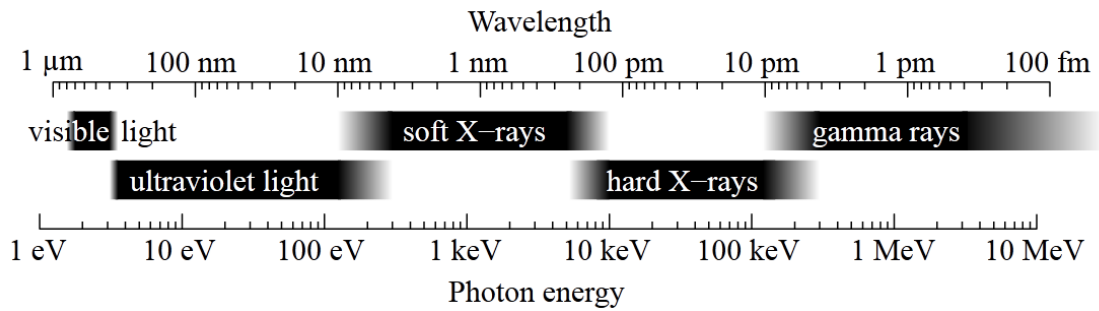
Figure 2.2: **Illustration of the electromagnetic spectrum**

X-rays are located between ultraviolet light on the low energy regime
and gamma radiation in the high energy sector, with a bit of an overlap
on both sides. (image from [17])

An electron interacting with matter may create two different kinds of spectral ra-
diation distribution. The first process is a result of the slowing down process of
the electron (or any other charged particle) by the Coulomb field of an Atom and
referred to as bremsstrahlung. The kinetic energy loss results in a continuous radia-
tion spectrum limited by the maximum energy $E_{kin} = e \cdot U$ and therefore a minimum
wavelength of $\lambda_{min} = ch/E_{kin}$ where c stands for the velocity of light in the vacuum
($c \approx 3 \cdot 10^9$ m/s), h for Planck's constant ($h \approx 6.626 \cdot 10^{-34} J \cdot s$), e is the electrical
charge ($e \approx 1.602 \cdot 10^{-19}$ C) and U the applied potential. This relation is usually
refered to as the Duane-Hunt law [18]. According to [16] the probability for the
emission of bremsstrahlung can be approximated by formula 2.1 which has a strong
dependence on the atomic number Z of the target element and the charge q of the
interacting particle.

$$\frac{q^2 \cdot Z^2 \cdot E_{kin}}{m_0^2} \tag{2.1}$$

Kulenkampff found in his extensive work [19] the following empiric formula (2.2)
for the description of the energy distribution of bremsstrahlung generated in a thick
target sample. As the second term in equation 2.2 is usually small and neglected,
the energy distribution $I(\nu)d\nu$ is mainly proportional to the atomic number Z of the

element and the difference between between the frequency ν and it's minimum ν_0 determined by equation 2.1. a and b are independent constants and n the impinging electron.

$$I(\nu)\mathrm{d}\nu = n\left[aZ(\nu_0 - \nu) + bZ^2\right] \tag{2.2}$$

Building on the work of Kuhlenkampff, Wentzel and Kramers formulated the following approximations of the spectral energy distribution in the limit of thin film (2.3) and thick film (2.4) samples, where A is the atomic mass, V_0 the kinetic energy of the impinging particle (usually an electron) and l is a constant usually set to 6.

$$
\begin{aligned}
I(\nu)\mathrm{d}\nu &= \frac{16\pi^2 \cdot A \cdot Z^2 \cdot e^5}{3\sqrt{3} \cdot m_0 \cdot V_0 \cdot c^3}\mathrm{d}\nu, \quad \nu < \nu_0 \\
I(\nu)\mathrm{d}\nu &= 0, \qquad\qquad\qquad\quad \nu > \nu_0
\end{aligned} \tag{2.3}
$$

$$I(\nu)\mathrm{d}\nu = \frac{8\pi \cdot e^2 \cdot h}{3\sqrt{3} \cdot l \cdot m_0 \cdot c^3}Z(\nu_0 - \nu)\mathrm{d}\nu \tag{2.4}$$

These basic approximations described by Kramer's law represent a fast and easy way to estimate the spectral intensity distribution but they neglect several effects such as self-absorption or electron backscattering. A lot of effort was put into an accurate description of the spectral intensity distribution as they are necessary for applying fundamental parameter methods and extracting the background caused by bremsstrahlung [15].

On the other hand an incoming particle might eject an inner shell electron of an atom. The resulting vacancy is filled by one or more successive transitions of outer shell electrons, which emit their excess energy in the form of so called characteristic radiation, that is specific for each element and shell transition. Manne Siegbahn was the first to present a system for the classification of these transitions. For example, an electron transition from the M to the K shell is called a $K\beta$ transition. The first letter represents the vacancy that is filled, the following Greek letter defines the origin of the electron (L=α, M=β and so forth) and an optional number would represent the subshell. Although the Siegbahn notation is still widely used, the International Union of Pure and Applied Chemistry (IUPAC) recommended another system in 1991 [20].
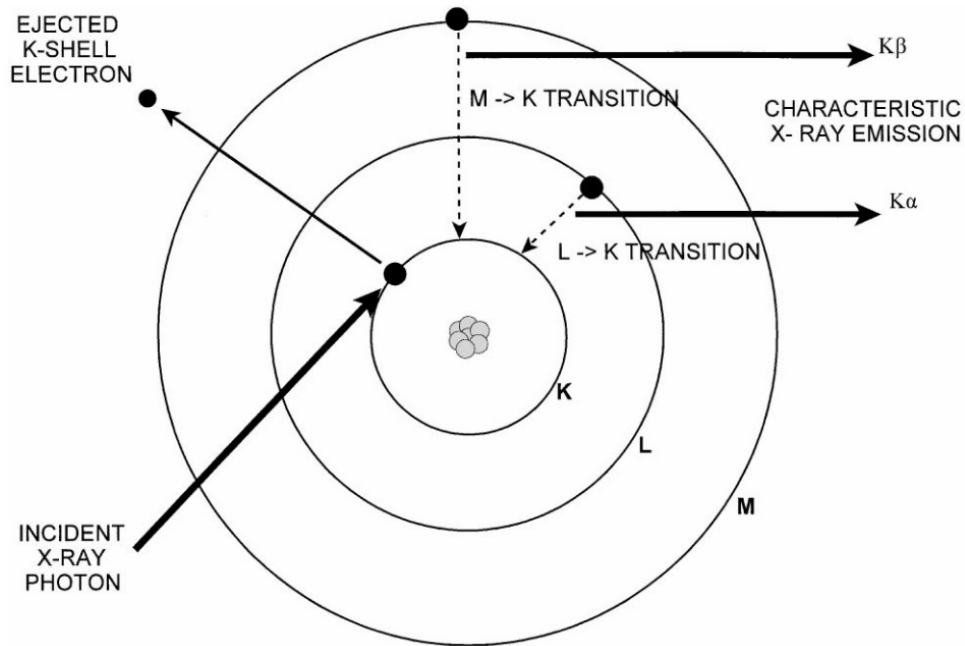
Figure 2.3: **Principle of XRF:** An X-ray of high enough energy excites an inner shell electron resulting in the emission of characteristic radiation as the vacancy is filled by an electron from an outer shell [21].

According to Moseley's law [7] the frequency ν of a x-ray photon emitted during the transition of an electron between two atom shells n_1 and n_2 can be calculated by equation 2.5. In this formula R_∞ stands for Rydbergs constant, m_e for the electron mass, Z is the effective charge and S the screening constant dependent on the involved shells in the transition.

$$\nu = \frac{c}{\lambda} = \frac{c \cdot R_\infty}{1 + \frac{m_e}{M}} \cdot (Z - S)^2 \cdot \left(\frac{1}{n_1^2} - \frac{1}{n_2^2} \right) \tag{2.5}$$

However not all shell transitions are allowed and observed. The transitions with the highest probability are the so called dipole transitions that follow the selection rules according to 2.6. Considering classical mechanics the first rule $\Delta l = \pm 1$ can be interpreted in such a way, that an angular momentum is transfered. These simple rules can be extended to describe electric and magnetic transitions of a higher order according to 2.7. In general magnetic transitions are less likely than electric ones

of the same order and magnetic transitions one order less than the corresponding electric ones usually compete against each other. For example M2 is less likely than E2 and competes with E3 transitions.

$$\Delta l = \pm 1, \quad \Delta m = 0, \ \pm 1 \quad \Big\} \quad \text{dipole} \tag{2.6}$$

$$\left.\begin{array}{ll} |I_i - I_f| \leq n \leq I_i + I_f & \\ \Pi_i \cdot \Pi_f = (-1)^n & \text{for E}n \\ \Pi_i \cdot \Pi_f = (-1)^{n+1} & \text{for M}n \end{array}\right\} \quad \text{multipole} \tag{2.7}$$

Especially in the low Z regime another process has to be taken into account. The Auger effect discovered by Pierre Victor Auger [22], is a competitive process to the emission of characteristic X-rays. A vacancy created by an impinging particle in the inner shell of the atom can be either filled with an electron from a higher shell with the excess energy released as a X-ray or an electron from an intermediary shell can fill the hole in the lower shell, while an outer electron is ejected to satisfy the conservation of energy. This electron is then referred to as Auger electron. Figure 2.4 depicts the probability for the emission of an Auger electron or characteristic radiation in relation to the atomic number for the two lowest shell combinations and suggests a break even point at Z≈32.
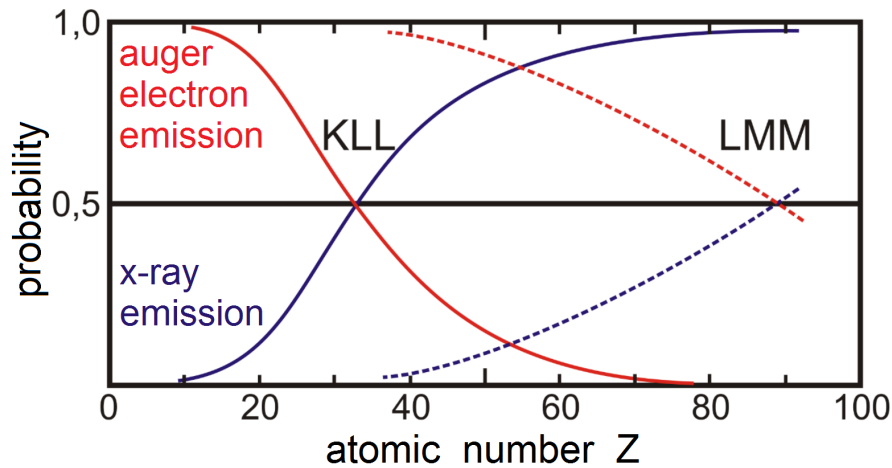
Figure 2.4: **Auger versus X-ray emission probability**

> The probability of emission for characteristic radiation compared to auger electron emission is depicted as a function of the atomic number Z for two different shell transition combinations. The auger effect will dominate until approximately Z=32 for KLL transitions. (image from [23])

2.1.1 X-ray tubes

After the first experiments with X-rays by W. C. Röntgen, W. D. Coolidge invented the Coolidge tube [6], an improvement to the far less effective Hittorf-Crooks tube, in 1913. This basic design is still widely used and usually referred to when mentioning a X-ray tube. All tube designs feature some sort of electron generating electrode and a target anode where several processes as a result of the electron bombardment can occur. Only a small amount of the impinging electrons contributes to the generation of continuous bremsstrahlung and characteristic radiation. Figure 2.5 is an example of a basic or empty spectrum as a result of a direct measurement of the radiation generated by the tube. Such spectra consist of the background produced by bremsstrahlung and some few sharp line peaks representing the characteristic radiation induced by the target anode material. Other values such as form and

intensity, especially of the background, are a result of the high voltage and current applied to the tube.
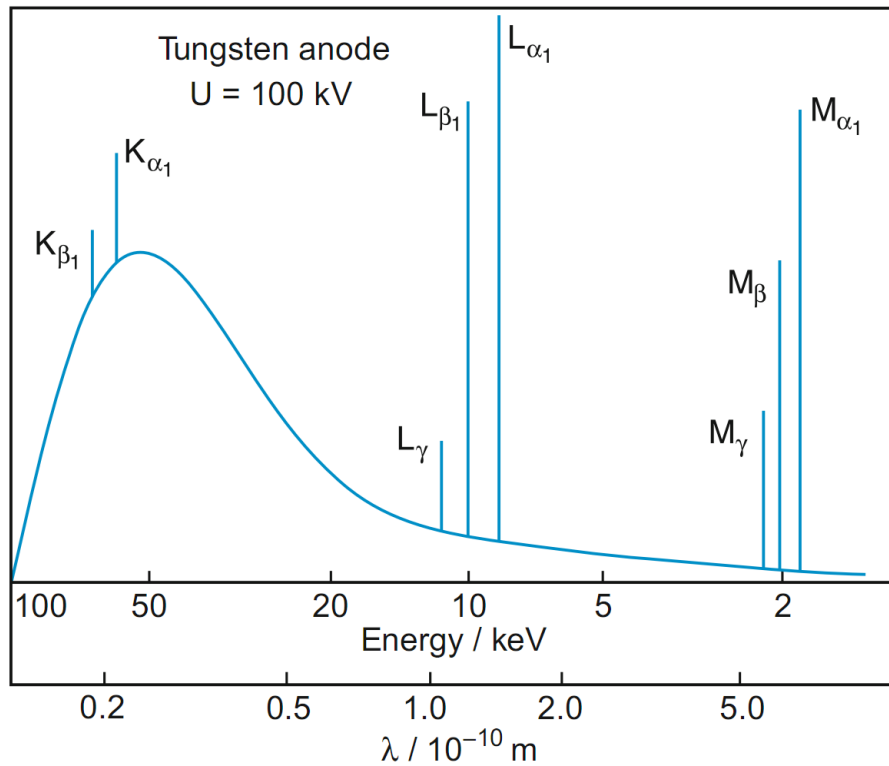
Figure 2.5: **Pure X-ray spectrum emitted by a tungsten anode**

This is a typical blank spectrum recorded directly in front of the exit window of a tungsten tube at 100kV. It is a combination of the background generated by bremsstrahlung and the characteristic lines of the anode material. The amount of bremsstrahlung generated is strongly dependent on the applied voltage. (image from [24])

Since the invention of the Coolidge tube more than 100 years ago a lot of effort was invested into the development and design of a wide variety of X-ray tubes ranging from small low power peltier cooled, to high power water cooled tubes that can even be further improved by the implementation of a rotating anode to increase heat dissipation for all kinds of different and specialized applications. In chapter 3.1 the

AMP-TEK [1] low power and Seiffert high power tube used during this thesis will be explained in greater detail.

Figure 2.6 depicts a standard X-ray tube with it's basic components. A Wehnelt electrode emits electrons in a focused beam onto the target material, which in this case is a tungsten disc embedded in a large copper part for better heat dissipation purposes. This target disc is tilted in such a way as to maximize the radiation output through a side window on the bottom of the picture. All parts are encased in an evacuated glass housing and in most cases with a very thin beryllium film covering the exit window to minimize absorption losses.
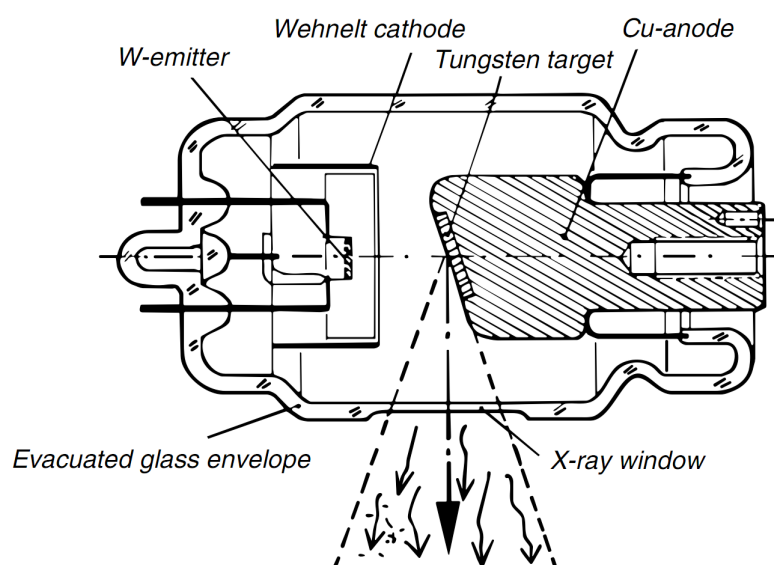

Figure 2.6: **Basic principle of a side window configuration X-ray tube**

An electron emitter in a Wehnelt configuration emits a focused beam onto the target material, in this case tungsten, embedded in a massive copper part for cooling purposes. The generated radiation can exit through a thin side window usually made of beryllium. (picture from [14])

Unfortunately an electron impinging on the target material of the X-ray tube will primarily introduce thermal energy to the anode. Only a small amount will con-

tribute to the generation of either continuous radiation (bremsstrahlung) or characteristic radiation. Equation 2.8 estimates the efficiency of such a tube, where C is a constant amounting to roughly 10^{-6} per kilo Volt, Z is the atomic number of the target material, U is the high voltage and I the current applied to the tube. This unfortunate relation makes it necessary to provide cooling for high power tubes and limits the maximum achievable radiation intensity of conventional tubes.

$$P = C \cdot Z \cdot I \cdot U^2, \qquad \eta \equiv \frac{P}{I \cdot U} \approx 10^{-6} \cdot Z \cdot U[kV] \qquad (2.8)$$

2.1.2 Radioisotope sources

Although more and more radioisotope sources can be replaced by modern low power tubes, there are still some areas where no other methods or instruments are applicable. This is due to the fact that radioisotope sources have some major advantages. They do not require electricity, are cheap, very small and lightweight, are independent from environmental conditions and continuously radiate, which is also one of their major drawbacks.

Radioactive decay can occur in 4 different processes. The α-decay (2.9) is characterized as the emission of an α-particle (or a ^4_2He core) and reduces the atoms mass number by 4 and atomic number by 2. There are furthermore two different kinds of β-decays, the β^--decay and the β^+-decay. While the β^--decay (2.11) raises the atomic number by one accompanied by the emission of an electron and anti-electron neutrino, the β^+-decay (2.11) reduces it by 1 while emitting a positron and an electron neutrino. In the last process the K capture (2.12), or electron capture, an atoms nucleus captures, hence the name, an electron and thus lowers its atomic number by one while emitting an electron neutrino.

$$^A_Z X \ \rightarrow \ ^{A-4}_{Z-2} Y \ + \overbrace{^4_2 He}^{\alpha} + \Delta E \qquad \alpha \text{ - decay} \qquad (2.9)$$

$$^A_Z X \ \rightarrow \ ^A_{Z+1} Y \ + \ e^- + \bar{\nu}_e \qquad \beta^- \text{ - decay} \qquad (2.10)$$

$$^A_Z X \ \rightarrow \ ^A_{Z-1} Y \ + \ e^+ + \nu_e \qquad \beta^+ \text{ - decay} \qquad (2.11)$$

$$^A_Z X + \ e^- \ \rightarrow \ ^A_{Z-1} Y \ + \ \nu_e \qquad \text{electron capture} \qquad (2.12)$$
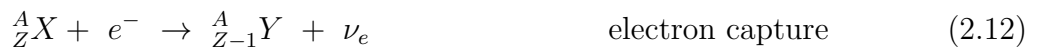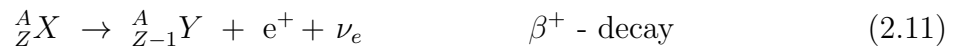
For XRF applications the radioisotope sources used are mainly γ emitters and sometimes β with a secondary target. Radioisotope sources are usually characterized by their activity, their half-life time, their emitted energy and of course the type of radioactive decay. The activity A of a radioactive material is described as the number of decays per time frame (2.13). Historically the first unit to describe the activity of an element *Curie* [Ci] was named after Maria and Pierre Curie, but was replaced by *Becquerel* [Bq], named after Henry Becquerel (1 Ci $= 3.7 \cdot 10^{10}$ Bq).

For the description of decay processes the radioactive decay law (2.14) calculates the number of remaining radioactive atoms of a given amount of a radioactive substance N_0 after a time t with the decay constant λ which is specific for each isotope. It is fairly easy to calculate the half-life time $T_{1/2}$ (2.15) after which half of the given number of radionuclides N_0 has decayed.

$$\text{A} = \frac{\mathrm{d}N}{\mathrm{d}t} \tag{2.13}$$

$$\text{N} = \text{N}_0 \cdot e^{-\lambda t} \tag{2.14}$$

$$\text{T}_{1/2} = \frac{\ln 2}{\lambda} \tag{2.15}$$

The selection of the right radioisotope is crucial, since to be able to excite a certain line of a given element, the radiation source must be able to supply an energy greater than the line energy plus the binding energy to be observed. Therefore a number of different isotope sources are available today to satisfy every need [25]. Figure 2.7 below depicts two different standard sizes and shapes of commonly used radioactive sources.

Some typical examples of sources used today are:

- Am^{241} 59.5 keV photon energy, α-decay

- Cd^{109} 22.1 keV photon energy, K-capture

- Fe^{55} 5.9 keV photon energy, K-capture

(a) disc source (b) ring source
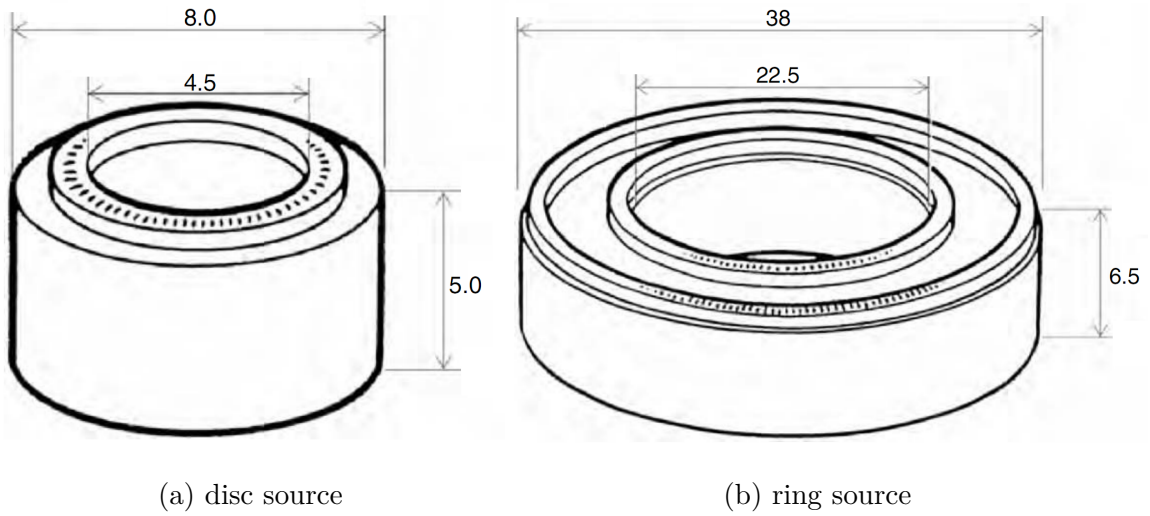
Figure 2.7: **Examples of standard radioisotope sources**

(a) typical disc source mostly used in applications that have a small window, for example silicon drift detectors. (b) ring sources are the most common, as they provide a higher photon flux. (image from [14])

2.1.3 Synchrotron radiation

Synchrotron radiation was first predicted by Ivanenko and Pomeranchuk [26] in 1944 as a result of fast moving particles on a circular orbit. Figure 2.8 explains the narrowing and focusing effect of the radiation emitted by a charged particle on a bent path according to the theory of special relativity. A particle on a bent or circular path is constantly exposed to radial acceleration and as a result will continuously radiate. At speeds much lower than the speed of light, such a particle will display a dipole radiation pattern and with increasing velocity will develop a strong constriction in forward direction tangential to it's orbit due to special relativity.
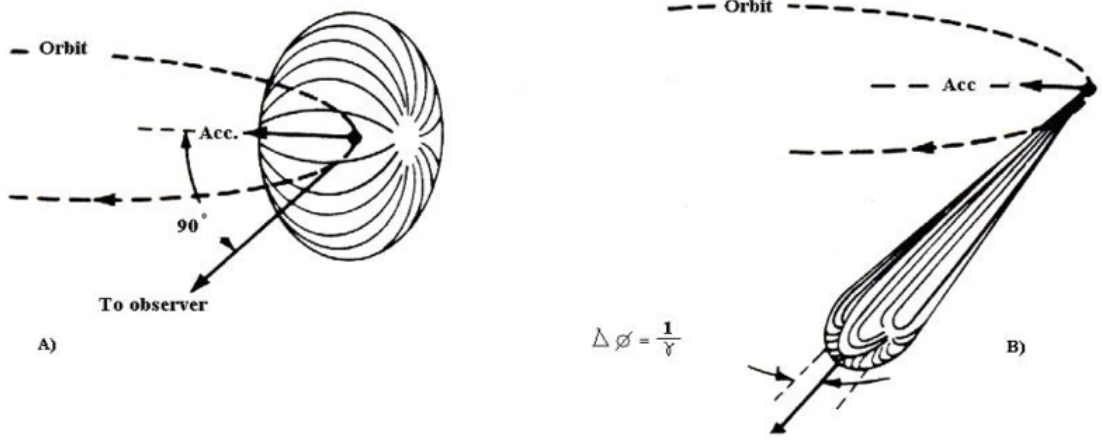
Figure 2.8: **Illustration of the synchrotron principle**

A carged particle on a bent path is subjected to accelleration and will constantly radiate. At speeds much lower than that of light (left) this will result in a dipole pattern, that will constrict in forward direction (right) with increasing velocity due to special relativity. (image from [17])

The opening angle of the beam can be calculated according to 2.16 and is an inverse function of the Lorentz-factor γ. A particle on a curved trajectory is subjected to energy loss, which in case of a circular orbit amounts to equation 2.17 for each circulation as a function of the charge of the particle $Z \cdot e$, again the Lorentz-factor γ, β is the ratio of the velocity divided by the speed of light, ϵ_0 the electric constant and R the radius of the orbit.

$$tan(\theta) = \frac{1}{\gamma} = \frac{m_0 \cdot c^2}{E}, \qquad\qquad \gamma = \sqrt{\frac{1}{1 - \frac{v^2}{c^2}}} \qquad (2.16)$$

$$\Delta E = \frac{(Ze)^2 \cdot \beta^3 \cdot \gamma^4}{\epsilon_0 \cdot 3R}, \qquad\qquad \beta = \frac{v}{c} \qquad (2.17)$$

While first experiments used the synchrotron radiation as a byproduct of particle accelerators, today dedicated and highly specialized facilities such as the European

Synchrotron Radiation Facility (ESRF) [27] are in use and enjoy a high degree of popularity for a multitude of applications.

Some of the major properties of synchrotron radiation are:

- very broad and continuous spectrum ranging from IR over UV and deep into hard X-rays

- High flux

- High stability

- High brilliance

- Polarization

- Pulsed time structure

There are three main insertion devices that further increase specific properties of synchrotron radiation: a Wiggler, an Undulator and a wavelength shifter. The Wiggler is used to produce a continuous spectrum with a high intensity while the use of an Undulator will result in a line spectrum. Another distinction between these two devices is given by the Undulator coefficient K that describes the amplitude of the electron oscillations according to equation 2.18, where e is the electric constant, m the mass, c the speed of light in the vacuum, B represents the magnetic field strength and λ_u the undulating period. This last parameter, the undulating period is defined as the distance after which the original magnetic field strength is reached. A K value greater than 1 describes a Wiggler, otherwise an Undulator. Equation 2.19 calculates the wavelength of the emitted radiation in case of an Undulator, where θ stands for half of the opening angle of the emitted radiation cone.

$$K = \frac{e \cdot B \cdot \lambda_u}{2\pi \cdot m \cdot c} \tag{2.18}$$

$$\lambda = \frac{\lambda_u}{2\gamma^2} \left[1 + \frac{K^2}{2} + (\theta\gamma)^2 \right] \tag{2.19}$$

2.2 Interaction
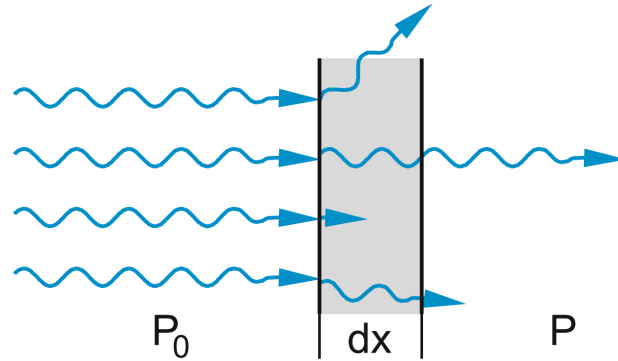
Figure 2.9: **Illustration of X-rays interacting with matter**

An X-ray beam with radiation power P_0 from the left when passing through a material with thickness dx is subject to scattering and/or absorption processes and exits with a certain lower power P to the right. (image from [24])

A parallel beam of X-ray radiation directed onto a material of thickness dx will be subject to several different processes. These effects can be divided into scattering (μ_s) and absorption (α) processes and can be combined to the attenuation coefficient μ (2.20). Figure 2.9 illustrates these effects: some rays are scattered, some absorbed and only a certain fraction of radiation power P passes through the target material according to equation 2.20. This relation is known as Beer-Lambert law.

$$\mathrm{d}P = -\mu P \mathrm{d}x, \qquad P(x) = P_0 \cdot e^{-\mu x}, \qquad \mu = \mu_s + \alpha \qquad (2.20)$$

Inelastic and elastic scatter processes are described by the scatter coefficient μ_s. While elastic scattering occurs when an incoming X-ray photon interacts with a tightly bound inner shell electron and conserves the photon energy, in an inelastic scatter process the energy is partially transfered to a free or outer shell electron.

The three main processes contributing to the absorption coefficient α are the photoelectric effect, the Compton effect and pair formation. First discovered in 1905 by

Albert Einstein [28] the photoelectric effect occurs when an impinging X-ray photon of the energy $h \cdot \nu$ is absorbed by an atom resulting in the ionization of an inner shell electron if the energy of the photon was equal or greater than the binding energy of the electron.

While the inelastic Compton effect is primarily a scatter process, the scattered photon may subsequently be absorbed via the photoelectric effect. This means, that an X-ray photon collides with an outer shell electron of an atom resulting in a division of it's energy between the scattered photon and the kinetic energy of the released electron and of course the binding energy. If the X-ray photon has at least two times the rest energy of an electron (~511 keV) it may interact with the nucleus of an atom and generate an electron positron pair. This process is called pair formation and is depicted in figure 2.10b along with the Compton effect (figure 2.10a).


(a) The Compton-effect   (b) Pair formation
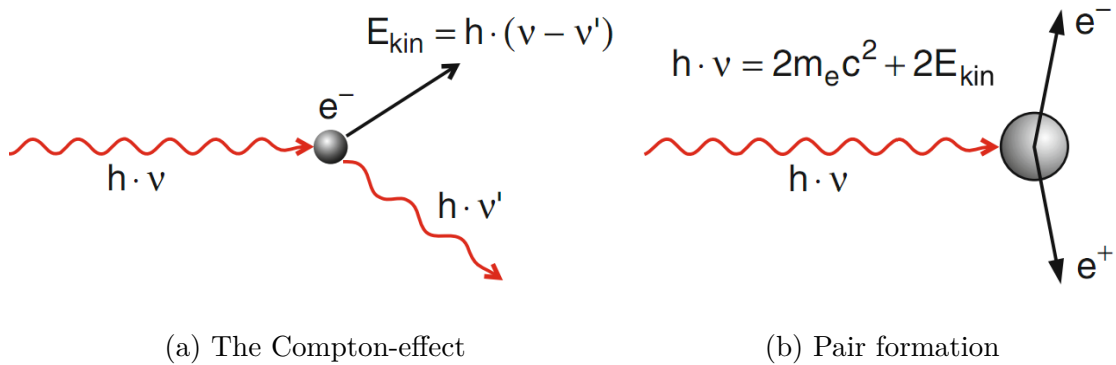
Figure 2.10: **Illustration of the Compton effect and pair formation**

(a) When an electron is hit by a X-ray photon of the energy $h \cdot \nu$ greater than the binding energy of the electron, the electron is ionized, the photon loses some energy in the scatter process and might get absorbed via the photoelectric effect. (b) When the incoming photon has at least twice the rest energy of an electron (~511 keV) it may create an electron positron pair. (image from [24])

All of the absorption processes described above are included in the absorption coefficient α, which is the product of the particle density n and the cross section of the absorption σ_a as described in equation 2.21 and is strongly dependent on the atomic number of the target material Z and the wavelength λ of the radiation.

$$\alpha = n \cdot \sigma_a, \qquad\qquad \sigma_a = C \cdot Z^4 \cdot \lambda^3 \qquad\qquad (2.21)$$
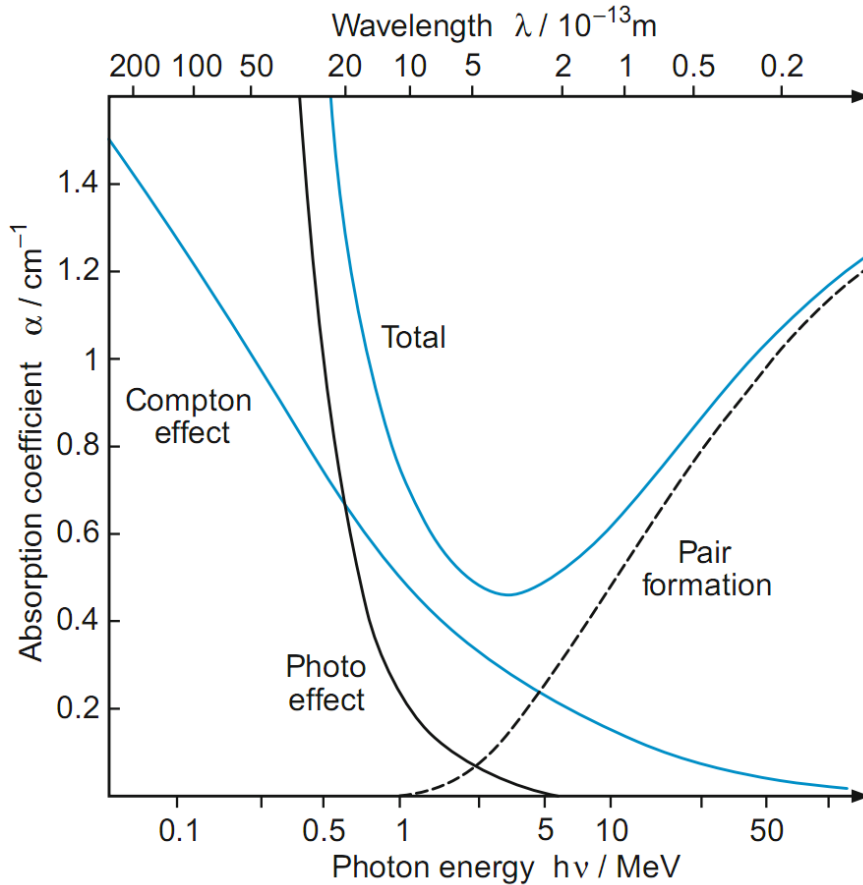
Figure 2.11: **Absorption coefficient as a function of the X-ray energy**

        The contributions of the three absorption processes, the Compton-effect, the photoelectric-effect and pair formation are a function of the X-ray energy and dominant in different energy regions. (image from [24])

The contribution of the different effects are illustrated in figure 2.11 and depend mostly on the photon energy of the radiation. For example pair formation can only occur above a certain energy threshold and will then increase in it's probability, while the other processes become far more likely, as the energy difference increases. However, the energy range relevant for XRF is on the very low end of this figure, as the important interactions take place below approximately 100keV.

Considering the shell structure of an atom, we find that each shell has a different binding energy for the electrons. The higher the order of the shell, the lower the energy required to ionize an electron. Furthermore, if we assign the quantum number n to the shells (K=1, L=2, M=3,...) then each shell consists of 2n-1 subshells with slightly different binding energies. This description of the atomic model is reflected in the behavior of the absorption coefficient α as depicted in figure 2.12. With increasing X-ray energy $h \cdot \nu$ the coefficient follows the predicted λ^3 trend, until the energy is high enough to ionize the electrons of the next shell or sub-shell. At this point called an absorption edge, the absorption coefficient experiences an immediate increase, because all the electrons of the corresponding shell can now contribute.
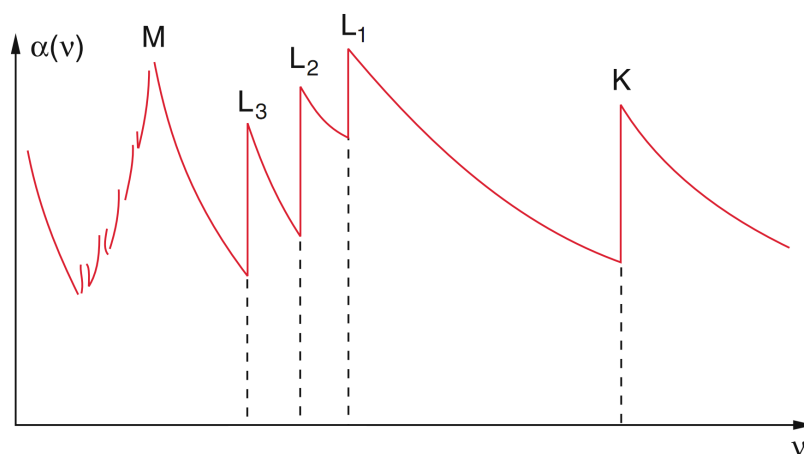

Figure 2.12: **Absorption coefficient with absorption edges**

Each shell or sub-shell of an atom is characterized by a certain binding energy that decreases with ascending order and results in so called absorption edges, where the absorption coefficient displays an immediate elevation. (image from [24])

2.3 Detection

This section will give a short overview of various available detection principles with a focus on silicon drift detectors (SDD) that were used during this thesis. A very detailed essay of numerous detector systems is given in [29].

One of the first detectors for X-rays is the proportional counter. It consists of a gas filled housing with an anode wire in the middle and a high voltage applied between them. An incoming particle may ionize an atom of the gas and thus creating an electron ion pair. This process will occur several times along the trajectory of the particle and due to the applied high voltage the electrons will drift towards the anode. When they reach a certain distance, a threshold from the anode, each electron will trigger an avalanche effect that results in a multiplication of the electrons in the immediate vicinity of the anode before they are detected. The registered signal is proportional to the energy of the impinging particle as it will take a certain amount of collisions and thus ionization processes to occur before the particle lost enough energy and is finally stopped. For electrons the amount of energy lost per ion pair formation is about 25-40 eV/ion-pair [29], which results in up to 40.000 collisions for a 1 MeV electron. Several other detectors like the gas detector, multiwire- or multi-strip detectors and the Geiger-Müller counter use roughly the same ionization and charge collection process and differ mostly in their application as position sensing devices or simple radiation detectors.

Scintillation detectors vary in such a way, that the interaction medium is not necessarily a gas, it can be a liquid or even a solid material and incoming radiation will rather excite the atoms of the detector material instead of ionizing them. This results in the emission of fluorescence light that is intensified by a photomultiplier tube and creates a signal proportional to the energy and intensity of the incident radiation.

Typical semiconductor detector materials are germanium (Ge) and silicon (Si). Up until now it is only possible to manufacture Ge of such a high purity (HPGe) necessary to achieve a sufficiently thick depletion depth. In case of Si it is still required to compensate for the usually boron (B) impurities, that act as acceptor atoms. A process called ion drifting is a common way to provide a sufficient amount of donor

atoms to achieve equilibrium. Lithium (Li) for example has only 1 electron in the 2s shell that will compensate the one electron of boron in the 2p shell and with a helium like core provides great diffusion properties through solids. This detectors are commonly called Si(Li) or Ge(Li) detectors.

The fabrication process is fairly easy and somewhat self balancing. At slightly elevated temperatures an excess of Li ions is incorporated into one side of the Si crystal, thus creating a n-type region on this side in opposition to a large p-type region on the other. After this first step the direction is reversed and the Li donor ions propagate due to the applied electric field into the p-type region. After a sufficient amount of time, as mentioned before, a self balancing effect will occur in which the space charge of the drifted region between the p- and n-type junction is effectively zero, because any net charge would result in further drifting until the net charge is zero again due to the applied electric field. With this process it is possible to achieve compensated regions up to 10mm thick for Si.

An example picture of the resulting p-i-n configuration (i=intrinsic) of such a lithium drifted silicon semiconductor is shown in figure 2.13. The concentration of Li donors in the intrinsic region is mostly constant and displays a linear gradient at the p- and n-type borders, which results in a positive charge density ρ on the n-side and a negative charge density on the p-side respectively. As a result, the applied electric field ϵ will drop sharply at the boundaries and the electric potential ϕ has a linear gradient in the compensated region.

Some of the major properties of Si(Li) detectors are that the lifetime of an ion pair created by an incoming particle in the intrinsic region is higher than the collection time and that the lower atomic number of Si over Ge shifts the optimum energy detection region to X-rays instead of γ-rays. Furthermore the larger bandgap of Si results in a smaller leakage current than in Ge. However both semiconductor detectors have to be cooled by liquid nitrogen, in order to reduce noise induced by fluctuations in the leakage current and to prevent thermal stresses and diffusion of lithium at room temperature.
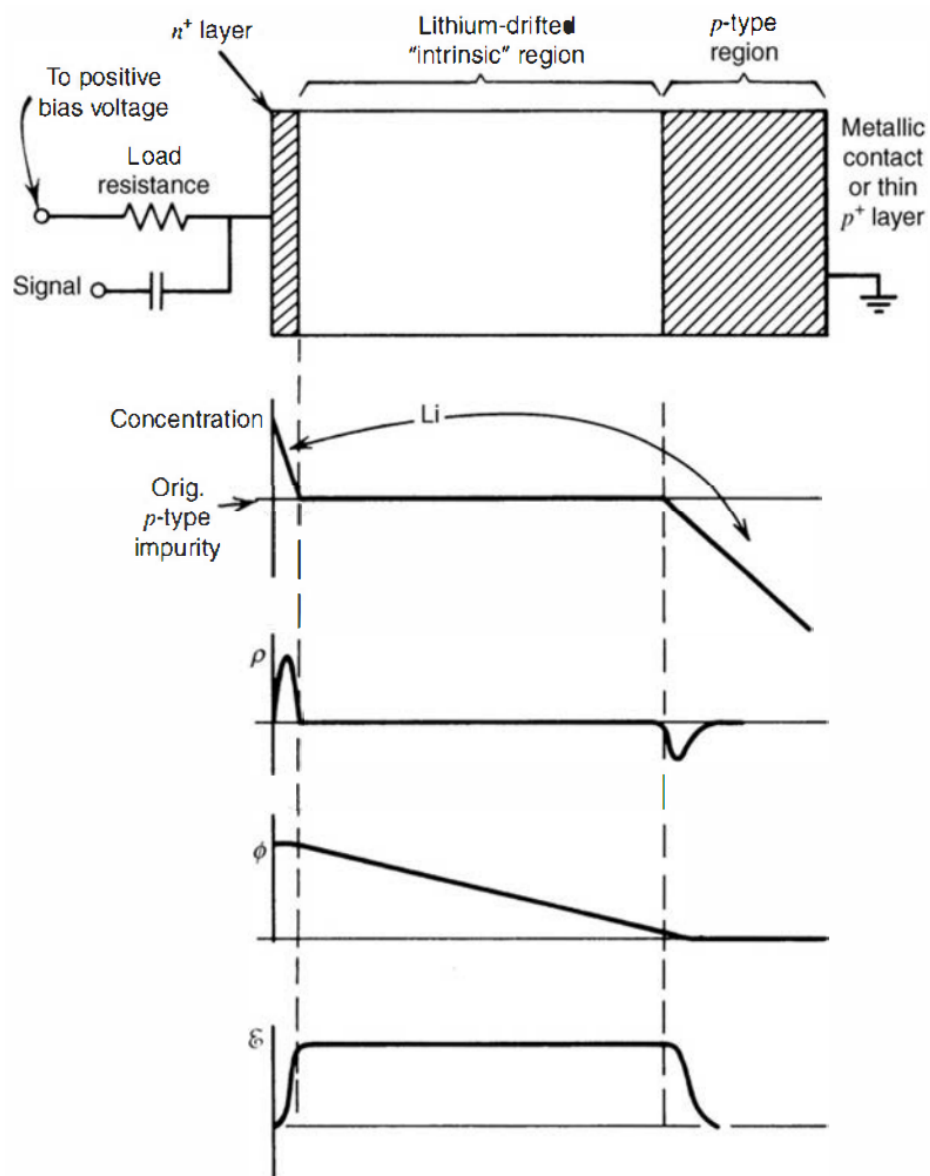
Figure 2.13: **Basic principle of a lithium drifted p-i-n junction detector**

The upper image depicts a simplified layout of the p-i-n configuration with a large compensated or intrinsic region in the middle. Below several distributions of various parameters such as the concentration of Li donors, the charge density ρ, the electric potential ϕ and electric field ϵ across the entire cross section are displayed. (image from [29])

A silicon drift detector (SDD) utilizes a special electrode arrangement to enable the position sensitive detection of ionizing radiation in two directions. Figure 2.14 illustrates a linear arrangement of anodes on both sides, connected with resistors to generate the required potential gradient that causes the electron generated by ionizing particles to drift parallel instead of perpendicular to the surface from their origin to an anode on one side. This anode can be divided into small multiple anodes to provide a second information of position. It has been shown that a spatial resolution of approximately $4\mu m$ can be achieved with this technique [30].
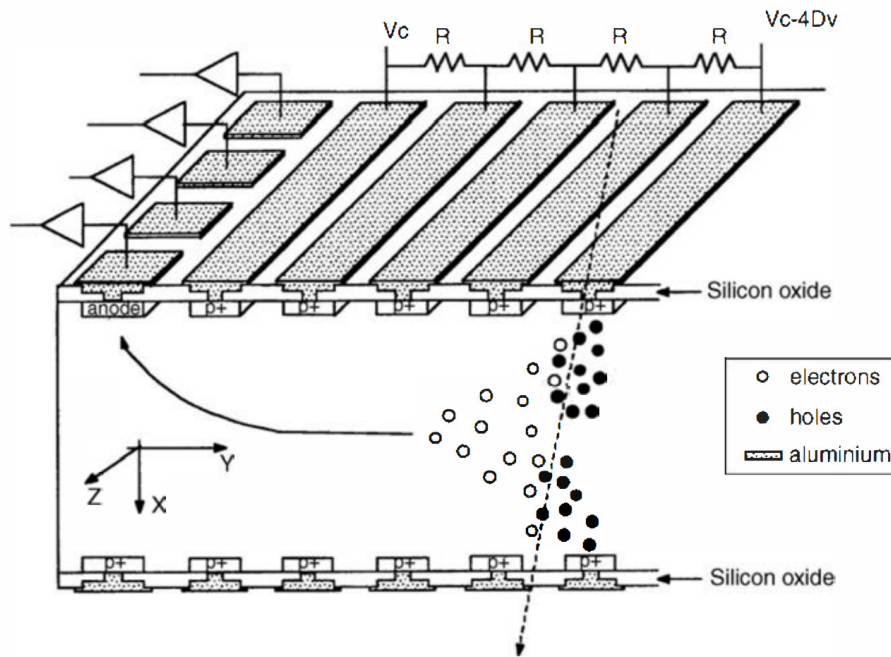
Figure 2.14: **Cross section of a linear silicon drift detector (SDD)**

An incident particle (dashed arrow) creates electron hole pairs that travel perpendicular to the surface to the collector anodes on the right. The Z resolution is limited by the spacing of the collector anodes and the Y position is a function of the drift time in the potential created by electrode strips on both sides. (image from [29])

Another possible configuration of an SDD is depicted in figure 2.15, where concentric
ring electrodes are regularly distributed on a circular dish with a collector anode
in combination with an on-chip junction field effect transistor (JFET). This com-
bination in addition to a very small anode design results in minimum capacitance,
which is a great advantage over regular Si(Li) detectors. This small capacitance is
a feature of great benefit, because is leads to a significant reduction in the noise
level. In comparison for an incident energy of 5.9 keV, a Si(Li) detector achieves an
energy resolution of 170 eV at -10°C [31], which is a temperature that is possible to
maintain via Peltier cooling on a SDD while providing a similar resolution. With
the loss of the need for liquid nitrogen cooling, SDD devices have been on the rise
in the last decades, especially for field applications and in other compact systems.
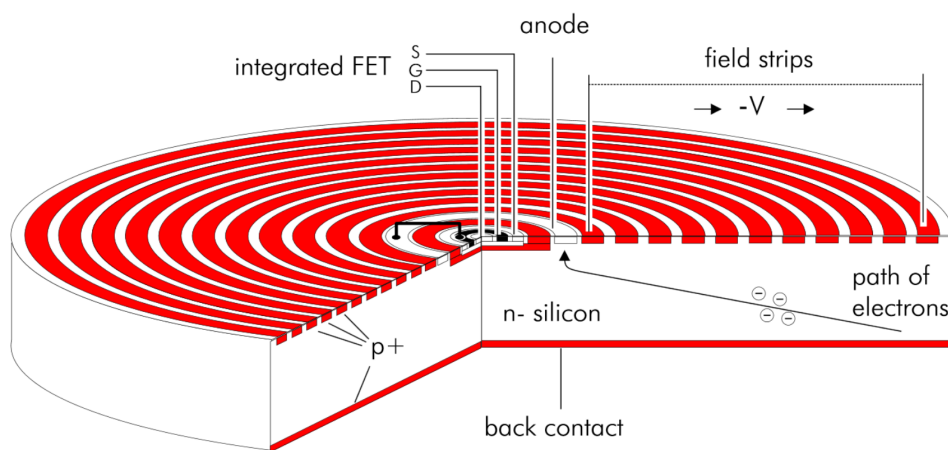

Figure 2.15: **Cross section of a circular silicon drift detector (SDD)**
In this configuration a small integrated JFET right next to a very thin
collector anode in the middle of concentric ring shaped electrodes has
the advantage of a very low capacitance that makes Peltier cooling a
viable option. (image from [31])

Some of the main features of modern silicon drift detectors are the excellent energy
resolution of 125eV at 5.9 keV, a high throughput of up to 1 million counts per
second and as mentioned before the lack for the need of liquid nitrogen cooling,
which allows such devices to be mounted in any direction.

2.4 Quantitative analysis

Quantitative analysis is a complex topic as it relies on a huge number of factors and effects. A lot of different empirical and theoretical methods for x-ray fluorescence analysis such as the fundamental parameter method, Monte-Carlo simulations and many more have been developed. In the following description only the very basics of the fundamental parameter method will be explained and are based on the very informative and detailed work of Wobrauschek [32] and Beckhoff et al. [14]. For a more detailed insight into the following topics those two sources are highly recommended. The last section will cover the empirical method as used in this thesis.

2.4.1 The fundamental parameter method

The fundamental parameter method (FP) derives it's name from the many basic physical parameters that are involved. A few examples are the attenuation coefficients, transition probabilities and fluorescent yield. Sherman [33] [34], as well as Shiraiwa and Fujino [35] derived the mathematical background and foundation for this method. It is a very difficult subject because so many effects have to be considered simultaneously, such as excitation of atoms and successive relaxation processes, absorption of radiation in the sample, corrections for matrix effects in the form of indirect excitation, the shape, thickness and the constitution of the sample and many more. Nonetheless it proved to be a viable theory and tool for the calculation of the elemental composition of various kinds of samples in the X-ray fluorescence analysis (XRF).

Figure 2.16 illustrates the geometry for the calculation of characteristic radiation with the fundamental parameter method according to equation 2.22. This fairly long and complicated formula can be separated into basically five different parts as indicated by braces.

An X-ray source generates a certain radiation of intensity $I_0(E_0)$ that is usually limited by apertures to a certain solid angle $d\Omega_1$. This beam enters the material under a certain angle ψ and travels through a certain depth x where it will interact with the atoms of the segment dx.

It is therefore necessary to calculate the attenuation of the beam for this distance $\frac{x}{sin(\psi)}$ represented by the red part of the formula.

The incoming radiation will lead to the uniform emission of a certain amount of fluorescence radiation in this differential element. The intensity of this radiation is dependent on several factors, such as the concentration W_i of the element i, the density ρ_s, the fluorescent yield $\omega_{i,j}$ of a certain shell j and finally the probability of each shell transition k $\rightarrow$ j for each given element i. Additionally the jump ratio between each shell j and i has to be taken into account by the factor $\left(1 - \frac{1}{r_{i,j}}\right)$ along with the photoelectric mass absorption coefficient $\left(\frac{\tau}{\rho}\right)_{i,E_0}$. All these relations together describe the formation of fluorescent radiation and are underbraced in equation 2.22.

However the uniformly emitted characteristic radiation will again travel through the material where it is attenuated as described by the blue part of the equation.

Finally it leaves the sample under a certain exit angle ϕ before a detector with efficiency $\epsilon_{E_{i,j,k}}$ will then register a fraction of the solid angle $\frac{d\Omega_2}{4\pi}$.

Everything taken together will finally yield the total intensity $I(E_{i,j,k})$ as a function of the respective energy specific for each element i and shell transition k $\rightarrow$ j.

$$I(E_{i,j,k}) = \underbrace{I_0(E_0) \cdot dE_0 \cdot d\Omega_1}_{primary\ beam} \cdot \underbrace{\overbrace{e^{-\left(\frac{\mu}{\rho}\right)_{s,E_0} \rho_s \frac{x}{sin(\psi)}}}^{\color{red}{incident\ beam}} \cdot \overbrace{e^{-\left(\frac{\mu}{\rho}\right)_{s,E_{i,j,k}} \rho_s \frac{x}{sin(\phi)}}}^{\color{blue}{emitted\ beam}}}_{attenuation} \cdot$$

$$\cdot \underbrace{\left[W_i \frac{\left(\frac{\tau}{\rho}\right)_{i,E_0}}{sin(\psi)} \left(1 - \frac{1}{r_{i,j}}\right) \cdot \rho_s \cdot \omega_{i,j} \cdot p_{i,j,k} \cdot dx\right]}_{emission\ of\ fluorescent\ radiation} \cdot \underbrace{\frac{d\Omega_2}{4\pi} \cdot \epsilon_{E_{i,j,k}}}_{detector} \tag{2.22}$$
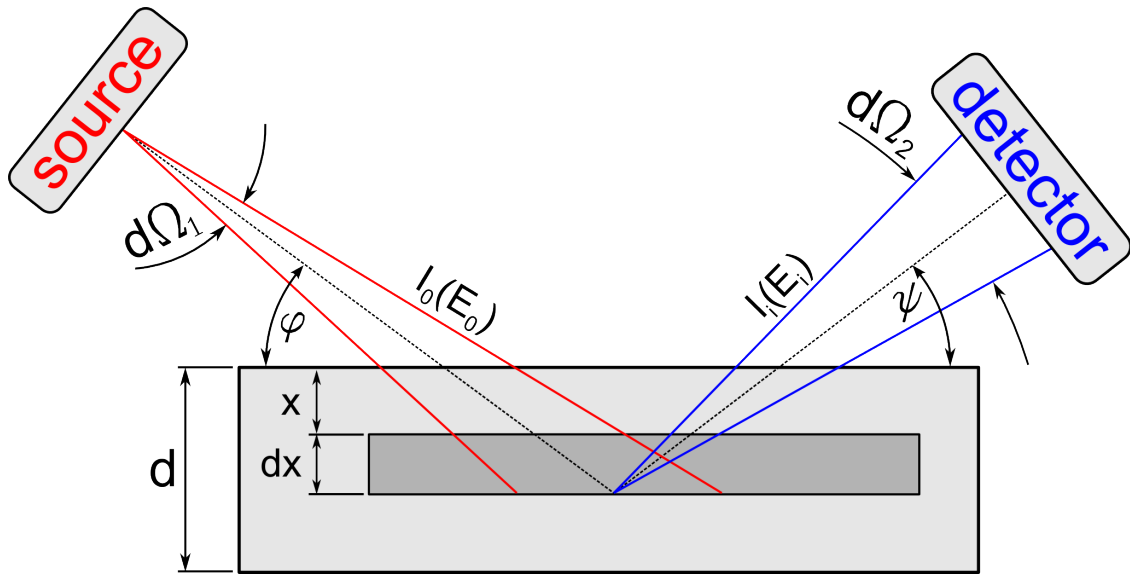
Figure 2.16: **Geometry for the calculation of the intensity of characteristic radiation with the fundamental parameter method**

An incident X-ray beam from the left (red) with an opening angle of $d\Omega_1$ and intensity $I_0(E_0)$ interacts with a differential element dx of the sample material under an entry angle ψ in a certain depth x, where characteristic radiation is generated (blue) and registered with a certain intensity $I_i(E_i)$ for each element i, by a detector under an exit angle ϕ, with a certain efficiency ϵ and opening angle $d\Omega_2$.

2.4.2 The empirical approach

Since the fundamental parameter method described in the previous section (2.4.1) is a rather complicated subject, the empirical method relies only on the use of standards ministered by the International Organization for Standardization (ISO) [36], as a means of quick, industrial calibration and analysis technique.

According to the work of Criss and Birks [37] the intensity for the same element in different multi-element materials of varying concentration is a non-linear function

due to matrix effects such as selective absorption, secondary excitation or other effects. This means, that the intensity for each element has to be a function of all elements in the sample as described in equation 2.23. The following formulas are a simplified example and based on the assumption that the samples are reasonably thick, homogeneous with a flat surface and monochromatic radiation is used. Furthermore no influences of the detector or corrections for the background are taken into account. Nevertheless these simple equations are well suited for several applications, such as analysis of steel samples, alloys or other basic materials. It shall be noted that multicomponent samples that cover a wide range of the expected composition are best suited for calibration, as second order effects are automatically taken into account and the number of samples can be kept to a minimum.

$$R_i = f(C_1, C_2, C_3, ..., C_n), \qquad R_i = \frac{C_i}{\sum_{j=1}^{n} \alpha_{i,j} C_j} \qquad (2.23)$$

With the assumptions mentioned above it is possible to determine the n^2 α coefficients for an n-element system by measuring at least n samples of known composition (standards). For example, if we consider a 3 element system A, B, C one would require at least 3 different standards (1, 2, 3) as mentioned before. This yields a set of three equations (equation 2.24) for each element. With the obtained α coefficients and the additional equation, that the sum of all concentrations has of course to be 1, it is now possible to analyze a sample of unknown composition and recieve very good results.

$$\left. \begin{aligned} \frac{C_{A,1}}{R_{A,1}} &= \alpha_{A,A} C_{A,1} + \alpha_{A,B} C_{B,1} + \alpha_{A,C} C_{C,1} \\[2ex] \frac{C_{A,2}}{R_{A,2}} &= \alpha_{A,A} C_{A,2} + \alpha_{A,B} C_{B,2} + \alpha_{A,C} C_{C,2} \\[2ex] \frac{C_{A,3}}{R_{A,3}} &= \alpha_{A,A} C_{A,3} + \alpha_{A,B} C_{B,3} + \alpha_{A,C} C_{C,3} \end{aligned} \right\} \quad \text{3 element example (A,B,C)} \quad (2.24)$$

Chapter 3

Experimental setup

All experiments conducted during this research where performed using the AMP-TEK 4 Watt Mini-X x-ray tube [1] in a direct configuration, or the Seifert 2.2 KW high power tube (PW2279/20) either in a direct configuration, or in combination with a secondary target to achieve polarized irradiation. Both tubes utilize a silver anode target material. For future references these different conditions will be referred to as low power direct, high power direct or high power polarized.

To achieve an interchangeable and easy to use set-up, both tubes are mounted on a hole matrix table inside a 30mm thick acrylic glass cage for radioactive protection. They share the same x-y table and all experiments are controlled with the X-Spect software, that was written by Stephan Smolek and Alexander Utz and had to be heavily tweaked and expanded during this thesis. The resulting radiation is measured with an AXIS-D silicon drift detector (SDD) from KETEK [2].

The following pages will describe the used equipment in detail together with the set-up of the low power tube that was designed during a previous project work [38] and the high power set-up that had to be adapted during this work.
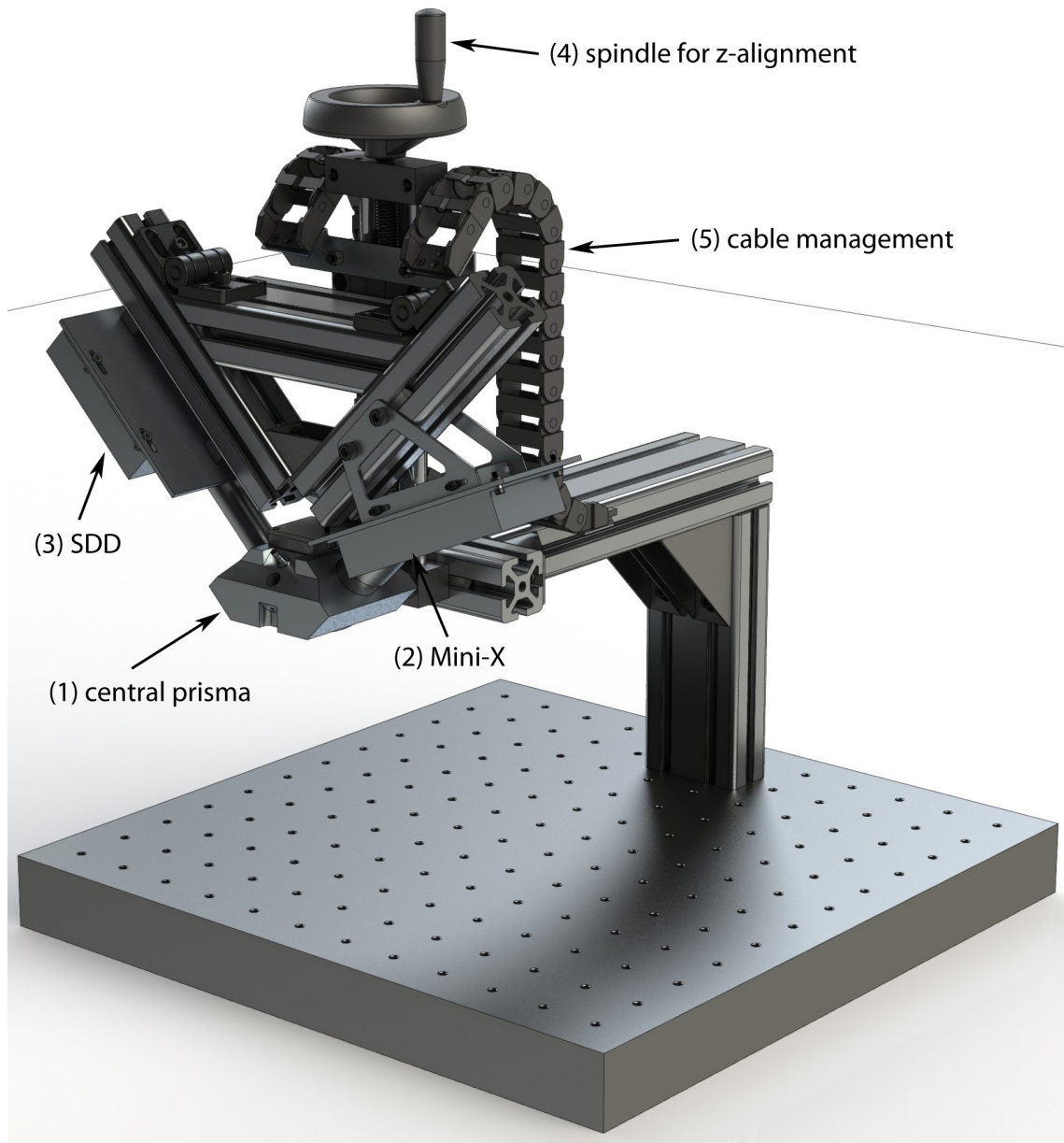
Figure 3.1: **Final rendering of the Makro-XRF facility:** (1) central prisma, (2) Mini-X X-ray source, (3) AXIS-D SDD, (4) spindle for z-alignment, (5) cable management

The low power set-up is depicted in figure 3.1 and was designed in a previous work [38] with the software Solidworks [39] in 3D. To save manufacturing time, standard strat profiles were used, wherever applicable. The main parts of this machine are the X-Ray source Mini-X, the silicon drift detector (SDD) AXAS-D, which are described in detail in section 3.1.1 and 3.2 respectively. Because standard strat profiles were used, additional equipment can be easily added if required and the complete setup can be mounted on any standard hole-table.

The most important part of the Makro-XRF system is the central prisma (see figure 3.2), which is mounted to a linear spindle-lift table. It houses the SDD, the Mini-X tube, two laserpointers and a camera, with all axis centered on the same spot, approximately 0.43 mm below the lowest point of the prisma. There is also support for the attachment of a gas tube to provide optional Nitrogen flush or a vacuum pump to evacuate the system.

By using a fluorescence screen as a target, the two laser pointers can be adjusted to focus on the same point as the x-ray, thus enabling continuous monitoring of the beam spot on the actual target with the attached camera. If both laser pointer spots overlap the x-ray beam is in focus and ready for measurements.

Since the chosen material of the prisma is aluminium, which is electrically conductive, two additional teflon tubes separate the SDD and XRF-source from the prisma, provide electrical isolation and serve as a sealing purpose for the optional nitrogen flush or evacuation.

To further increase the adaptability of the facility the prisma is designed to hold various detectors of different finger sizes. This is achieved by the use of interchangeable PTFE tubes which are inserted in the prisma as distance pieces.

An end piece serves as a protection of the underside of the prisma and can be fitted with an 8 μm thick Kapton [40] end window if nitrogen flush or evacuation are required. For this purpose an O-ring gasket serves as a tight seal between these two parts.
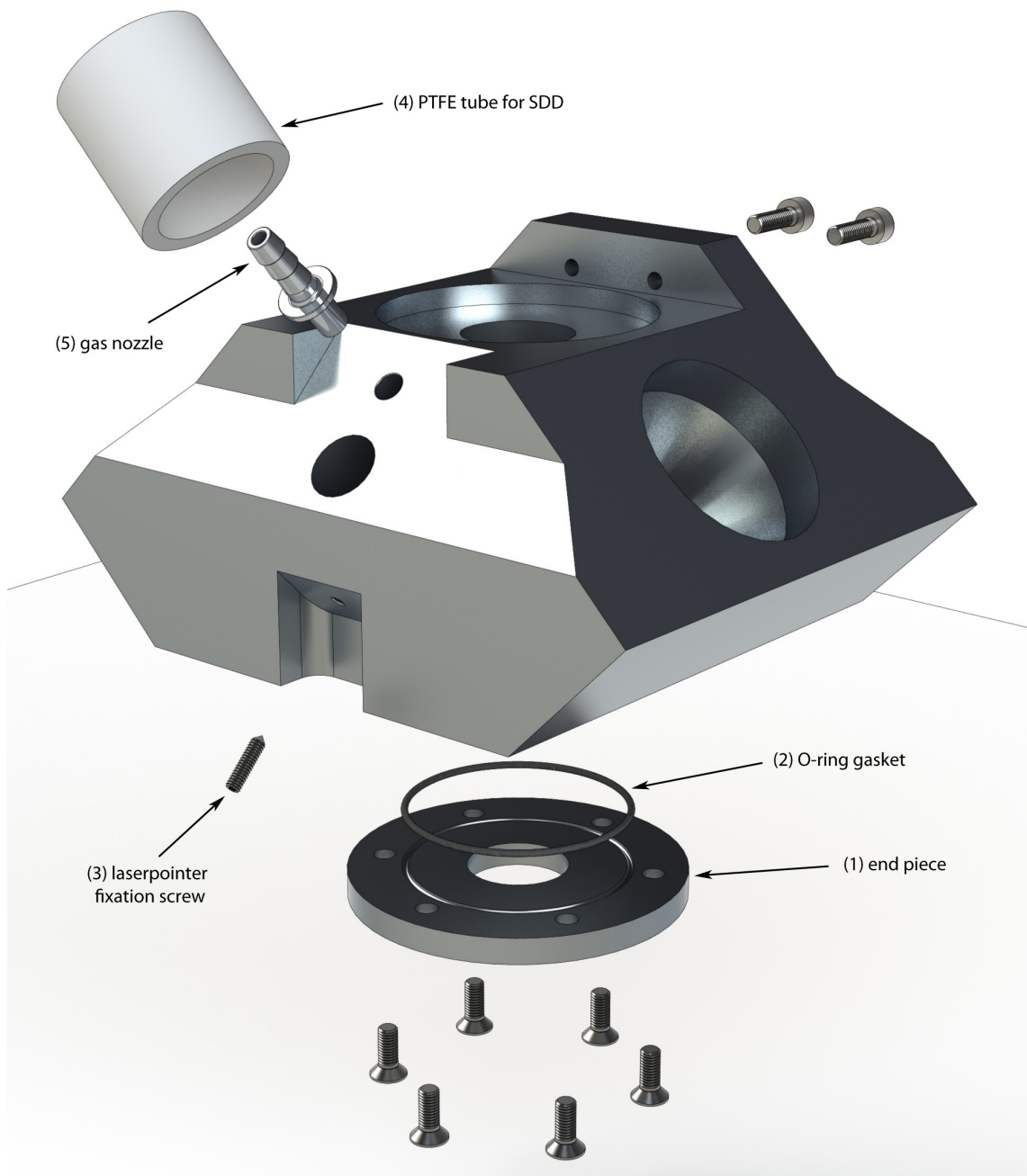
Figure 3.2: **Central prisma:** (1) end piece with optional Kapton [40] end window, (2) O-ring gasket, (3) laserpointer fixation screw, (4) PTFE tube for SDD, (5) gas nozzel

Finally, a simple USB-camera is mounted on top of the central prisma and provides visual information of the current beam spot position, the alignment of the two laserpointers and the object to investigate. If required, images can be recorded for documentation purposes. After a first test revealed that the picture of the webcam was quite dark, a new end piece made of acrylic glass was designed, that radially houses several white LEDs to achieve adjustable lightning conditions as needed. Both the laser pointer and LED intensity can be adjusted directly through the software.

3.1 X-ray tubes

3.1.1 Low power tube

Figure 3.3: **Mini-X X-ray tube from AMP-TEK** [1].

The Mini-X features a 50 kV/80 μA power supply, a gold (Au) or silver (Ag) transmission target and a beryllium (Be) end window. The dimensions are listed in table 3.1. Due to its low power design air cooling is sufficient even during continuous operation. It can be equipped with several filters such as Al, Cu, Mo, Ag or W if required [1].

Target Material	Silver (Ag)	Gold (Au)
Target thickness	0.75 μm	1.0 μm
Approximate dose rate	10 Sv/h @ 30cm	13 Sv/h @ 30cm
Approximate flux	$10^6 cps/mm^2$	$1.3x10^6 cps/mm^2$
	on the axis @ 30cm	on the axis @ 30cm
Focal spot size	$\approx$ 2mm	$\approx$ 2mm
Output cone	120deg	120deg
Window material	Beryllium (Be)	Beryllium (Be)
Window thickness	127 μm	127 μm

Table 3.1: Selected AMPTEK Mini-X specifications [1]

Formula 3.1 below, describes the penetration depth of electrons with a kinetic energy in the range between 10 keV and 3 MeV. The resulting depth has the dimension μm, E stands for the energy in MeV and ρ for the material density in g/cm^3.

$$R_{el} = \frac{4120}{\rho} E^{(1,265-0,0954 \cdot ln(E))} \tag{3.1}$$

In our case the typical energy is about 50 keV which leads to a penetration depth of 21.4 μm in beryllium, which is approximately one sixth of the end window thickness of the Mini-X. This ensures that only photons are emitted from the X-ray source.

In principle, when an atom is irradiated by an X-ray and the energy is high enough to excite the atom, a vacancy in an inner shell is created. After the corresponding decay time an electron from an outer shell eventually falls down to fill the hole and the excess energy is released as a photon with a specific wavelength, equivalent to the energy difference of the involved shells. This photon can then be detected and yields a characteristic peak for each element and transition. For a more detailed theoretical background on XRF analysis see section 2.1 or the excellent books [14] and [21].
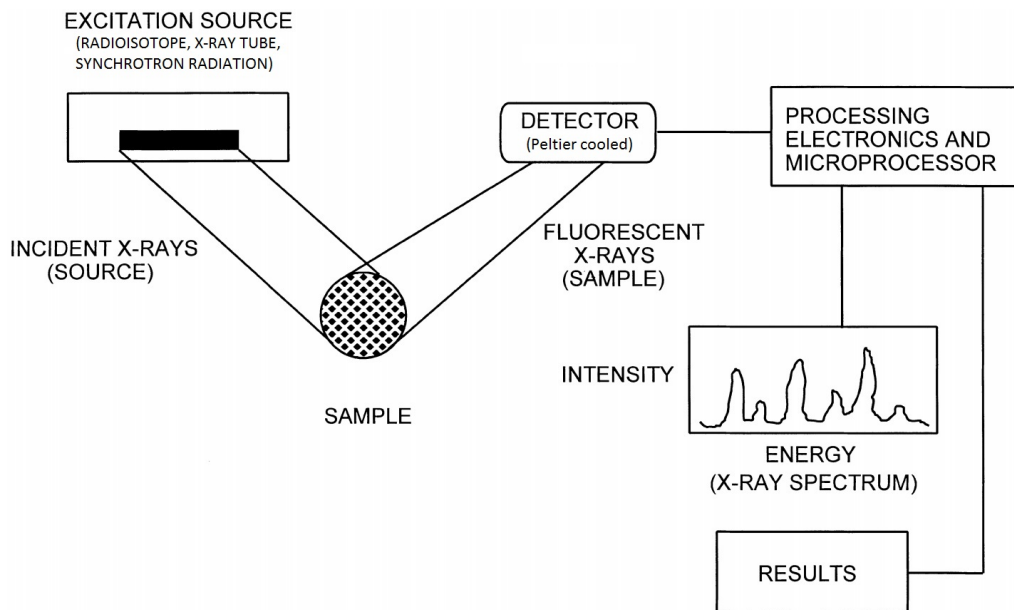
Figure 3.4: **Schematic view of a basic XRF setup:** A X-ray source irradiates the sample, resulting in characteristic X-ray radiation which is then measured by a detector and electronically processed to provide an energy/intensity spectrum for chemical analysis [21].

Figure 3.4 illustrates the working principle of **X-R**ay **F**luorescence Analysis (XRF). An excitation source provides the incident X-rays, which interact with the sample by several elastic and inelastic scatter processes and generates fluorescence radiation. This characteristic radiation travels again through the sample and the emitted photons are then registered by the attached SDD. The resulting signal is then enhanced by an amplifier, in our case the Canberra 2025 AFT, before it is further processed by the Amptek 8000A MCA (Multi-Channel-Analyzer). The resulting data is then sent to the computer to obtain an energy/intensity spectrum as a result. Such a spectrum might contain three different kinds of misleading artifacts, a sum peak, an escape peak or Compton-scatter. When two photons hit the detector almost at the same time, they cannot be distinguished and are counted as the sum of both thus resulting in the so called sum peak. An escape peak is a result of partial energy loss especially in the border region of the detector if some of the secondary photons generated by the incoming radiation leave the detector material.

3.1.2 High power polarized
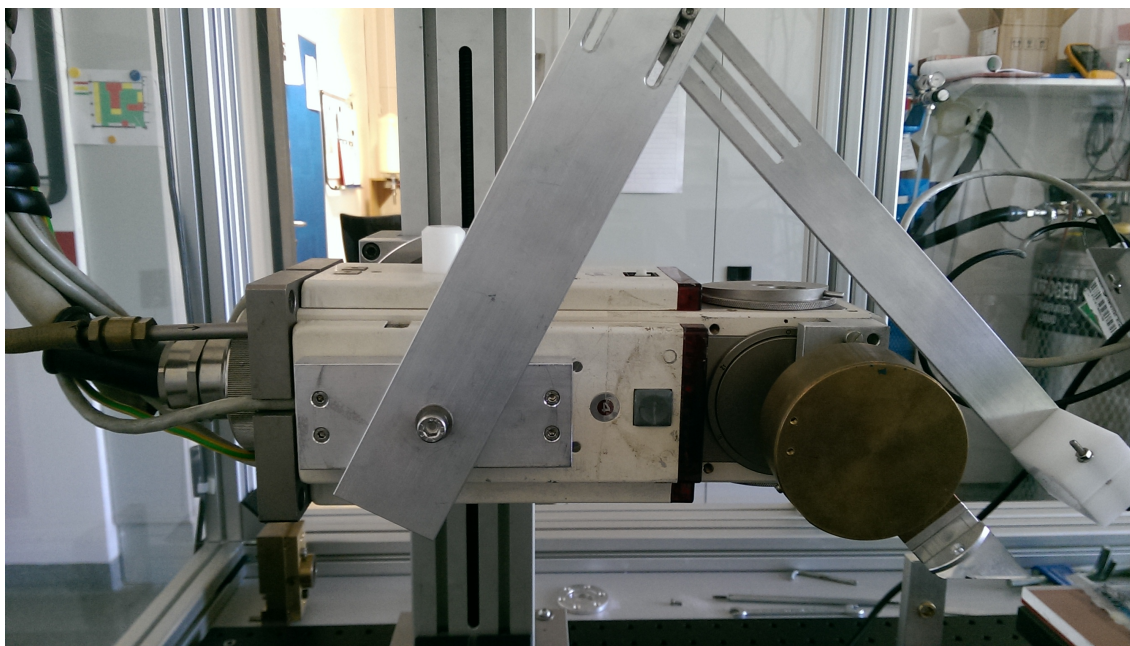
Figure 3.5: **High power polarized (HPP) configuration**

The PW2279/20 Seifert X-ray tube with a maximum power of 2.2kW is combined with a secondary XXX target in a 90° configuration and the KETEK AXAS-D [2] silicon drift detector.

The high power polarized set-up is depicted in figure 3.5. It consists of the water cooled, high power X-ray tube Seifert PW2279/20 with a maximum power of 2.2kW at 60kV and a silver target. The primary radiation is directed onto a secondary target made of molybdenum in a 90° configuration. This geometry yields a virtually monochromatic spectrum consisting only of the K_α and K_β lines of the secondary target material without any bremsstrahlung or anode lines and thus providing an excellent peak to background ratio. As mentioned above all configurations share the same x-y table and the silicon drift detector KETEK AXAS-D [2].

3.1.3 High power direct
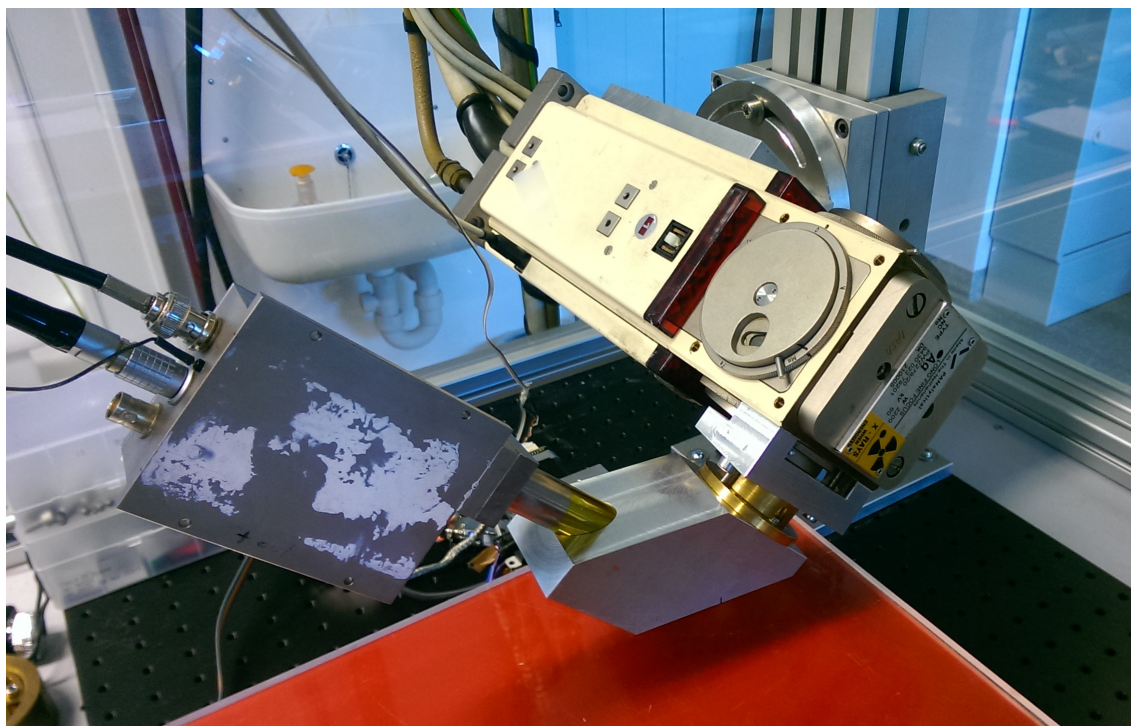
Figure 3.6: **High power direct (HPD) configuration**

The PW2279/20 Seifert X-ray tube with a maximum power of 2.2kW mounted on a 45° assembly to provide direct irradiation of the sample in combination with the KETEK AXAS-D [2] silicon drift detector.

For the high power direct set-up it was necessary to design and construct a 45° mounting assembly to hold the Seifert X-ray tube and a prisma with a interchangeable collimator that is directly attached to the tube and houses the KETEK AXAS-D [2] silicon rift detector as well. All the scematics of the prisma (section 5), the collimator (section 3) and the mounting assembly (section 4) can be found in the appendix. The advantage of this configuration is a very high intensity at the cost of a higher background.

3.2 Silicon drift detector

Figure 3.7: **AXAS-D silicon drift detector from KETEK** [2]

CLASS	STANDARD
Energy resolution	≤ 139 eV
Peak to background	> 6000
Peak to tail	> 1000
Absorption depth	450 μm Si
Peak shift stability up to 100 kcps	< 1 eV
Max. input count rate	1000 kcps
Window	8 μm Be
Cooling performance	Δ T > 75K
On-chip collimator	multilayer

Table 3.2: Typical key parameters of a VITUS H30 SDD [2]

The AXAS-D digital X-ray acquisition system from KETEK [2] includes a VI-TUS SDD (**S**ilicon **D**rift **D**etector), reset type preamplifier and DPP (**D**igital **P**ulse **P**rocessor). It supports X-ray energies in the range between 0.2 keV and 30 keV, various detector sizes and is peltier cooled, which results in a highly integrated, compact design. Table 3.2 contains some key parameters of the AXAS-D SDD.

A silicon drift detector consists of high purity silicon with a very low leakage current, which allows for peltier cooling, a transversal electric field created by ring shaped anodes with an increasing bias voltage to the outside and an integrated FET (**F**ield **E**ffect **T**ransistor) connected to the collecting anode, thus minimizing the stray capacitance and electronic noise. In this way the SDD can be operated in a continuous mode, as the anode is constantly discharged from the collected electrons. Some of the main advantages of a SDD are higher count rates and a very low capacitance.
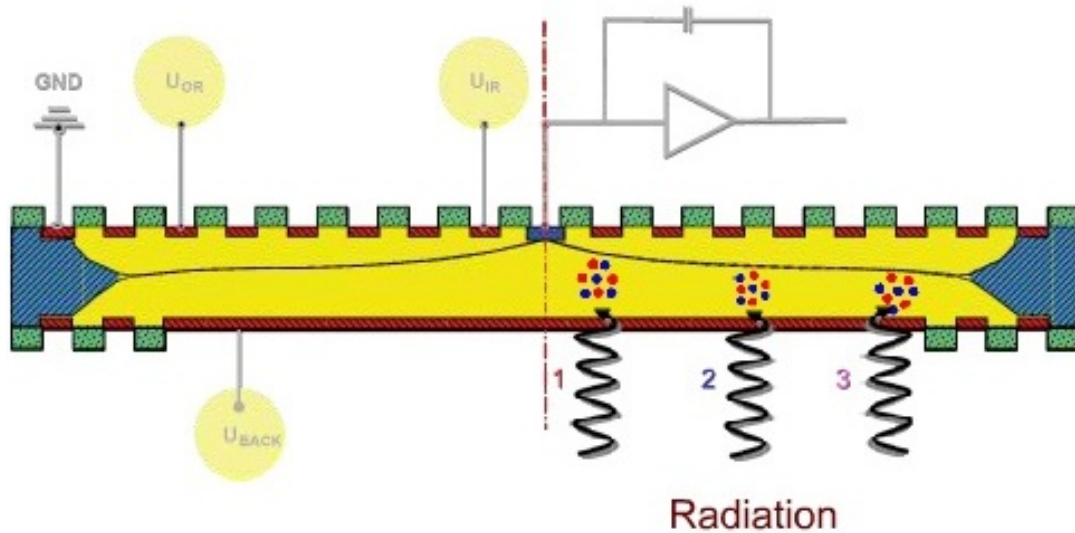
Figure 3.8: **Working principle of a Silicon Drift Detector** [1]:

> The high purity silicon (yellow) is depleted of all charge carriers by a transversal electric field created by ring anodes (red, top) of outwardly increasing bias voltage with the collector anode in the center (blue, top), thus forming a drift region. Three electron/positron pairs are created by impinging radiation (red and blue dots), which are distinguishable in their rise and detection time due to their different drift distance.

A cross section of a KETEK SDD is depicted in figure 3.8 below and illustrates the formation of electron/positron pairs by impinging X-rays in the depletion region. Because of the transversal electric field, the negative charge carriers now start to drift towards the collector anode in the center and the negative charge carriers towards the cathode respectively. Due to their different starting positions, the three simultaneously created events differ in rise and detection time.

Chapter 4

Software

Several different software packages complement each other regarding spectrum acquisition (AMPTEK ADMCA), measurement control (X-Spect)and spectrum evaluation (AXIL). The new equipment developed during this thesis made it necessary to add several new features to the X-Spect program that will be discussed briefly in section 4.2.

4.1 Analysis software

For quick and easy spectrum acquisition the AMPTEK ADMCA display and acquisition software [1] was used. This software package was integrated in the main control software X-Spect to directly acquire and store all necessary scan data. Some key features of this software include:

- acquisition presets, gain, peaking time, detector HV, detector temperature, number of channels, risetime discrimination parameters, and many more.

- Live display of the spectrum with many options. Includes linear and logarithmic vertical scaling, manual or auto-ranging, and zoom on the horizontal scale. Displays live spectrum and multiple stored or processed spectra.

- Spectral analysis features include energy calibration, setting regions of interest (ROI), computing ROI information (centroid, total area, net area, FWHM), spectrum smoothing, summing of spectra, subtraction and scaling of background spectra.

4.2 X-Spect

To control the x-y table and all external components that are part of the set-up a graphical user interface, the X-Spect software was developed by Alexander Utz during his master thesis [41]. Some of the basic functions of this program include the manual position mode, automatic 2-d scans and spectrum acquisition using the AMPTEK-MCA software package to create a graphical display of the acquired data that can be used to get some basic information of the spectrum.

During the development of the new set-up it was necessary to implement the webcam feed for easier positioning to the program. This allows the user to directly monitor the current position of the x-ray beam, marked by two overlapping laser pointers, take a screenshot manually or automatically at every scan position for documentation purposes.

An Arduino Micro micro controller [42] connected to the computer via USB, made it possible to tweak the light and laser pointer intensity directly through the X-Spect software by means of pulse width modulation. The Arduino Micro features 20 digital input/output pins, whereas 7 may be used as pulse width modulation outputs and 12 as analog input pins [42], offers great control capabilities for possible future requirements.

To easier estimate the overall time of a measurement a progress bar has been implemented along with a counter, that displays the time remaining until completion. A simple algorithm measures the time it takes for a single point measurement to complete and then multiplies it with the remaining points. However this time will greatly vary at first, because the time it takes to acquire one scan depends on several factors, such as scan time per point, detector acquisition and conversion time, movement time of the x-y table and a possible lag of the software itself.
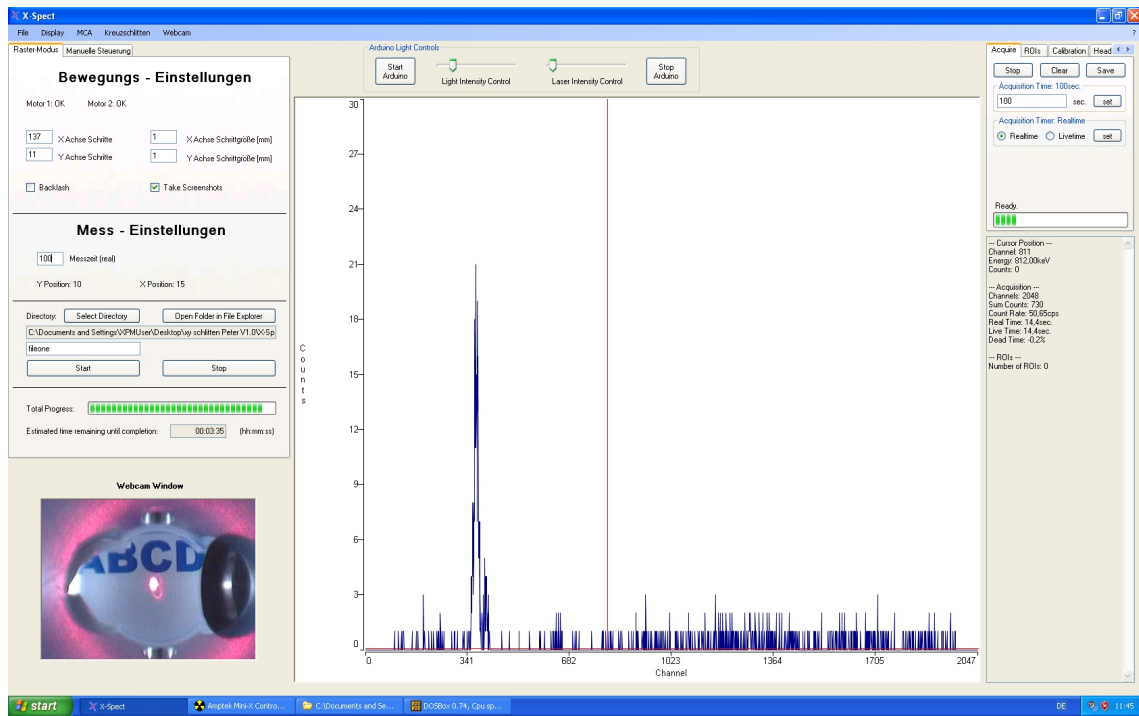
Figure 4.1: **X-Spect control software**

The image depicts the main window of the X-Spect control software during spectrum acquisition. All values regarding an area scan can be entered directly on the left above the webcam window with the current measurement position indicated by the overlapping laser pointers. Located above the diagram are the slider bars to adjust the brightness settings of the laser pointers and the auxiliary light source. The right side of the screen is used for manual measurements and contains information about current scan progress and the spectrum.

Another feature is the addition of KLM-markers in order to make it easier to identify the various peaks in the spectrum. This required the creation of a database of the characteristic line energies of all elements up to uranium. The correct implementation of these markers was a difficult task, because the K-α line should vary in size according to the peak height at the current position and scale down properly to the

K-β lines in order to distinguish sum peaks, overlaps and other artifacts. The same applies to the other lines as well. In case there should be no discernible peak at the marker position, the K-α line will be a quarter of the total frame size with the other lines scaled accordingly.

One last feature implemented is the possibility to compare either the last or a saved spectrum with the current one, to easily track the progress of certain elements per scan point or to simply compare two spectra of different samples or spots.

Most of these changes were added as new, separate functions in c# and may be reviewed in the corresponding section of the appendix. The main control window of the X-Spect software is depicted in figure 4.1 below and shows some of the new features added during this thesis. The data acquired using the X-Spect program is written into an ASCII file that can be processed by several other programs such as AXIL, that will be discussed in the next section.

4.3 Axil

The software used for evaluation is called **Q**uantitative **X**-ray **A**nalysis **S**ystem or QXAS and is from the IAEA laboratories in Seibersdorf, Austria. Figure 4.2 depicts a complex spectrum with several different element characteristic peaks such as Ar marked by the two vertical yellow lines that correspond to the Ar-Kα and Ar-Kβ.

With this program it is possible to create a suitable model using the so called sum-spectrum, which is simply the sum of all single points scanned during an area or line scan. The combined intensity in the sum-spectrum usually ranges from some 100 counts for trace elements, up to several 10.000 counts for main constituents. These peaks can be identified by looking up the characteristic line energies of the elements. For our purposes all relevant elements are added to the evaluation model, including possible sum and escape peaks. With the right settings concerning the background shape it is possible to achieve a decent deconvolution of the spectrum after only a few iterations.

Once satisfied with the results of the model it can be saved and used to quickly evaluate all single point spectra in a batch process which saves a lot of time as there can easily be more than 1000 single data files to process for an average area scan. A more detailed description and manual of this software is available online [43].
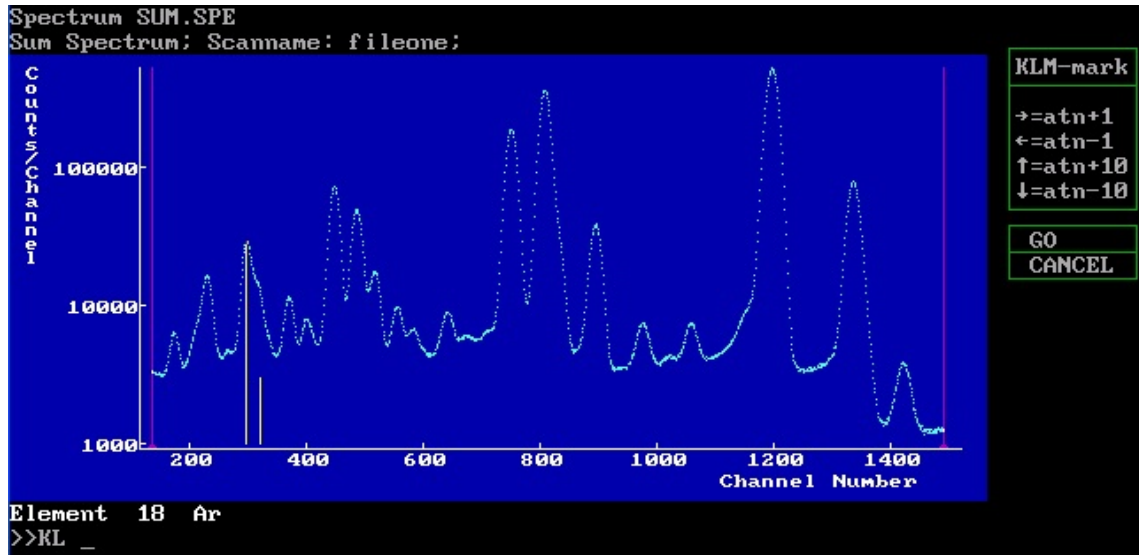
Figure 4.2: **AXIL sample spectrum**

> Typical spectrum of a multi element matrix. The vertical yellow lines below one peak are KLM-markers and correspond to the characteristic Ar-Kα and Ar-Kβ line.

Chapter 5

Measurements

5.1 Copper wire - set-up influences

For a first basic comparison of the different measurement methods, a simple copper wire strip with a diameter of 0.15mm was chosen and mounted either on a Teflon plate or a Kapton foil on a PTFE cylinder for reduced background as depicted in figure 5.1. The three methods to be compared are: low power (LP), high power polarized (HPP) and high power direct (HPD). For a full description of these methods see chapter 3.
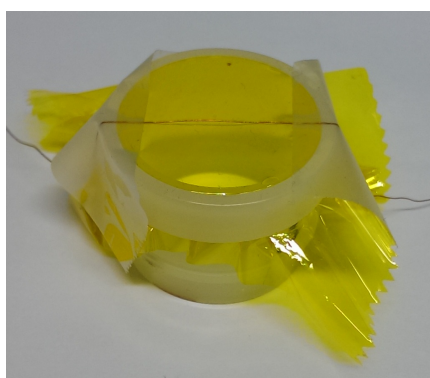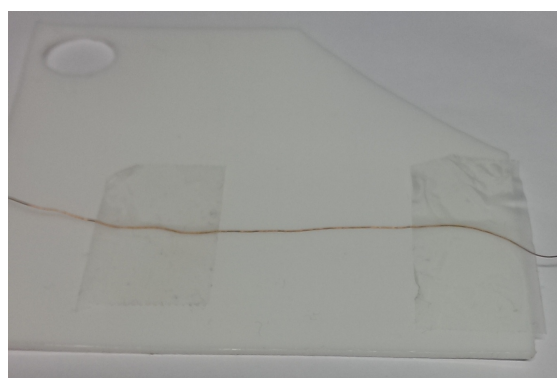
(a) Kapton foil   (b) Teflon plate

Figure 5.1: ∅**0.15mm copper wire on different support materials**

All configurations however use a 90° geometry and therefore the initial circular cross section of the X-ray beam hits the surface of the sample under an angle of 45 degree. This leads to an elliptic distortion of the beam spot on the target as depicted in figure 5.2 with a minor axis b corresponding to the diameter of the collimator and a major axis of $\sqrt{2}\cdot$b.
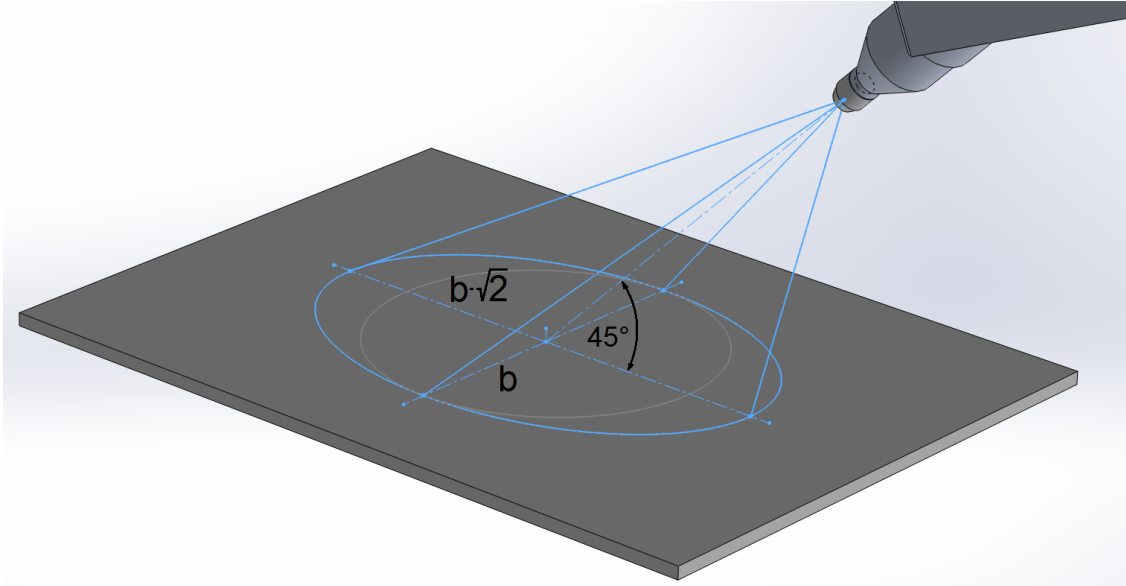
Figure 5.2: **Illustration of the elliptic distortion of the beam spot**

    Due to the geometric set-up an elliptic distortion of the beam spot occurs and has to be taken into account regarding resolution and possible overlap.

Due to this elliptic distortion mentioned above, when conducting an area scan with a collimator diameter the same size as the step size, the resulting counts will include an overlap region and some additional area compared to a pure circle. These conditions are illustrated in figure 5.3 and the respective areas are color coded. It is now fairly easy to calculate the area of these regions according to equation 5.3 (overlap - gray) and 5.5 (additional area - blue). Equation 5.3 calculates the intersection area of two ellipses with major axis a, minor axis b and distance s. The next formula 5.4 describes the intersection of an ellipse with a circle of radius b and separation s. This is needed to derive the final equation 5.5, which subtracts half of the area of

a circle from an ellipse and from that area the result for the whole overlap area 1 minus area 3 to calculate the overlap area as depicted. For quantitative analysis it is necessary to correct for the overlap and thus subtract the counts corresponding to the overlap area considering a Gaussian distribution of the beam intensity.

$$\frac{(x-x_0)^2}{a^2} + \frac{y^2}{b^2} = 1, \qquad\qquad x = \pm\sqrt{a^2 - \frac{a^2y^2}{b^2}} + x_0 \qquad (5.1)$$

$$(x-x_0)^2 + y^2 = r^2, \qquad\qquad x = \pm\sqrt{r^2 - y^2} + x_0 \qquad (5.2)$$

$$\text{area } 1 = \int_{-b}^{+b} dy \int_{-\sqrt{a^2 - \frac{a^2y^2}{b^2}}+x_0}^{+\sqrt{a^2 - \frac{a^2y^2}{b^2}}} dx \cdot 1 = b(a\pi - 2s) \qquad (5.3)$$

$$\text{area } 2 = \int_{-b}^{+b} dy \int_{-\sqrt{b^2 - y^2}+x_0}^{+\sqrt{a^2 - \frac{a^2y^2}{b^2}}} dx \cdot 1 = \left(ab + b^2\right)\frac{\pi}{2} - 2bs \qquad (5.4)$$

$$\text{area } 3 = 2 \cdot \left\{\left(ab - r^2\right)\frac{\pi}{2} - \left[b(a\pi - 2s) - \left(\left(ab + b^2\right)\frac{\pi}{2} - 2bs\right)\right]\right\} \qquad (5.5)$$
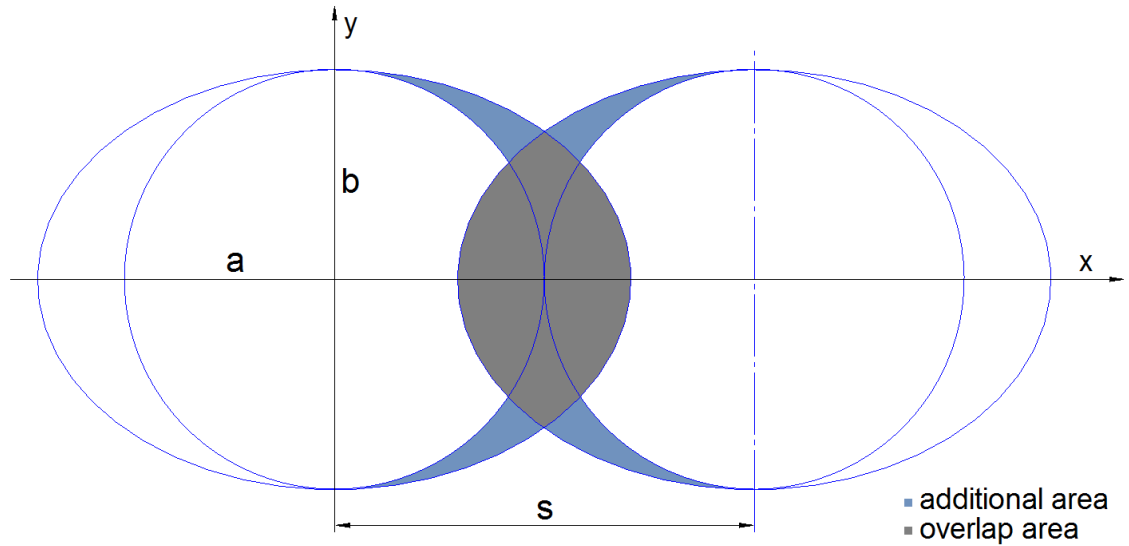
Figure 5.3: **Different areas as a result of elliptic distortion**

Another effect of this elliptic distortion is the different resolution depending on the orientation of the test piece to the line defined by the X-ray tube and the detector. For this reason a line scan on the two different copper wire configurations were conducted, with either parallel or perpendicular orientation of the major axis of the ellipse in respect to the wire. All scans involved 12 steps with a step size of 1mm covering 12mm in total, a scan time of 20s per point and a voltage of 50kV at 35mA for the high power configurations or 30kV and 30μA for the low power tube. The results are listed below in table 5.1 and were evaluated in AXIL using the sum spectrum of all 12 measuring points and correspond to the Cu-K_α peak.

CONFIGURATION	PEAK AREA	BACKGROUND	FWHM	χ^2
LP $\perp$ Teflon	5952 $\pm$62	216	215.78	4.1
LP $\parallel$ Teflon	7615 $\pm$70	193	213.60	2.0
LP $\parallel$ Kapton/air	6149 $\pm$61	65	214.30	3.4
LP $\perp$ Kapton/air	8479 $\pm$71	68	212.37	2.6
HPP $\perp$ Teflon	875 $\pm$7	0	241.32	1.3
HPP $\parallel$ Teflon	1198 $\pm$26	0	214.15	1.5
HPP $\perp$ Kapton/air	1221 $\pm$8	0	217.26	1.5
HPP $\parallel$ Kapton/air	1471 $\pm$9	0	224.60	1.3
HPD $\perp$ Kapton/air	246163 $\pm$479	49917	272.42	14.2
HPD $\parallel$ Kapton/air	265299 $\pm$493	49983	277.04	18.1
HPD $\perp$ Teflon	220598 $\pm$363	7617	250.28	3.7
HPD $\parallel$ Teflon	268658 $\pm$405	4596	263.58	8.7

Table 5.1: **Comparison of low power versus high power irradiation**

As assumed, the peak area of the perpendicular orientation corresponds approximately to the parallel orientation by a factor of $\sqrt{2}\cdot$. The peak to background ratio for the polarized configuration is remarkable, whereas the low power and high power direct methods have a rather similar relation.

The evaluated Cu intensities for each point of the line scan for every configuration were centered and fitted with a Gauss function in the program IGOR Pro [44] to calculate the FWHM (Full Width at Half Maximum) values of each method and orientation. Figures 5.4 to 5.6 depict these data in respect to either low power, high power polarized or high power direct configuration.

All this data is listed in table 5.2 to allow a more direct and convenient comparison. Again the FWHM values of perpendicular and parallel orientation have approximately a $\sqrt{2}$ relation. The very narrow distribution of the high power direct method is most likely related to the very high intensity and thus statistics. Although the high power polarized results have a much lower intensity than the low power results, the FWHM value for the HPP configuration surpasses the one of the LP due to the neglectable background in this method.
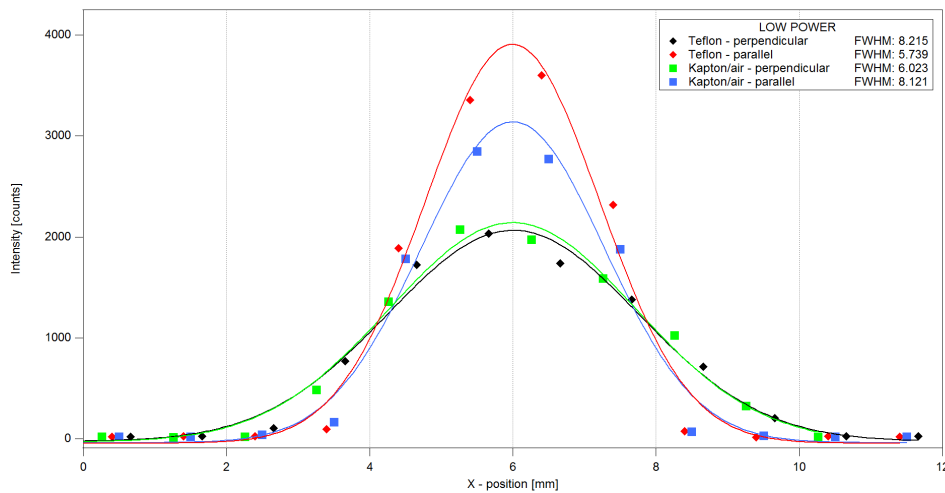
Figure 5.4: **Low power Gauss fits.** Settings: 12mm line scan with a step size of 1mm, collimator ∅1mm, 20 seconds scan time and a voltage of 30kV at 30μA in either perpendicular or parallel orientation in respect to the copper wire, on a Kapton foil or a Teflon plate.
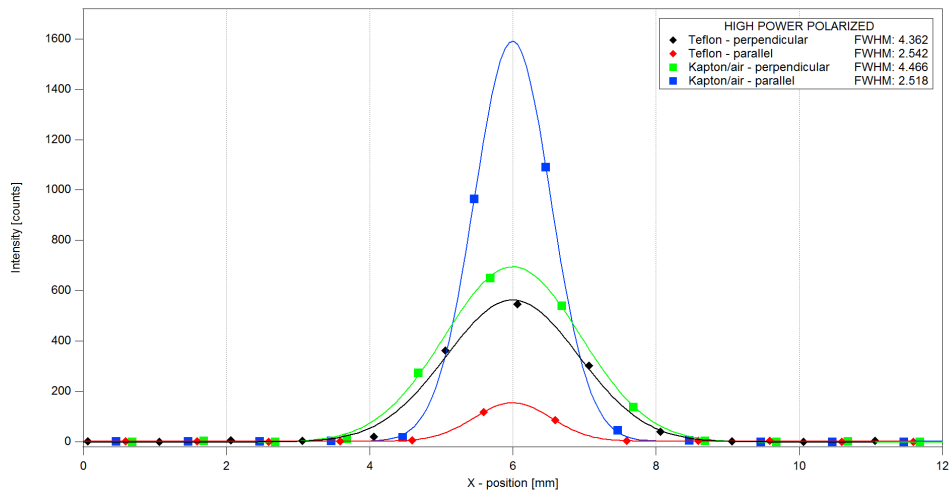
Figure 5.5: **High power polarized Gauss fits.** Settings: 12mm line scan with a step size of 1mm,collimator ∅1mm, 20 seconds scan time and a voltage of 50kV at 35mA in either perpendicular or parallel orientation in respect to the copper wire, on a Kapton foil or a Teflon plate.
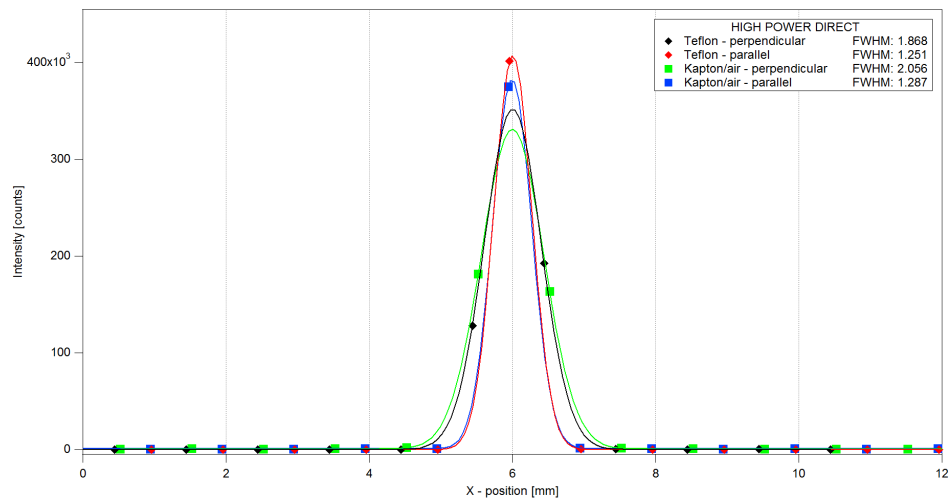
Figure 5.6: **High power direct Gauss fits.** Settings: 12mm line scan with a step size of 1mm, collimator ∅1mm, 20 seconds scan time and a voltage of 50kV at 35mA in either perpendicular or parallel orientation in respect to the copper wire, on a Kapton foil or a Teflon plate.

CONFIGURATION	SUPPORT MATERIAL	ORIENTATION	FWHM
low power collimator ∅1mm 20s scan time 30kV/30μA	Teflon	⊥ perpendicular	8.215
		∥ parallel	5.739
	Kapton/air	⊥ perpendicular	6.023
		∥ parallel	8.121
high power polarized collimator ∅1mm 20s scan time 50kV/35mA	Teflon	⊥ perpendicular	4.362
		∥ parallel	2.542
	Kapton/air	⊥ perpendicular	4.466
		∥ parallel	2.518
high power direct collimator ∅1mm 20s scan time 50kV/35mA	Teflon	⊥ perpendicular	1.868
		∥ parallel	1.251
	Kapton/air	⊥ perpendicular	2.056
		∥ parallel	1.287

Table 5.2: **Gauss fit comparison for all three configurations**

5.2 Laserjet bars - resolution test

As a simple reproduceable resolution test, a pattern was chosen that originates from the United States Air Force (USAF), who utilized it to investigate the resolution of optical imaging equipment. It consists of several groups of 3 parallel bars with certain spacing and dimension. To cite the USAF MIL-STD-150A [45]:

"The resolving power target used on all tests shall be as follows: The target shall consist of a series of patterns decreasing in size as the $\sqrt{2}$, $\sqrt[3]{2}$, $\sqrt[6]{2}$, with a range sufficient to cover the requirements of the lens-film combination under test. The standard target element shall consist of two patterns (two sets of lines) at right angles to each other. Each pattern shall consist of three lines separated by spaces of equal width. Each line shall be five times as long as it is wide."

With this standard in mind a custom test pattern (figure 5.7b) was designed, that fulfills these rules and is compact enough to allow for a reasonable scanning time. Because the laserjet color blue contains only small trace amounts of copper (Cu) a scan time of 175s (LP) and 20s (HPP and HPD) per point ($1mm^2$) was required.
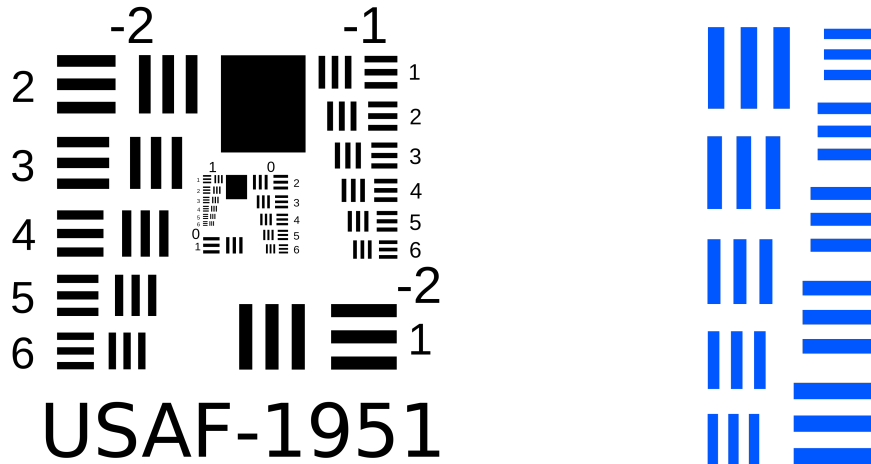
(a) Standard USAF-1951 test pattern   (b) Customized test pattern

Figure 5.7: **USAF-1951 test pattern conforming to MIL-STD-150A** [45]

After scanning an area of 25x55 mm^2 with the low power set-up and 30x60 mm^2 with the high power tube respectively, the data was evaluated with the program AXIL [43] for the element copper. The larger scan size of the high power tube was necessary because of uncertain positioning circumstances. Due to the implemented camera in the low power design no such flaws are given in the other system. All data files with the evaluated spectra are automatically processed by a MATLAB [46] program created by Alexander Utz [41] that generates a 2 dimensional map for each element selected. The results for both, high and low power tubes are depicted below in figure 5.8 and 5.9 respectively. While the last 2 bar groups are not clearly distinguishable for the low power set-up, all bars are discernible for the high power set-up. This outcome is on one hand caused by the elliptic distortion of the beam in one direction, but that applies to both systems and on the other hand due to the greatly increased intensity of the high power tube, resulting in much better statistics.
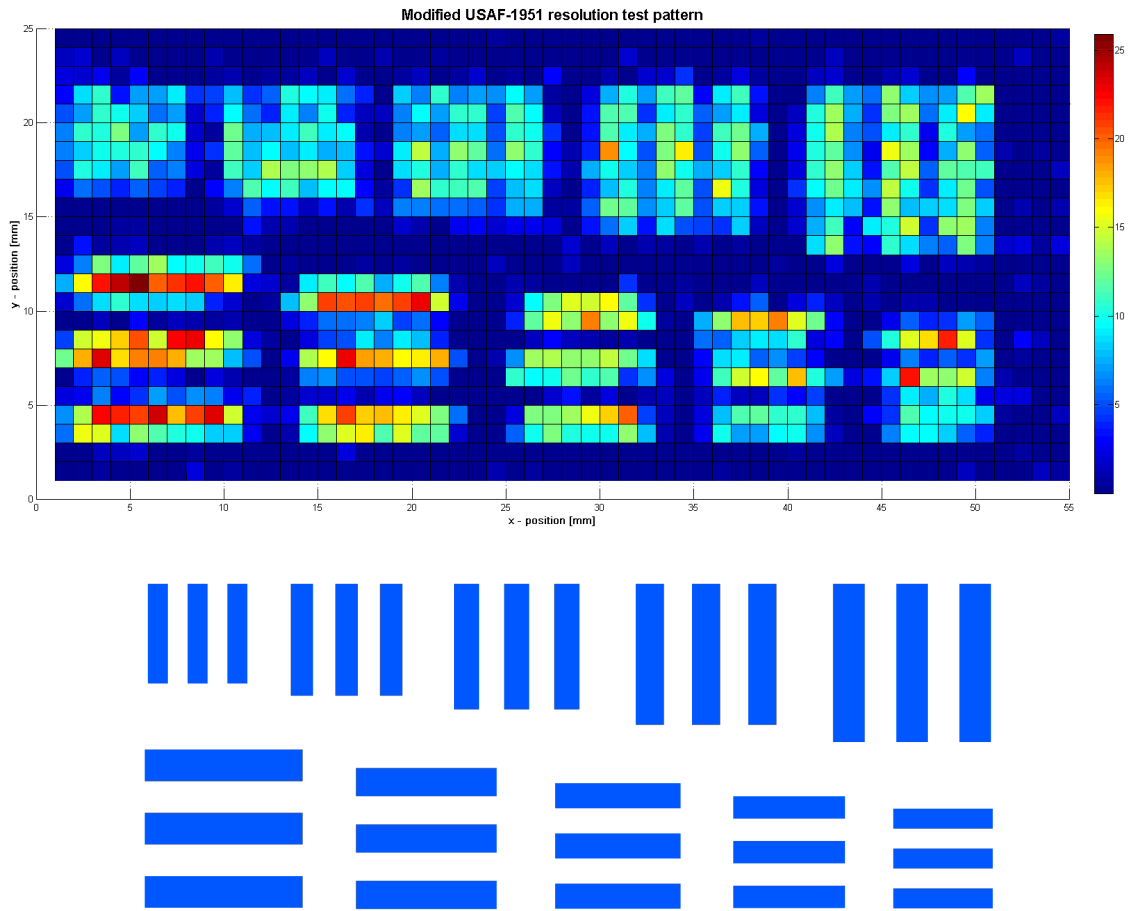
Figure 5.8: **Low power tube resolution test - copper distribution**
LP settings: 175 seconds scan time, voltage of 40kV at 80μA and a scan frame of 25x55 mm with a step size of 1mm. The maximum copper intensity is 27 counts and the major axis of the ellipse is in the X-axis.
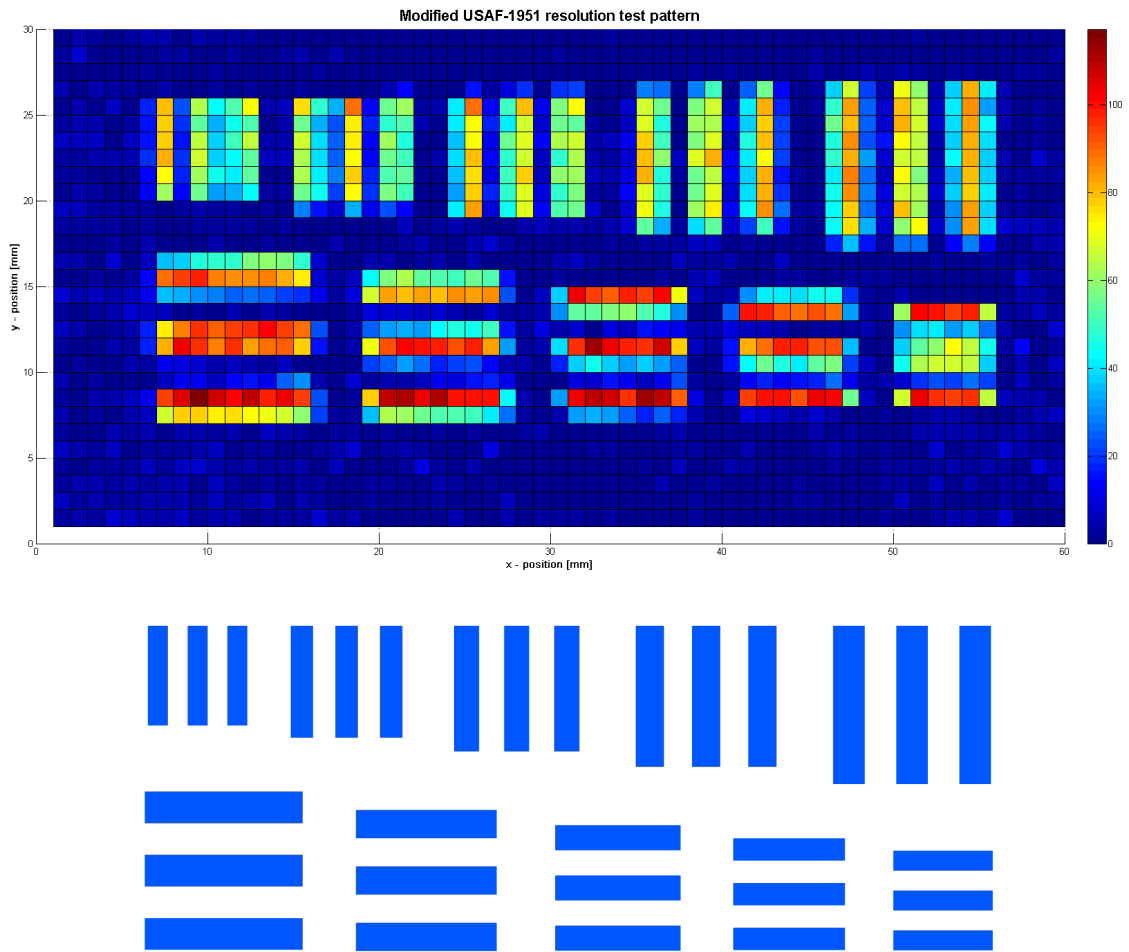
Figure 5.9: **High power tube resolution test - copper distribution**
HPD settings: 20 seconds scan time, voltage of 30kV at 10mA and a scan frame of 30x60 mm with a step size of 1mm. The maximum copper intensity is 114 counts and the major axis of the ellipse is in the X-axis.

5.3 Circuit board - resolution test

The second resolution test was motivated by an industrial inquiry if we are able to determine the gold (Au) distribution on circuit boards, especially if the required thickness of all gold contacts conform to the specifications as ordered. With this

topic in mind a sample piece of a circuit board was selected and analyzed with both tubes and again evaluated in AXIL [43] and further processed in MATLAB [46]. The results are depicted in figure 5.10 and 5.11 along with a picture of the original board. Since one of the main elements of most circuit boards is bromine (Br) the images (a) and (b) present a complimentary information, as high Br means less Cu and vice versa, because the conductive Cu tracks will shield the base material. With our current set-up and the use of a ⌀1mm collimator it was only possible to distinguish rough shapes of the gold platings on the board. It shall be noted that the high power direct configuration seems to display a much better resolution because of far greater count rates and thus statistics.

Nevertheless one can assume that with a collimator diameter corresponding to such small structures it should be easily possible to accomplish such a task, especially since no trace element analysis is required, which means that the scan time per point can be kept to a minimum. It shall be noted, that for a even more detailed or even multi-layer board design confocal XRF techniques would be more suited. For future applications, the use of optical X-ray components such as a poly-capillary would allow a resolution of 30 to 200 μm in addition to a more focused intensity, but such an equipment has the drawback of being rather expensive.

(a) Low power Cu   (b) Low power Br   (c) Original
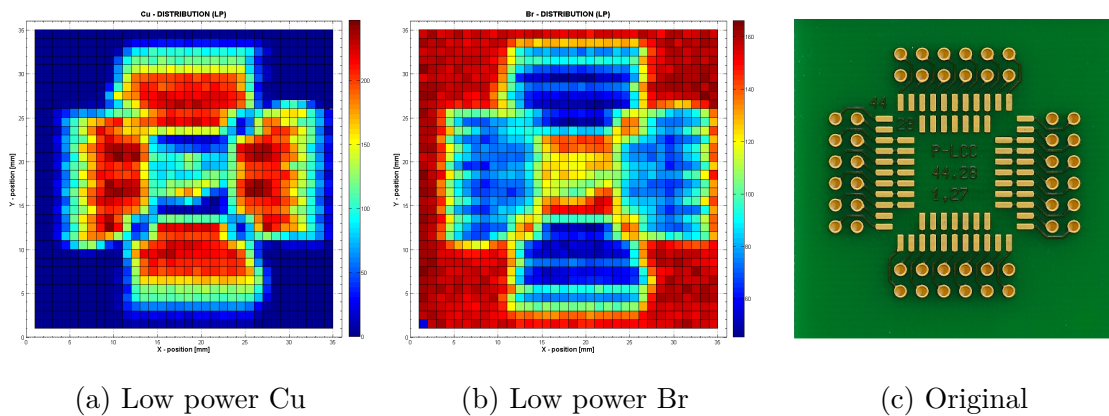
Figure 5.10: **Low power configuration - circuit board**

LP settings: 30 seconds scan time, voltage of 30kV at 30μA and a scan frame of 35x35 mm with a step size of 1mm. The maximum copper intensity is 165 counts and the major axis of the ellipse is in the X-axis.

(a) High power Cu (b) High power Br (c) Orginal
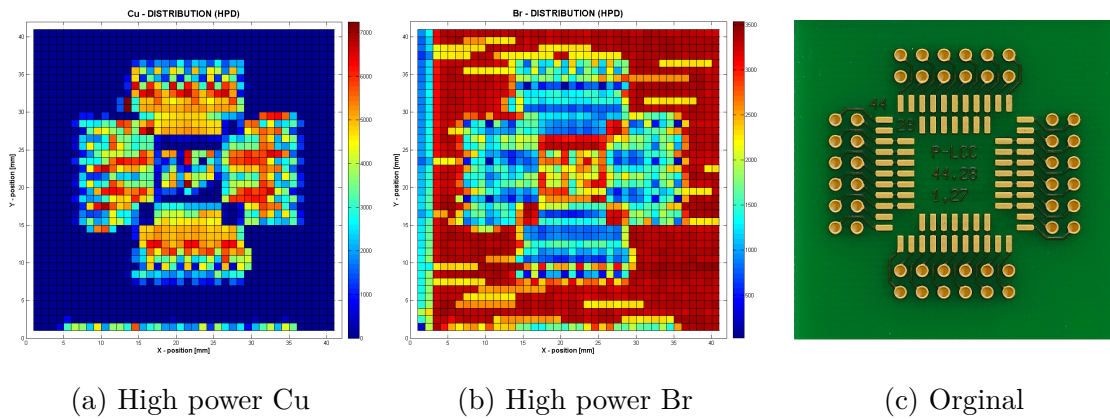
Figure 5.11: **High power direct configuration - circuit board**
HPD settings: 5s scan time, voltage of 30kV at 10mA and a scan frame
of 30x30 mm with a step size of 1mm. The maximum copper intensity
is 3517 counts and the major axis of the ellipse is in the X-axis.

5.4 Cross section of steel forgings

Another interesting application of macroscopic 2d elemental mapping might be found
in the steel industry. During the casting process various elements undergo segrega-
tion processes in different strength and variety. Such impurities are quite normal but
can vary in strength and distribution and might be influenced by different settings
during the casting process. Forging or remelting will change the distribution and
magnitude of such segregations. Informations gathered about the distribution of
these segregations might help in optimizing casting or remelting procedures. In co-
operation with the steel plant *Breitenfeld Edelstahl AG* [47], this topic was discussed
and two different samples of forged products were supplied for investigation.

5.4.1 High power direct

Figure 5.12 depicts a section of a forged ring from which 4 samples were taken,
covering the whole area from the outer diameter to the inner diameter. Because of

the large dimensions these samples were only scanned with the HPD configuration with a voltage of 40kV at 5mA, a scan time of 5s per point and a step size of 1mm, covering an area of 110x40mm per piece. As illustrated the areas will be numbered from 1 to 4 starting at the outside diameter.
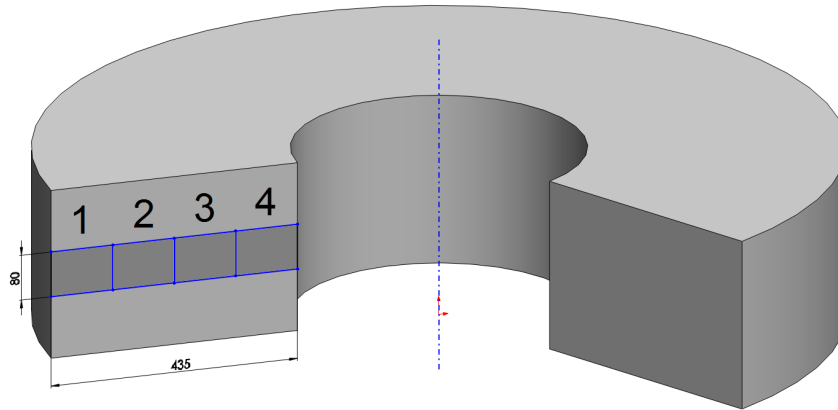
Figure 5.12: **Ring forging from Breitenfeld Edelstahl AG [47]**

Illustration of the cross sections taken from a forged ring with a total area of 80x435mm divided into 4 pieces numbered from 1 to 4 beginning at the outside diameter.

Every point can by analytically evaluated either with the fundamental parameter method described in chapter 2.4.1 or the empirical coefficient method described in chapter 2.4.2 respectively. Since the steel plant supplied the chemical analysis of the forged material, the latter method can be applied for a quick quantitative evaluation.

For this purpose, the sum spectrum of the HPD mesaurements is assumed to correspond to the supplied reference analysis. The small deviations observed and depicted in the following color maps may be assumed to be linear. Thus a quick and easy conclusion can be made about the variation in elemental concentration. The following images represent the elemental distribution of the elements manganese (Mn≈0.66%) and nickel (Ni≈3.37%).
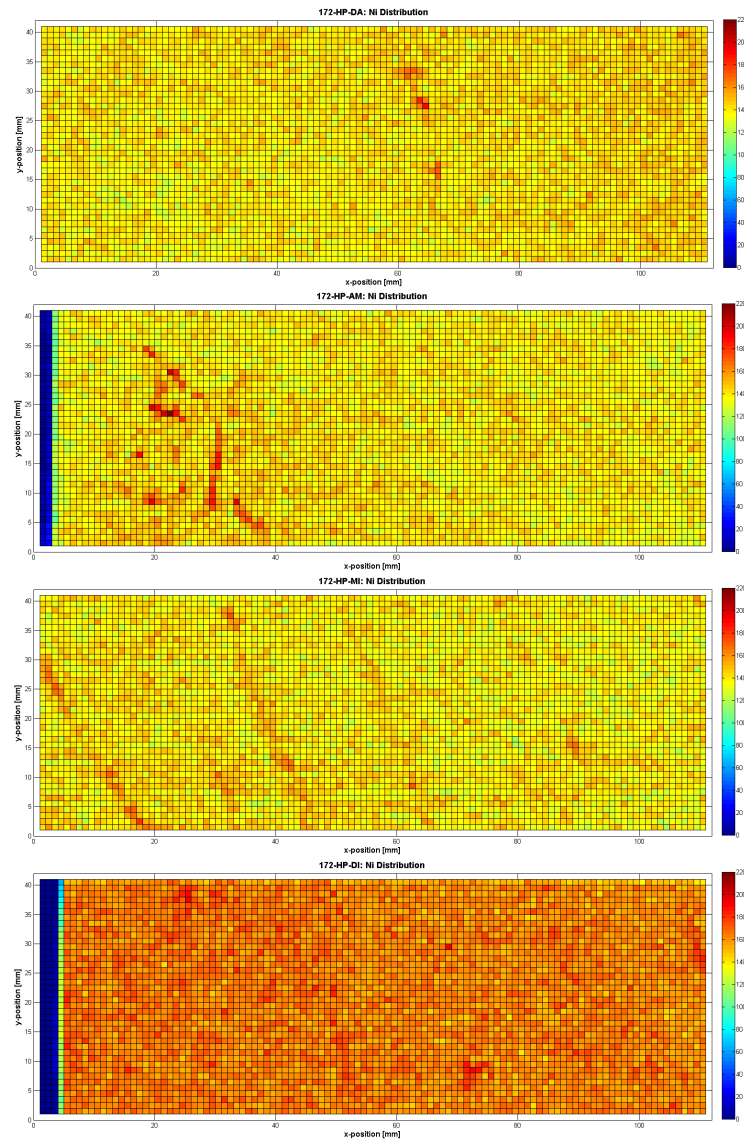
Figure 5.13: **Elemental distribution of Ni from top=1 to bottom=4**

Nickel distribution of the complete cross section from the outer diameter=1=top to the inner diameter=4=bottom as depicted in figure 5.12. The intensity color scale is the same on each image. Some artifacts are visible, especially in the 2nd picture. The reason for the higher intensities on the last image might be due to a different distance between the prisma and the steel sample resulting in a slightly better focus.
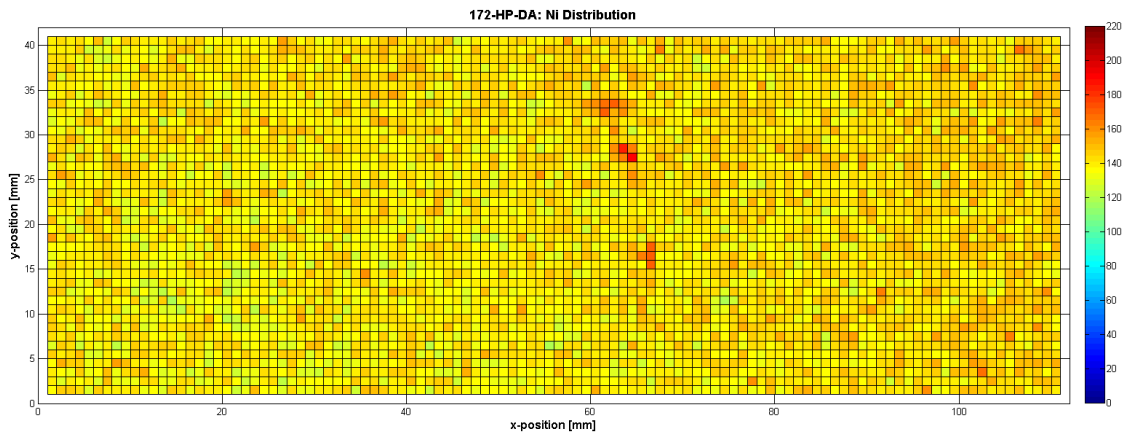
Figure 5.14: **Detailed nickel color map of the 1st section**

HPD settings: 5s scan time, voltage of 40kV at 5mA and a scan frame of 110x40 mm with a step size of 1mm. Mostly homogenous distribution, only a small artifact is visible in the center with slightly higher intensity.
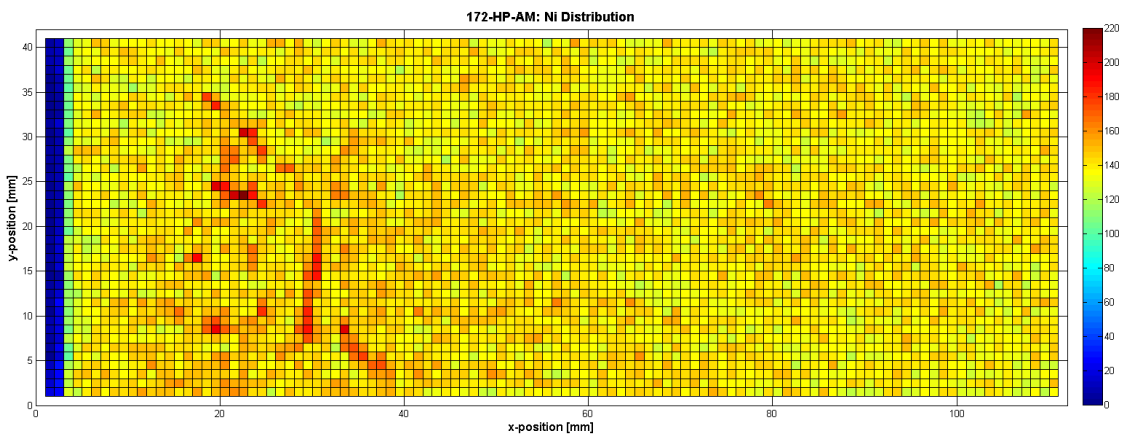
Figure 5.15: **Detailed nickel color map of the 2nd section**

HPD settings: 5s scan time, voltage of 40kV at 5mA and a scan frame of 110x40 mm with a step size of 1mm. One major artifact is clearly visible with a dimension of roughly 20x35mm located approximately at the middle between inner and outer diameter.
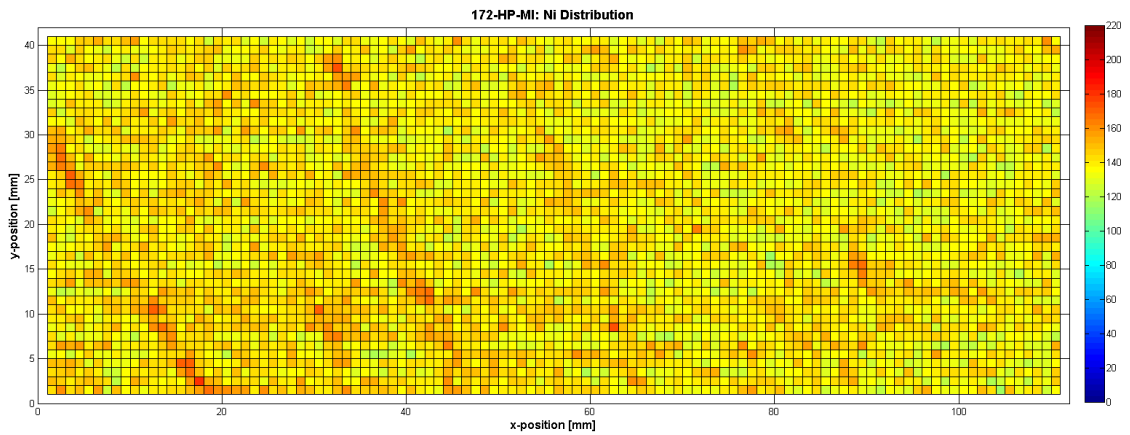
Figure 5.16: **Detailed nickel color map of the 3rd section**

HPD settings: 5s scan time, voltage of 40kV at 5mA and a scan frame of 110x40 mm with a step size of 1mm. Several linear artifact lines are scattered accross this section and are visible on the Mn map as well.
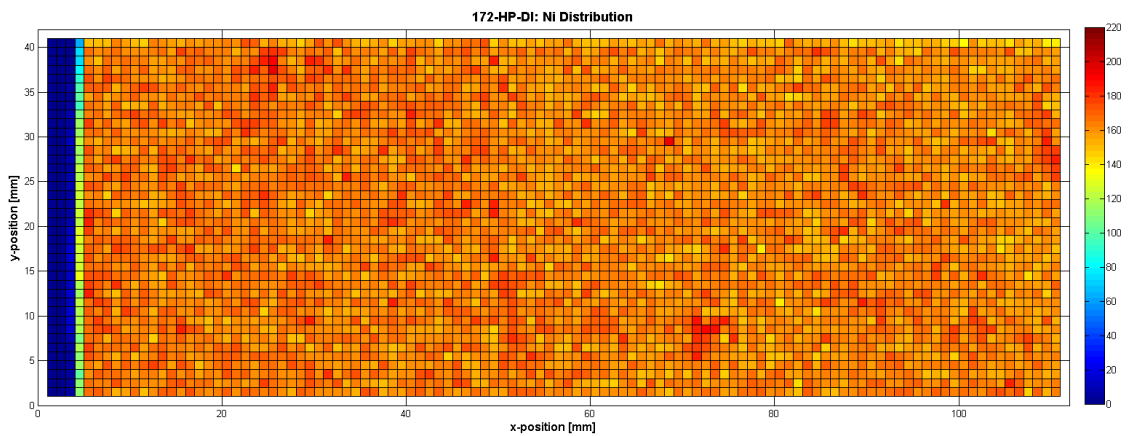

Figure 5.17: **Detailed nickel color map of the 4th section**

HPD settings: 5s scan time, voltage of 40kV at 5mA and a scan frame of 110x40 mm with a step size of 1mm. Mostly homogenous distribution. The dark artifact at x=70, y=10 is visible on the Mn map as well. The higher intensity in this section may be caused by a different distance between the prisma and the sample resulting in slightly better focus.
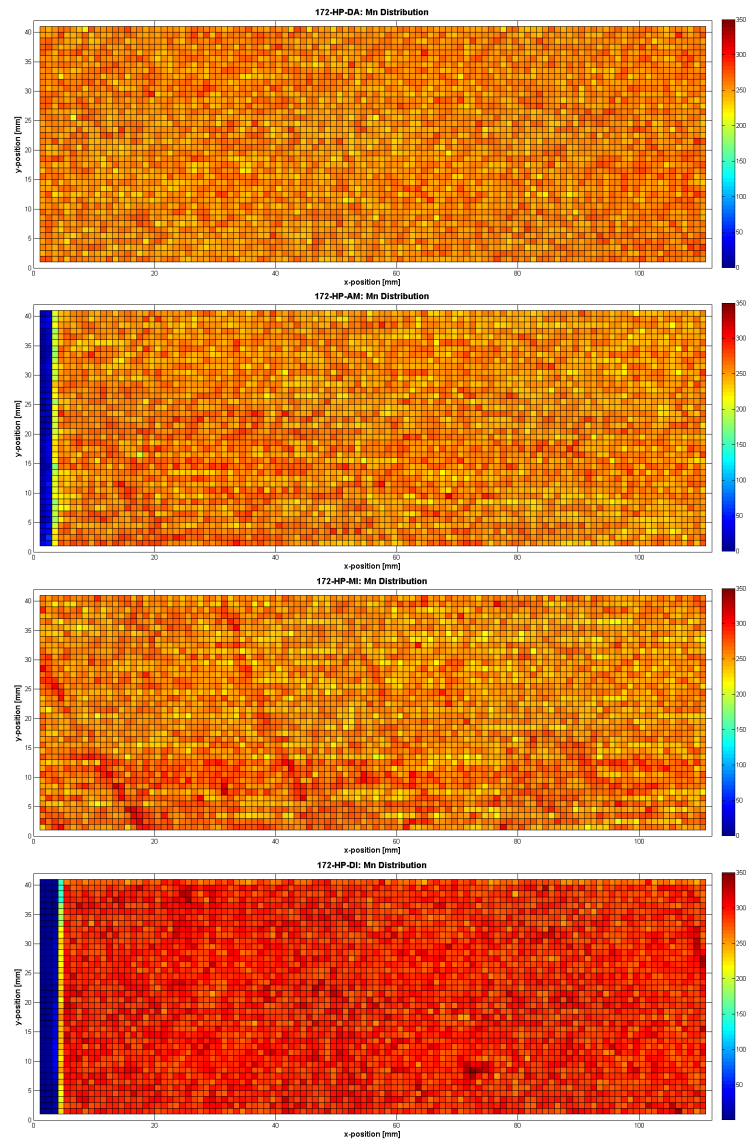
Figure 5.18: **Elemental distribution of Mn from top=1 to bottom=4**

Manganese distribution of the complete cross section from the outer diameter=1=top to the inner diameter=4=bottom as depicted in figure 5.12. The intensity color scale is the same on each image. Much more homogenous distribution than nickel. The reason for the higher intensities on the last image might be due to a different distance between the prisma and the steel sample resulting in a slightly better focus.
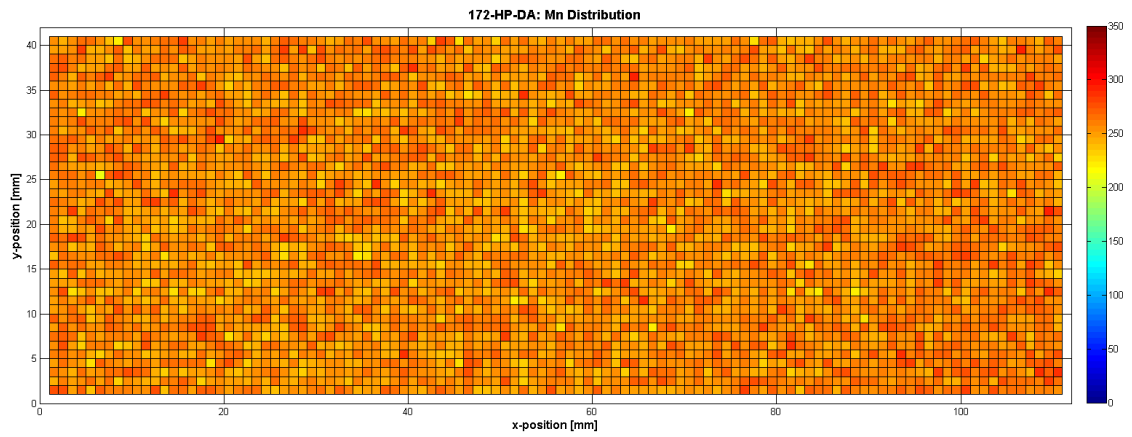
Figure 5.19: **Detailed manganese color map of the 1st section**

HPD settings: 5s scan time, voltage of 40kV at 5mA and a scan frame of 110x40 mm with a step size of 1mm. Mostly homogenous distribution.
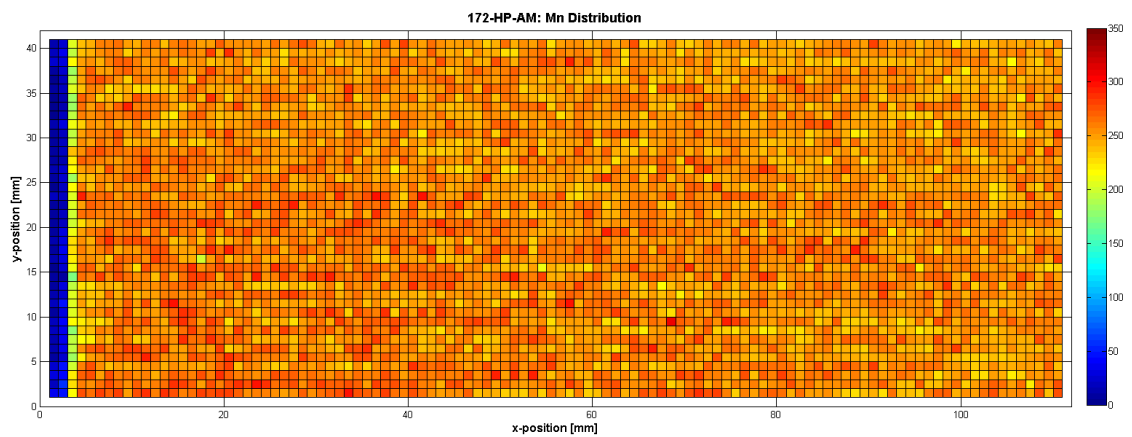

Figure 5.20: **Detailed manganese color map of the 2nd section**

HPD settings: 5s scan time, voltage of 40kV at 5mA and a scan frame of 110x40 mm with a step size of 1mm. Mostly homogenous distribution.
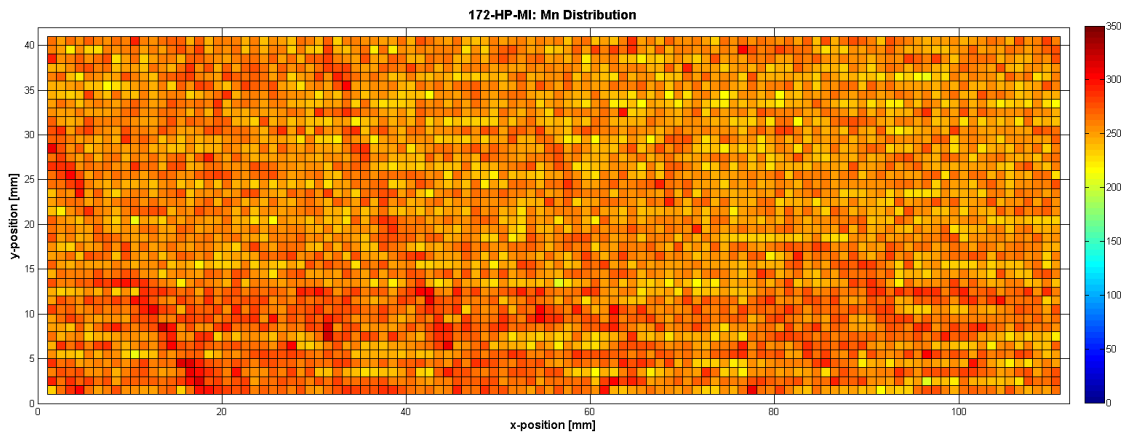
Figure 5.21: **Detailed manganese color map of the 3rd section**

HPD settings: 5s scan time, voltage of 40kV at 5mA and a scan frame of 110x40 mm with a step size of 1mm. Several linear artifact lines are scattered accross this section and are visible on the Ni map as well.
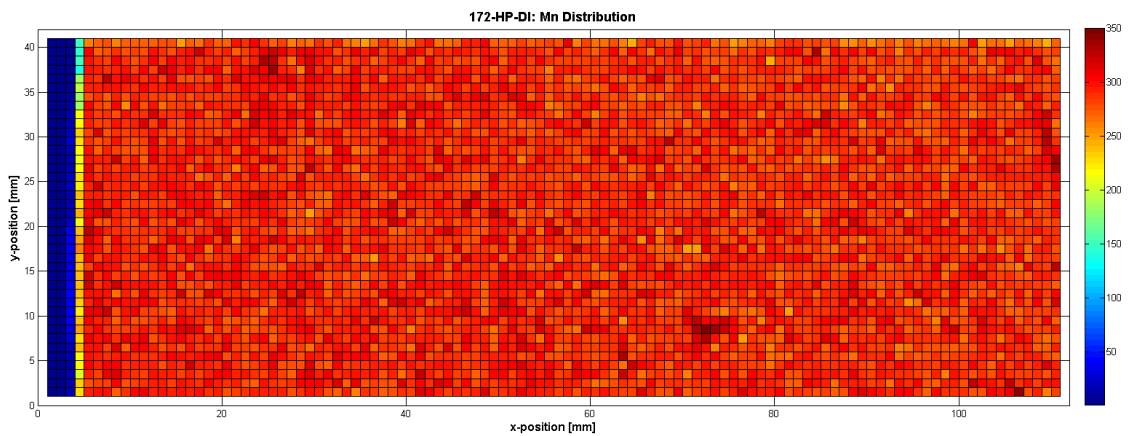
Figure 5.22: **Detailed manganese color map of the 4th section**

HPD settings: 5s scan time, voltage of 40kV at 5mA and a scan frame of 110x40 mm with a step size of 1mm. Mostly homogenous distribution. The dark artifact at x=70, y=10 is visible on the Ni map as well. The higher intensity in this section may be caused by a different distance between the prisma and the sample resulting in slightly better focus.

5.4.2 Low power

The other test piece supplied by *Breitenfeld Edelstahl AG* [47] is a much smaller forging product with a cross section of only 232x42 mm and a much higher alloy content. Known as X5CrNiCuNb17-4-4, 1.4548 or AISI 630, the martensitic chromium-nickel stainless steel consists, in this case, of 15.36% chromium, 4.27% nickel, 3.61% copper, 0.274% niobium and 0.77% manganese. Because of this smaller scan area, approximately half of the sample (120x42 mm) was scanned with the low power configuration and evaluated in AXIL and MATLAB. The distribution of the elements Cr, Ni, Mn and Cu are depicted and described in the following images.


(a) Cr distribution

(b) Ni distribution

(c) Mn distribution
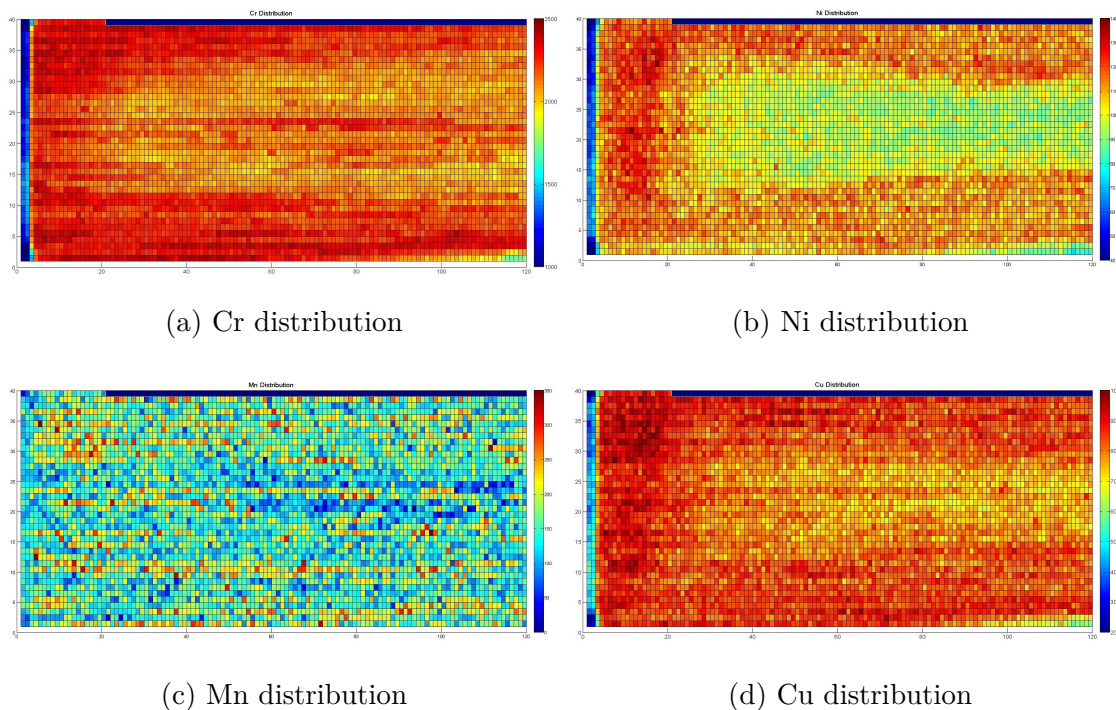
(d) Cu distribution

Figure 5.23: **Chemical distribution of the elements Cr, Ni, Mn and Cu**

Low power settings: 30s scan time, voltage of 40kV at 80μA and a scan frame of 120x42 mm with a step size of 1mm.**(a)** chromium (Cr) distribution, **(b)** nickel (Ni) distribution, **(c)**, manganese (Mn) distribution and **(d)** copper (Cu) distribution.
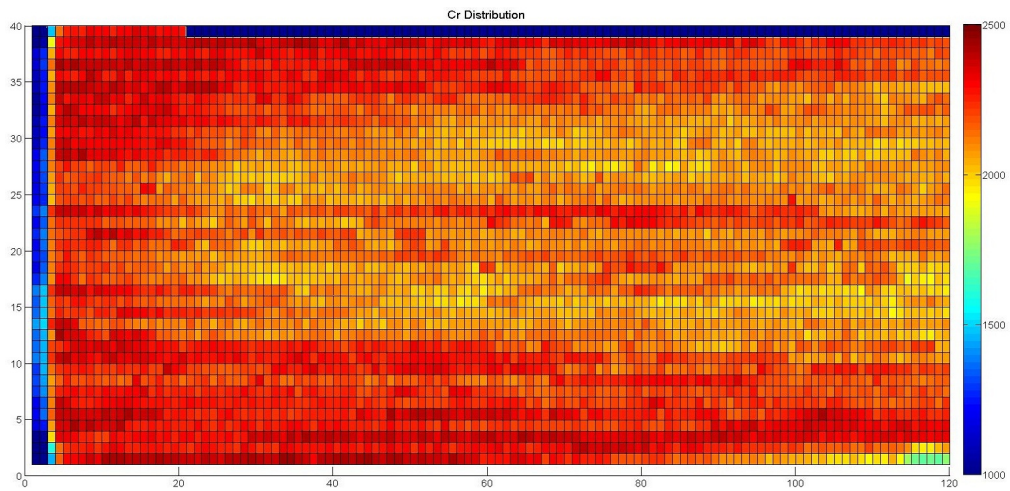
Figure 5.24: **Detailed chromium (Cr) color map of the steel forging**

LP settings: 30s scan time, voltage of 40kV at 80μA and a scan frame of 120x42 mm with a step size of 1mm. Clearly visible Cr depletion area in the middle. The same effect can be observed with Ni and Cu.
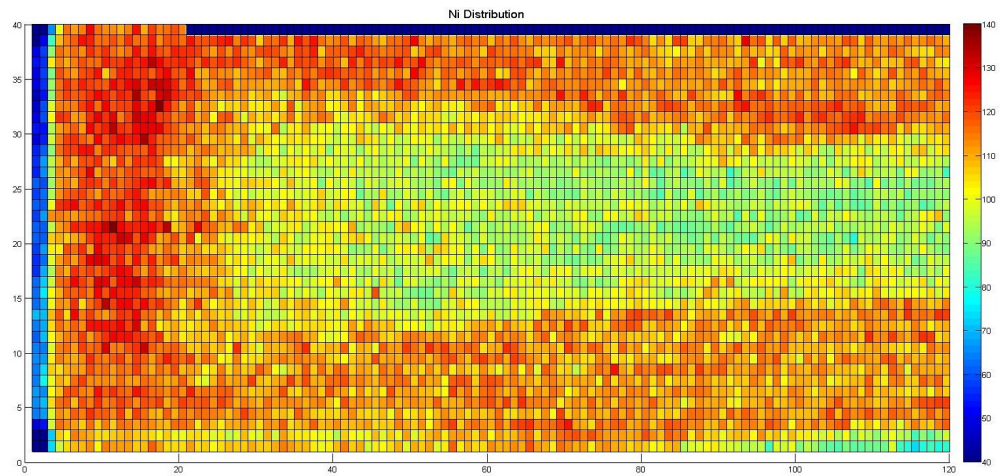
Figure 5.25: **Detailed nickel (Ni) color map of the steel forging**

LP settings: 30s scan time, voltage of 40kV at 80μA and a scan frame of 120x42 mm with a step size of 1mm. Clearly visible Ni depletion area in the middle. The same effect can be observed with Cr and Cu.
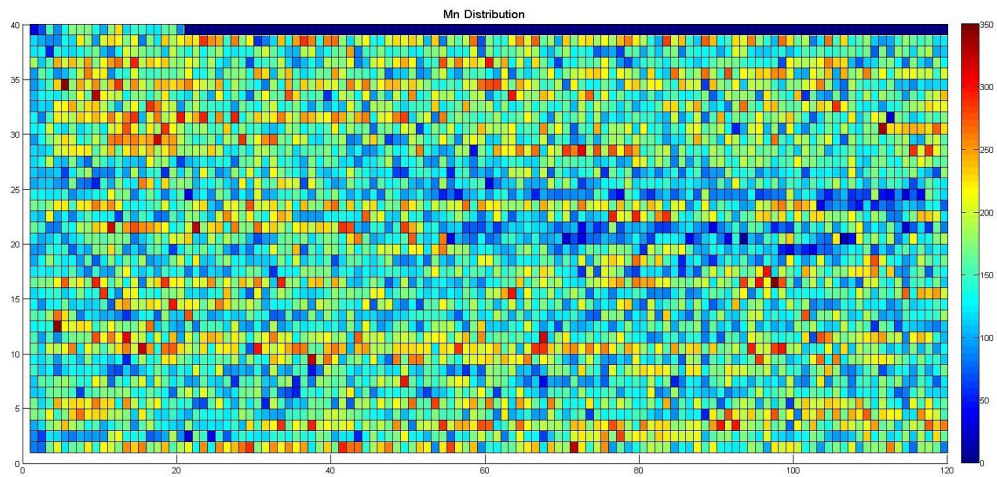
Figure 5.26: **Detailed manganese (Mn) color map of the steel forging**
LP settings: 30s scan time, voltage of 40kV at 80μA and a scan frame of 120x42 mm with a step size of 1mm. Mostly homogeneous distribution in contrast to the other elements Cr, Ni, Cu.
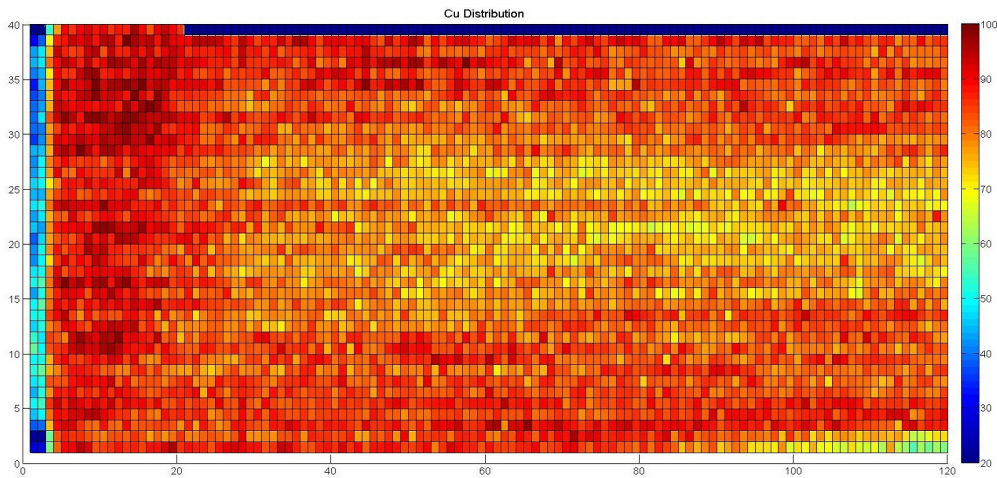
Figure 5.27: **Detailed copper (Cu) color map of the steel forging**
LP settings: 30s scan time, voltage of 40kV at 80μA and a scan frame of 120x42 mm with a step size of 1mm. Clearly visible Cu depletion area in the middle. The same effect can be observed with Ni and Cr.

Chapter 6

Conclusion and outlook

First and foremost the outcome of this thesis strongly supports the method of two dimensional makroskopic elemental mapping of various samples. In comparison of all three methods investigated, the high power direct configuration showed the highest potential. It combines short measuring times due to the high beam intensity, with the possibility to go to even smaller dimensions of the collimator as the flux would still be high enough. Furthermore the silver anode is very versatile and allows accurate analysis of most high Z elements, which is especially interesting for the steel industry. The only drawback is the necessity for water cooling and a bulky high voltage generator, which makes this system not really a portable design.

In contrast, the high power polarized set-up was not very promising, due to the very low count rates, which is rather unfortunate, as this method has the highest peak to background ratio because of the omission of the bremsstrahlung background.

Very promising on the other hand was the performance of the low power tube. Although only a device from the low power sector (4 Watt), the compact design and portability of this configuration makes it quite attractive for a lot of different applications. With a more powerful air cooled X-ray tube with a power around 35 Watt, it should be able to compete with the high power used in this work, because the exit window of the low power tube can be positioned much closer to the sample due to its small proportions and the inverse-square law comes to bear.

Quantitative analysis was no topic of this thesis, but as explained in the corresponding chapters, it is possible to evaluate every scan point using either the fundamental parameter method or the empirical coefficient method as applicable.

A possible topic for future investigations would be the application of X-ray optics, such as a poly-capillary and a comparison of the advantages in intensity and contrast against their costs. It shall be noted that with such a fine focus, large scan areas will take a lot of time and therefore a balance has to be found between applicable resolution for a macroscopic scan and possible resolution power, as other existing methods cover smaller, μm scale structures.

Another factor is the time consumption of an area scan. In regard to the elemental concentration that has to be mapped, the scan time per point cannot be reduced for a given radiation power. The time it takes to move from one spot to the next however can be reduced by implementing so called on-the-fly measurement techniques, where the beam is constantly and evenly moved across the sample material and the computer provides accurate deconvolution of the data.

The use of a large area SDD of up to $100mm^2$ in combination with a fast digital pulse processing unit will further improve the above mentioned features and possible applications of a low power tube.

Appendix

1 Arduino
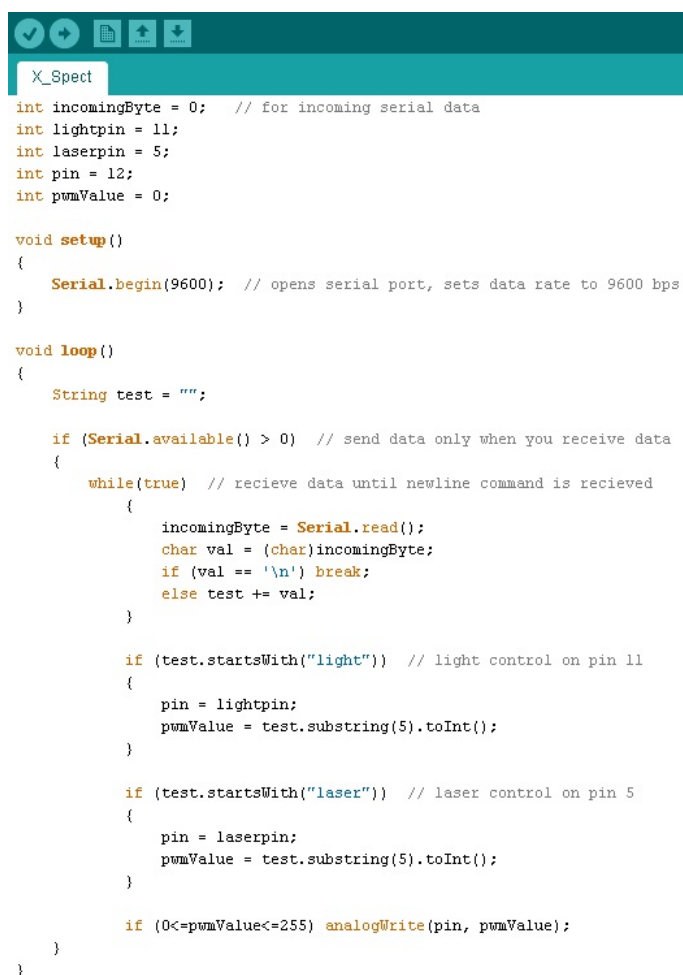
```
int incomingByte = 0;    // for incoming serial data
int lightpin = 11;
int laserpin = 5;
int pin = 12;
int pwmValue = 0;

void setup()
{
    Serial.begin(9600);  // opens serial port, sets data rate to 9600 bps
}

void loop()
{
    String test = "";

    if (Serial.available() > 0)  // send data only when you receive data
    {
        while(true)  // recieve data until newline command is recieved
        {
            incomingByte = Serial.read();
            char val = (char)incomingByte;
            if (val == '\n') break;
            else test += val;
        }

        if (test.startsWith("light"))  // light control on pin 11
        {
            pin = lightpin;
            pwmValue = test.substring(5).toInt();
        }

        if (test.startsWith("laser"))  // laser control on pin 5
        {
            pin = laserpin;
            pwmValue = test.substring(5).toInt();
        }

        if (0<=pwmValue<=255) analogWrite(pin, pwmValue);
    }
}
```

2 Program code

```
232         // Code below added from Allinger Peter ------------------------
233         public Bitmap CamImage;
234         private VideoCaptureDevice videoSource = null; // Initializes Object
235
236             private void WebcamAquire_Click(object sender, EventArgs e)
237             {
238                 FilterInfoCollection videoDevices = new FilterInfoCollection      ↙
        (FilterCategory.VideoInputDevice); // enumerate video devices
239                 if (videoDevices != null) // create video source if there is at least ↙
        one!
240                 {
241                     try
242                     {
243                         videoSource = new VideoCaptureDevice(videoDevices[0].        ↙
        MonikerString); // Always 1st device is selected
244                         videoSource.NewFrame += new AForge.Video.NewFrameEventHandler ↙
        (videoSource_NewFrame);
245                         videoSource.Start(); // Start the device
246                     }
247                     catch
248                     {
249                         MessageBox.Show("Webcam Error", "Could not connect to Webcam, ↙
        check if drivers are installed correctly!", MessageBoxButtons.OK, MessageBoxIcon. ↙
        Error, MessageBoxDefaultButton.Button1);
250                     }
251                 }
252             }
253
254         private void WebcamBtnStop_Click(object sender, EventArgs e)
255         {
256             if (videoSource != null && videoSource.IsRunning)
257             {
258                 videoSource.SignalToStop();
259                 videoSource = null;
260             }
261
262             WebcamBox.BackgroundImage.Dispose();
263             WebcamBox.BackgroundImage = null;
264         }
265
266         void videoSource_NewFrame(object sender, AForge.Video.NewFrameEventArgs     ↙
        eventArgs)
267         {
268             CamImage = (Bitmap)eventArgs.Frame.Clone(); //Jedes ankommende Objekt ↙
        als Bitmap casten und der Picturebox zuweisen
269             WebcamBox.BackgroundImage = CamImage; //(Denkt an das ".Clone()", um  ↙
        Zugriffsverletzungen aus dem Weg zu gehen.)
270         }
271
272         private void ScreenshotBtn_Click(object sender, EventArgs e)
273         {
274             if (dialogss.ShowDialog() == DialogResult.OK) CamImage.Save(dialogss. ↙
        FileName, System.Drawing.Imaging.ImageFormat.Jpeg);
275         }
276
277         private void buttonNewAquireStartStop_Click(object sender, EventArgs e) //↙
         Neue Einzelmessung
278         {
279             if (!connected) MessageBox.Show("MCA not connected! Nothing has been  ↙
        done!", "Warning", MessageBoxButtons.OK, MessageBoxIcon.Information,           ↙
        MessageBoxDefaultButton.Button1);
280
281             if (counting) // Button ist Start/Stop je nachdem was gerade gemacht  ↙
        wird
282             {
283                 labelAcquisitionStatus.Text = "Stopping...";
284                 mca.mcaStopAcquire();
285             }
286             else // Hier wird Einzelmessung gestartet
287             {
288                 if(checkBox_compSpec.Checked) spectrumOld.Data = spectrum.Data;
289                 labelAcquisitionStatus.Text = "Acquiring...";
290                 uint time = Convert.ToUInt32(textBoxAcquisitionTime.Text);
291                 RemoteCountAndSave(txtDirectory.Text, "nix", "nix", µXRF.Enums. ↙
```

```
   C:\Documents and Settings\XPMUser\Desktop... Peter V1.0\X-Spect\formMainXSpect.cs     2

       AcquisitionTimers.Realtime, time, new List<string>()); // nix ist wichtig!!
292                    remoteCountAndSave = false; // Damit nicht automatisch gespeichert↵
       wird
293                }
294            }
295
296        private void btnSaveSingleSpectrum_Click(object sender, EventArgs e)
297        {
298            if (dialogSingleMeasurement.ShowDialog() == DialogResult.OK)
299            {
300                string scanCurrentDirectory = System.IO.Path.GetDirectoryName ↵
       (dialogSingleMeasurement.FileName);
301                string scanFilenumber =  System.IO.Path.GetFileName ↵
       (dialogSingleMeasurement.FileName);
302                string reportFile = System.IO.Path.Combine(scanCurrentDirectory, ↵
       scanFilenumber + "-report.txt");
303                string ScreenshotFilename = System.IO.Path.Combine ↵
       (scanCurrentDirectory, scanFilenumber + "-image.jpg");
304                string SpectrumFilename = System.IO.Path.Combine ↵
       (scanCurrentDirectory, scanFilenumber + "-spectrum." + autoWriteFormat.ToString())↵
       ; //last part adds Filetype
305
306                if (checkBoxOptionsSecondarySave.Checked) SpectrumFilename = ↵
       System.IO.Path.Combine(scanCurrentDirectory, scanFilenumber + "-spectrum." + ↵
       secondaryWriteFormat.ToString()); //last part adds Filetype
307
308                using (System.IO.StreamWriter sw = new System.IO.StreamWriter ↵
       (reportFile)) // Save Report
309                {
310                    string reportText = textBoxReport.Text;
311                    reportText = reportText.Substring(reportText.IndexOf("---↵
       Acquisition ---"));
312                    sw.Write(reportText);
313                }
314
315                SpectrumFiles.write(autoWriteFormat, SpectrumFilename, header, ↵
       spectrum.Data, realtime, livetime, DateTime.Now); // Save Spectrum
316
317                if (videoSource != null && videoSource.IsRunning) CamImage.Save ↵
       (ScreenshotFilename, System.Drawing.Imaging.ImageFormat.Jpeg); // Save Screenshot
318            }
319        }
320
321        private void btnOpenExplorer_Click(object sender, EventArgs e)
322        {
323            string fileToSelect = txtDirectory.Text;
324            System.Diagnostics.ProcessStartInfo pfi = new System.Diagnostics. ↵
       ProcessStartInfo("Explorer.exe", fileToSelect);
325            System.Diagnostics.Process.Start(pfi);
326        }
327
328        // Arduino Micro communication-------------
329        public System.IO.Ports.SerialPort arduinoport { get; set; }
330
331        private string getAllComPorts()
332        {
333            string ports = "";
334            using (ManagementObjectSearcher searcher = new ↵
       ManagementObjectSearcher("SELECT * FROM WIN32_SerialPort"))
335            {
336                foreach (ManagementObject serialPortObj in searcher.Get())
337                {
338                    ports += Convert.ToString(serialPortObj.GetPropertyValue("Name↵
       ")) + "\n";
339                }
340            }
341            return ports;
342        }
343
344        private void btnArduinoStart_Click(object sender, EventArgs e)
345        {
346            bool arduinofound = false;
347            arduinoport = new SerialPort(); // Create a new SerialPort object with↵
       default settings.
```

```
348                 string[] portnames = getAllComPorts().Split('\n');
349                 foreach (string line in portnames) //Querries COM Devices for Arduino ↙
      and sets COM Ports, etc.
350                 {
351                     if (Regex.IsMatch(line, "arduino", RegexOptions.IgnoreCase))
352                     {
353                         arduinoport.PortName = line.Split('(')[1].Trim(')');
354                         arduinoport.BaudRate = 9600;
355                         arduinoport.Parity = Parity.None;
356                         arduinoport.DataBits = 8;
357                         arduinoport.StopBits = StopBits.One;
358                         arduinoport.Handshake = Handshake.None;
359                         arduinoport.ReadTimeout = 500;
360                         arduinoport.WriteTimeout = 500;
361                         arduinoport.Open();
362
363                         trackBarLight.Enabled = true;
364                         trackBarLaser.Enabled = true;
365
366                         arduinoport.WriteLine("light150");
367                         arduinoport.WriteLine("laser25");
368                         trackBarLaser.Value = 25;
369                         trackBarLaser.ValueChanged += this.trackBarLaser_Scroll;
370                         trackBarLight.Value = 150;
371                         trackBarLight.ValueChanged += this.trackBarLight_Scroll;
372
373                         arduinofound = true;
374                     }
375                 }
376                 if (arduinofound==false) MessageBox.Show("No Arduino found, check if ↙
      connected!", "Error", MessageBoxButtons.OK, MessageBoxIcon.Error,                ↙
      MessageBoxDefaultButton.Button1);
377             }
378
379         private void btnArduinoStop_Click(object sender, EventArgs e)
380         {
381             if (arduinoport != null && arduinoport.IsOpen)
382             {
383                 arduinoport.WriteLine("light0");
384                 arduinoport.WriteLine("laser0");
385                 trackBarLaser.Value = 0;
386                 trackBarLaser.ValueChanged += this.trackBarLaser_Scroll;
387                 trackBarLight.Value = 0;
388                 trackBarLight.ValueChanged += this.trackBarLight_Scroll;
389                 arduinoport.Close();
390             }
391
392             trackBarLight.Enabled = false;
393             trackBarLaser.Enabled = false;
394         }
395
396         private void trackBarLight_Scroll(object sender, EventArgs e)
397         {
398             try
399             {
400                 arduinoport.WriteLine("light" + Convert.ToString(trackBarLight. ↙
      Value));
401             }
402             catch
403             {
404                 trackBarLight.Enabled = false;
405                 trackBarLaser.Enabled = false;
406                 MessageBox.Show("Check if Arduino is connected!", "Error",          ↙
      MessageBoxButtons.OK, MessageBoxIcon.Error, MessageBoxDefaultButton.Button1);
407             }
408         }
409
410         private void trackBarLaser_Scroll(object sender, EventArgs e)
411         {
412             try
413             {
414                 arduinoport.WriteLine("laser" + Convert.ToString(trackBarLaser. ↙
      Value));
415             }
```

```
416                catch
417                {
418                    trackBarLaser.Enabled = false;
419                    trackBarLight.Enabled = false;
420                    MessageBox.Show("Check if Arduino is connected", "Error",    ⤶
        MessageBoxButtons.OK, MessageBoxIcon.Error, MessageBoxDefaultButton.Button1);
421                }
422            }
423
424        public struct ElementTable
425        {
426            public string El_Name;
427            public List<string> El_Line;
428            public List<float> El_Line_Energy;
429            public List<float> El_Line_Prob;
430        }
431
432        public ElementTable[] PeriodicTable = new ElementTable[92];
433
434        public void readElementList()
435        {
436            try
437            {
438                System.IO.StreamReader ElementList = new System.IO.StreamReader    ⤶
        (System.IO.Path.Combine(AppDomain.CurrentDomain.BaseDirectory, "HEAVYELE.txt")); /⤶
        /Application.StartupPath
439
440                string sLine = "";
441                string[] Line_split = null;
442
443                for (int e = 0; e < 92; ++e)
444                {
445                    PeriodicTable[e].El_Line = new List<string>();
446                    PeriodicTable[e].El_Line_Energy = new List<float>();
447                    PeriodicTable[e].El_Line_Prob = new List<float>();
448                }
449                int i = 0;
450                do
451                {
452                    sLine = ElementList.ReadLine();
453                    if (sLine == null) break;
454                    Line_split = sLine.Split((char[])null, StringSplitOptions.    ⤶
        RemoveEmptyEntries);
455                    if (Line_split.Length == 2) PeriodicTable[i].El_Name =    ⤶
        Line_split[0];
456                    if (Line_split.Length == 3)
457                    {
458                        PeriodicTable[i].El_Line.Add(Line_split[0]);
459                        PeriodicTable[i].El_Line_Energy.Add(float.Parse(Line_split⤶
        [1]));
460                        PeriodicTable[i].El_Line_Prob.Add(float.Parse(Line_split    ⤶
        [2]));
461                    }
462                    if (Line_split.Length == 4) i += 1;
463                } while (sLine != null);
464                ElementList.Close();
465            }
466            catch { }
467        }
468
469        private void buttonKLM_Click(object sender, EventArgs e)
470        {
471
472
473
474            if (buttonKLM.BackColor == Color.Green)
475            {
476                KLM = false;
477            }
478            if (buttonKLM.BackColor == SystemColors.Control)
479            {
480                KLM = true;
481            }
482            if (KLM)
```

```
483                    {
484                        try
485                        {
486                            readElementList();
487                            buttonKLM.BackColor = Color.Green; // Toggle Switch
488                            KLM_Element.BackColor = Color.LightBlue;
489                            KLM_Z.BackColor = Color.LightBlue;
490                            this.ActiveControl = null; // Setzt den Focus auf nichts!
491                        }
492                        catch
493                        {
494                            KLM = false;
495                            MessageBox.Show("No Spectrum Data or corrupt file! Make shure ↵
        HEAVYELE.txt is in the right directory!", "Error", MessageBoxButtons.OK,          ↵
        MessageBoxIcon.Error, MessageBoxDefaultButton.Button1);
496                        }
497                    }
498                    if (!KLM)
499                    {
500                        buttonKLM.BackColor = SystemColors.Control;
501                        KLM_Element.BackColor = SystemColors.Control;
502                        KLM_Z.BackColor = SystemColors.Control;
503                    }
504                }
505
506            private void drawKLM(int z)
507            {
508                pictureBoxOverlay.Parent = pictureBoxSpectrum;
509                pictureBoxOverlay.Size = spectrumBox.Size;
510                pictureBoxOverlay.Location = spectrumBox.Location;
511                pictureBoxOverlay.BackColor = Color.Transparent;
512                overlay = new Bitmap(spectrumBox.Width, spectrumBox.Height);
513                pictureBoxOverlay.Image = overlay;
514
515                Graphics gr = Graphics.FromImage(overlay);
516                gr.SmoothingMode = System.Drawing.Drawing2D.SmoothingMode.AntiAlias;
517
518                Font xFont = new Font("Arial", 12);
519                Brush xBrush = Brushes.Red;
520                StringFormat xStringFormat = new StringFormat();
521                xStringFormat.Alignment = StringAlignment.Center;
522                xStringFormat.LineAlignment = StringAlignment.Far;
523
524                KLM_Element.Text = PeriodicTable[z].El_Name;
525                KLM_Z.Text = Convert.ToString(z + 1);
526
527                try // Weil bei ein paar Elementen keine Linien in Tabelle sind
528                {
529                    gr.DrawString(PeriodicTable[z].El_Name, xFont, xBrush, new PointF ↵
        (xFromChannel(channelFromEnergy(PeriodicTable[z].El_Line_Energy[0])), 40),       ↵
        xStringFormat);
530                    ulong KaMax = 0;
531                    if (Convert.ToInt32(textBoxEditMaxChannel.Text) <= Convert.ToInt32↵
        (channelFromEnergy(PeriodicTable[z].El_Line_Energy[0]))) KaMax = 0;
532                    else KaMax = spectrum.Data[Convert.ToInt32(channelFromEnergy       ↵
        (PeriodicTable[z].El_Line_Energy[0]))]; // Gibt die Counts an der Stelle der Ka1  ↵
        Linie des Elements z
533                    int x = 0;
534                    int y = 0;
535                    float yscale = 1;
536
537                    for (int i = 0; i < PeriodicTable[z].El_Line.Count; i++) // Loop    ↵
        über alle Linien des Elementes
538                    {
539                        x = xFromChannel(channelFromEnergy(PeriodicTable[z].           ↵
        El_Line_Energy[i]));
540                        if (Convert.ToInt32(yFromCounts(KaMax)) < 0.85 * overlay.       ↵
        Height)
541                        {
542                            yscale = PeriodicTable[z].El_Line_Prob[i] / PeriodicTable  ↵
        [z].El_Line_Prob[0]; // skaliert Ka1=MaxCounts=100%
543                            if (yscale > 1) yscale = PeriodicTable[z].El_Line_Prob[i];↵
         // Naja, solange mir nichts besseres einfällt
544                            y = yFromCounts(Convert.ToUInt32(KaMax * yscale)); // Wenn ↵
```

```
        Peak da, der größer als 15%
545                           }
546                     else y = Convert.ToInt32(overlay.Height - (overlay.Height / 3. ↙
      0) * PeriodicTable[z].El_Line_Prob[i]); // Ansonsten Höhe nach Wahrscheinlichkeit, ↙
       durch 3
547                     gr.DrawLine(Pens.Red, new Point(x, pictureBoxOverlay.Bottom), ↙
      new Point(x, y));
548                           }
549                 }
550             catch { }
551         }
552
553         private void formMainXSpect_PreviewKeyDown(object sender,                    ↙
      PreviewKeyDownEventArgs e)
554         {
555             if (e.KeyCode.Equals(Keys.Left) || e.KeyCode.Equals(Keys.Right))
556             {
557                 e.IsInputKey = true;
558             }
559         }
560
561         private void formMainXSpect_KeyDown(object sender, KeyEventArgs e)
562         {
563             if (e.KeyCode.Equals(Keys.Left))
564             {
565                 e.Handled = true;
566                 if (!KLM)
567                 {
568                     if (cursorPosition > 0) cursorPosition -= 1;
569                     cursorPositionChanged();
570                 }
571                 else
572                 {
573                     if (ElementZ > 2) ElementZ -= 1;
574                     if (ElementZ == 2) ElementZ = 91;
575                     drawKLM(ElementZ);
576                 }
577             }
578             if (e.KeyCode.Equals(Keys.Right))
579             {
580                 e.Handled = true;
581                 if (!KLM)
582                 {
583                     if (cursorPosition < spectrum.Size - 1) cursorPosition += 1;
584                     cursorPositionChanged();
585                 }
586                 else
587                 {
588                     if (ElementZ < 91) ElementZ += 1;
589                     if (ElementZ == 91) ElementZ = 2;
590                     drawKLM(ElementZ);
591                 }
592             }
593         }
594
595         private void safetyLimitsToolStripMenuItem_Click(object sender, EventArgs ↙
      e) //Dropdown Menü --> XY-Schlitten Limits
596         {
597             using (var popup = new Limits(x_limit / (-101), y_limit / (-202)))
598             {
599                 DialogResult dialogresult = popup.ShowDialog();
600                 if (dialogresult == DialogResult.OK)
601                 {
602                     x_limit = popup.x_limit1 * (-101);
603                     y_limit = popup.y_limit1 * (-202);
604                 }
605                 popup.Dispose();
606             }
607         }
608         // Code above added from Allinger Peter ------------------------
```

3 Collimator

$\varnothing 15$

A | A

$\varnothing 10{,}10$

$\varnothing 1$

5

28

$\varnothing 5$

18

A-A

					ENTGRATEN	ZEICHNUNG NICHT SKALIEREN	ÄNDERUNG	
WENN NICHT ANDERS DEFINIERT: BEMASSUNGEN SIND IN MILLIMETER OBERFLÄCHENBESCHAFFENHEIT: TOLERANZEN: LINEAR: WINKEL:		OBERFLÄCHENGÜTE:			UND SCHARFE KANTEN BRECHEN			
	NAME	SIGNATUR	DATUM			BENENNUNG:		
GEZEICHNET								
GEPRÜFT								
GENEHMIGT								
PRODUKTION								
QUALITÄT			WERKSTOFF:			ZEICHNUNGSNR.	Kollimator	A4
			GEWICHT:			MASSSTAB:2:1	BLATT 1 VON 1	

4 45 degree mount

12,50

M6

15

125

150

30,50

65

4

19

105

	NAME	SIGNATUR	DATUM				BENENNUNG:		
GEZEICHNET									
GEPRÜFT									
GENEHMIGT									
PRODUKTION									
QUALITÄT				WERKSTOFF:			ZEICHNUNGSNR.	Flügel01	A4
				GEWICHT:			MASSSTAB:1:2		BLATT 1 VON 1

WENN NICHT ANDERS DEFINIERT:
BEMASSUNGEN SIND IN MILLIMETER
OBERFLÄCHENBESCHAFFENHEIT:
TOLERANZEN:
  LINEAR:
  WINKEL:

OBERFLÄCHENGÜTE:

ENTGRATEN
UND SCHARFE
KANTEN
BRECHEN

ZEICHNUNG NICHT SKALIEREN

ÄNDERUNG

B-B (1 : 1)

Ø 11

10

Ø 6,60

150

125

12,50

B

B

50

20

Ø 5

A (1 : 1)

20

24

15

45°

Basisplatte

ÄNDERUNG

ZEICHNUNG NICHT SKALIEREN

BENENNUNG:

ENTGRATEN
UND SCHARFE
KANTEN
BRECHEN

OBERFLÄCHENGÜTE:

WENN NICHT ANDERS DEFINIERT:
BEMASSUNGEN SIND IN MILLIMETER
OBERFLÄCHENBESCHAFFENHEIT:
TOLERANZEN:
LINEAR:
WINKEL:

NAME   SIGNATUR   DATUM

GEZEICHNET

GEPRÜFT

GENEHMIGT

PRODUKTION

QUALITÄT

WERKSTOFF:

GEWICHT:

ZEICHNUNGSNR.

MASSTAB:1:1

A3

BLATT 1 VON 1

5 High power prisma

6 Low power prisma

A-A (1:1)

B-B (1:1)

	NAME	SIGNATUR	DATUM				BENENNUNG:
GEZEICHNET							
GEPRÜFT							
GENEHMIGT							
PRODUKTION							
QUALITÄT							

WENN NICHT ANDERS DEFINIERT:
BEMASSUNGEN SIND IN MILLIMETER
OBERFLÄCHENBESCHAFFENHEIT:
TOLERANZEN:
  LINEAR:
  WINKEL:

OBERFLÄCHENGÜTE:

ENTGRATEN
UND SCHARFE
KANTEN
BRECHEN

ZEICHNUNG NICHT SKALIEREN   ÄNDERUNG

BENENNUNG:

Zentrales Prisma

WERKSTOFF:

ZEICHNUNGSNR.

A4

GEWICHT:

MASSSTAB: 1:1   BLATT 1 VON 2

30

15

M3

60

51

35,50

25,50

18

80

100

64

40

	NAME	SIGNATUR	DATUM				BENENNUNG:
GEZEICHNET							
GEPRÜFT							
GENEHMIGT							
PRODUKTION							
QUALITÄT							

WENN NICHT ANDERS DEFINIERT:
BEMASSUNGEN SIND IN MILLIMETER
OBERFLÄCHENBESCHAFFENHEIT:
TOLERANZEN:
  LINEAR:
  WINKEL:

OBERFLÄCHENGÜTE:

ENTGRATEN
UND SCHARFE
KANTEN
BRECHEN

ZEICHNUNG NICHT SKALIEREN

ÄNDERUNG

BENENNUNG:

Zentrales Prisma

WERKSTOFF:

ZEICHNUNGSNR.

A4

GEWICHT:

MASSSTAB: 1:1.5

BLATT 2 VON 2

7 Equipment datasheet - KETEK SDD

AXAS-D

Analytical X-ray Acquisition System

Digital

AXAS-D
digital

State of the Art Digital Detector System for your Application

- Complete digital acquisition system

- VITUS SDD sizes from 7 to 50 mm² available

- Including KETEK Digital Pulse Processor (DPP)

- KETEK reset type pre-amplifier

- Highly integrated design with regulated power supplies for TEC and SDD

- Finger lengths from 50 to 300 mm

- Software controlled settings and read-outs

- USB 2.0 full speed interface

- Windows XP data acquisition Software including DLL

Typical Spectrum acquired with AXAS-D & VITUS H30 SDD

40 mm² SDD
collimated to 30 mm²
10 kcps ICR
FWHM 130.2 eV
P/B 13700

AXAS-D with VITUS H30 SDD
ICR 10kcps
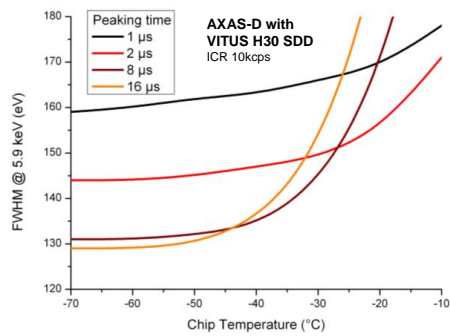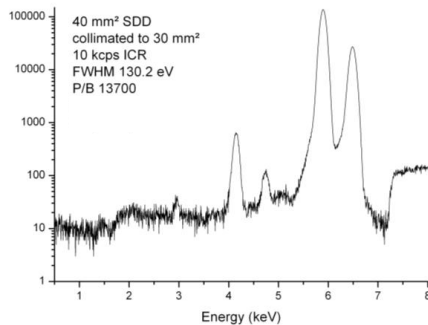
Energy Resolution vs Input Count Rate

40 mm² SDD
collimated to 30 mm²
Chip temperature -55°C

Dead time <50%

Peaking Time:
- 1µs
- 2 µs
- 4 µs
- 8 µs
- 16 µs
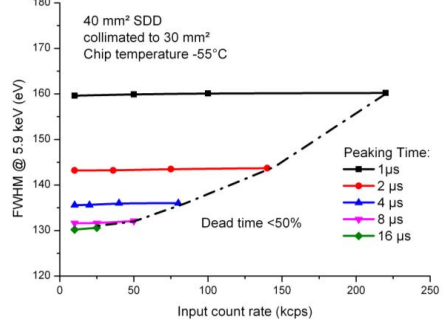
Peak Shift vs Input Count Rate

Peakshift < 0.5% up to 250 kcps

Peaking time
- 1 µs
- 8 µs
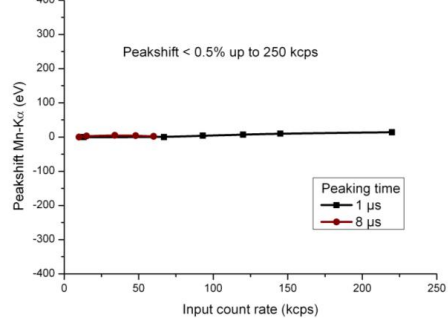
KETEK – accurate and reliable spectroscopy systems

KETEK
Creative Detector Solutions

ISO
9001:2008
CERTIFIED

www.ketek.net
info@ketek.net

AXAS-D
Analytical X-ray Acquisition System - Digital
Characteristics

AXAS-D Operation - Easy to Use

- Software controlled digital gain
- Software controlled threshold
- Software controlled peaking times
- Peaking times from 1.32 to 13.3 µs in 16 steps
- Built-in oscilloscope
- Integrated pulser
- 12 bit Analogue-to-Digital Converter (ADC)
- Implemented 8k Multi-Channel Analyzer (MCA)
- 25 MHz cycling frequency
- Pre-amplifier output
- Pulser input
- ±12 V power connection

Available Options

- **VITUS SDD**
  H7, H7LE*, H15LE*, H20, H30, H50
  * with low-energy window

- **Guaranteed FWHM [Mn Kα]**
  Premium Class   ≤ 133 eV*
  Standard Class   ≤ 139 eV*
  *≤ 136 eV and ≤ 144 eV for H15LE

- **Finger length [mm]**
  50, 100, 160, 200, 300

- **Upper energy limits**
  20 keV or 30 keV

- **Vacuum-tightness of snout**
  yes / no

AXAS-D Operation Block Diagram
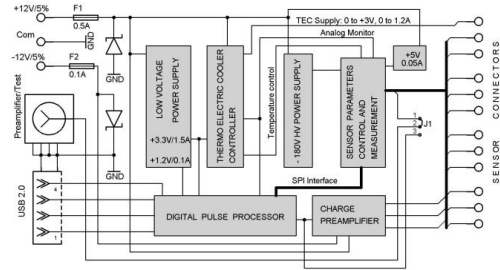
DPP Operation Block Diagram
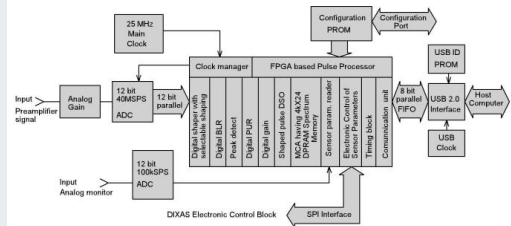
AXAS-D Housing Geometry [mm]

KETEK
Creative Detector Solutions

ISO
9001:2008
CERTIFIED

8 Equipment datasheet - AMPTEK Mini-X
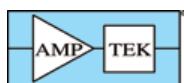
Miniature X- Ray Source

Mini–X

Mini–X is a self-contained, miniature X-ray tube system, which includes the X-ray tube, high voltage power supply and USB controller. Designed for X-ray fluorescence analysis applications - XRF.

Features
- 50 kV / 80 µA
- Ag or Au target
- USB controlled
- Stable output
- Fast
- Low power
- Small

Applications
- X-Ray Fluorescence (XRF) analysis
- Portable systems
- OEM
- Process Control
- Research
- Teaching

Mini-X is the first of its kind; a self-contained, packaged, miniature X-ray tube system, which includes the X-ray tube, the power supply, the control electronics and the USB communication to the computer. It is designed to replace radioisotopes in X-ray fluorescence analysis applications.

Mini-X has been designed to simplify the XRF process by providing a grounded anode, variable current and voltage controlled via USB and ease of operation. It features a 50 kV/80 µA power supply, a gold (Au) or silver (Ag) transmission target, and a beryllium end window. It is designed for continuous operation in industrial environments.

To further simplify the use of Mini-X an AC adaptor is provided to supply the 12 VDC needed to power the system. The only connections needed to operate the tube are a USB cable and AC adaptor. A flashing red LED and a beeper warns the user when x-rays are present.

Mini–X Output X-Ray Spectra

Ag Target @ 50 kV

Au Target @ 50 kV
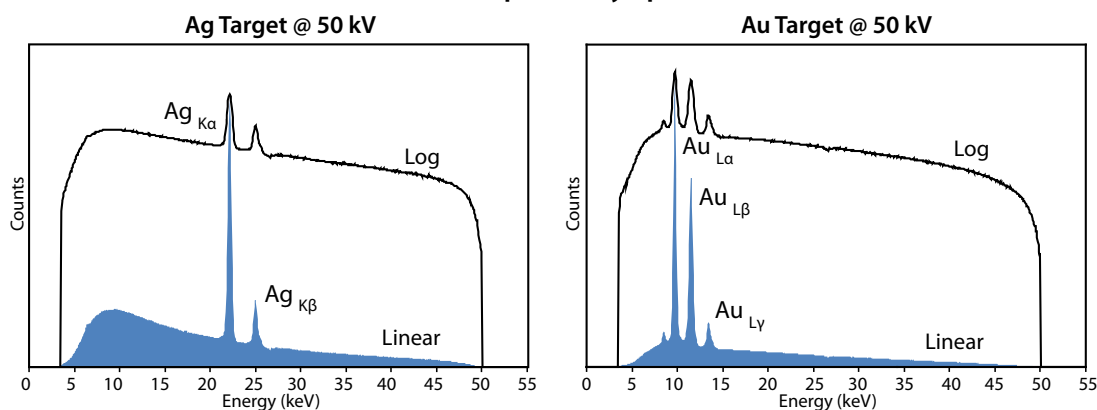
The Mini–X is based on the Newton Scientific Inc. miniature X-ray source.

Mini–X Specifications

Target Material	Silver (Ag)	Gold (Au)
Target Thickness	0.75 µm	1 µm
Tube Voltage	10 to 50 kV	10 to 50 kV
Tube Current	5 µA min. / 200 µA max.	5 µA min. / 200 µA max.
Approximate Dose Rate	10 Sv/h @ 30 cm	13 Sv/h @ 30 cm
Approximate Flux	10^6 counts per second/mm^2 on the axis at a distance of 30 cm (50 keV/1 µA)	1.3×10^6 counts per second/mm^2 on the axis at a distance of 30 cm (50 keV/1 µA)
Continuous Power	4 W max. @ 100% duty cycle	4 W max. @ 100% duty cycle
Window Material	Beryllium (Be); window at ground	Beryllium (Be); window at ground
Window Thickness	127 µm	127 µm
Focal Spot Size	Approximately 2 mm	Approximately 2 mm
Output Cone Angle	120°	120°
Cooling	Air cooled	Air cooled
High Voltage Stability	< 0.03% RSD	< 0.03% RSD
Leakage Radiation	<5 µSv/h (0.5 mrem/h) at 5 cm with safety plug installed	<5 µSv/h (0.5 mrem/h) at 5 cm with safety plug installed
Power Consumption	9 W at 50 kV and 80 µA	9 W at 50 kV and 80 µA
Input Voltage	12 VDC (AC adapter included), connector	12 VDC (AC adapter included), connector
Control	USB, mini-USB connector (cable included)	USB, mini-USB connector (cable included
Setting Time	Typical < 1 second	Typical < 1 second
Weight	360 g	360 g
Humidity	30 to 90% (non condensing)	30 to 90% (non condensing)
Operating Temperature	-10 °C to +50 °C	-10 °C to +50 °C
Storage Temperature	-25 °C to +60 °C	-25 °C to +60 °C
Safety Controls and Indicators	1) External hardware interlock 2) Flashing LED 3) Beeper	1) External hardware interlock 2) Flashing LED 3) Beeper
Software	Mini-X Control Software controls voltage and current Mini-X API for custom programming applications	Mini-X Control Software controls voltage and current Mini-X API for custom programming applications
Warranty	One year or 2000 hours, whichever comes first	One year or 2000 hours, whichever comes first

USB Software Interface. Allows the user to set the voltage and current as well as monitor both parameters.

Mini−X Mechanical Dimensions

120° X-Ray Cone

Be

Mini-X 120° cone.
NOTE: When using the 2 mm collimator,
the X-ray cone is 5°.

Dimensions in inches (mm)

1.125 (28.6)
1.329 (33.7)
22°
1.000 (25.4)
7.276 (184.8)
5.821 (147.8)
5.598 (142.2)
Ø0.120 (Ø3.0)
2.063 (52.4)
2.283 (58.0)

Mini-X Angular Response

Normalized Counts (%)

Degrees

Back panel connectors

PWR   USB   INTERLOCK   X-RAY ON

Flashing LED/Beeper
X-Rays ON
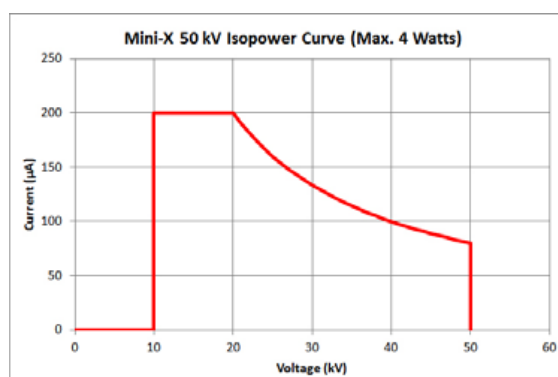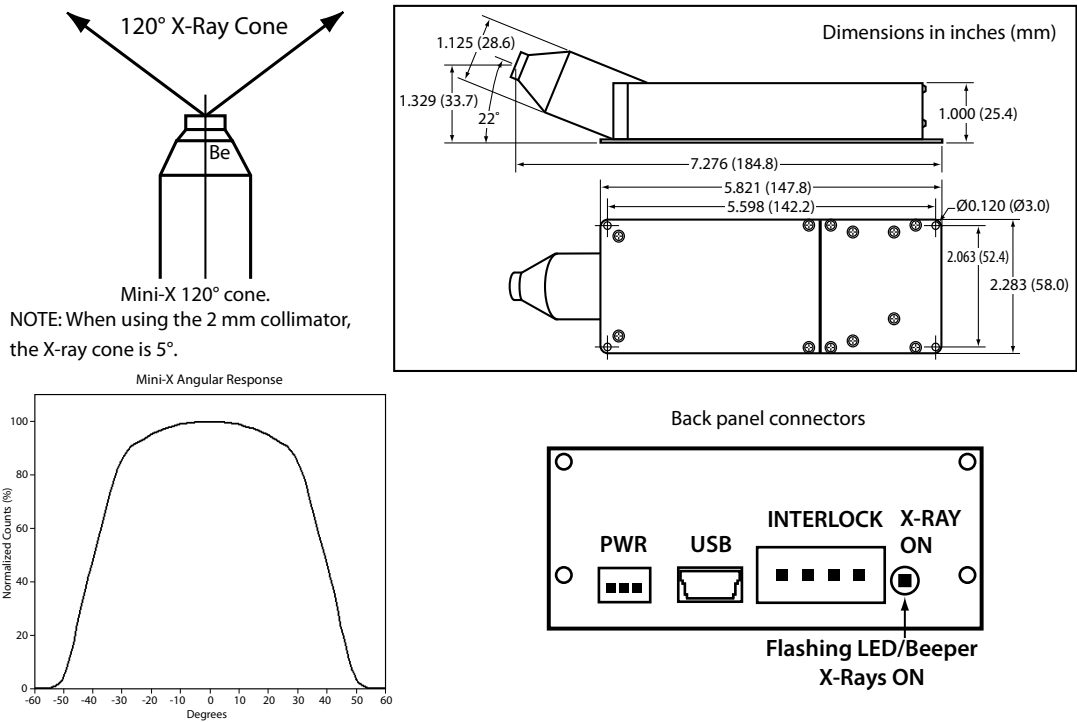
Collimator and Safety Plug

The Mini-X is provided with a collimator to facilitate its use in XRF applications. It consists of a brass collimator with an aluminum (Al) insert and a cover that screws into the Mini-X. The collimator has a 2 mm diameter hole. The brass safety plug when installed, reduces the flux from an operating tube to less than 2.5 mrem/h at 5 cm away in accordance with Requirements 5.2.2.1.1 and 5.2.2.2.2 of the NBS Handbook for Radiation Safety for X-Ray Diffraction and Fluorescence Analysis Equipment.

Brass Collimator with
Aluminum Insert
2 mm Diameter Hole

Screw-On
Nickel Plated
Brass Cover

Brass
Safety
Plug

Dimensions in mils/mm

.020/
0.51
.260/   .219/
6.6   5.6
.250/
6.4
.464/
11.8
.443/11.3

Collimator cover mechanical dimensions (mils/mm).
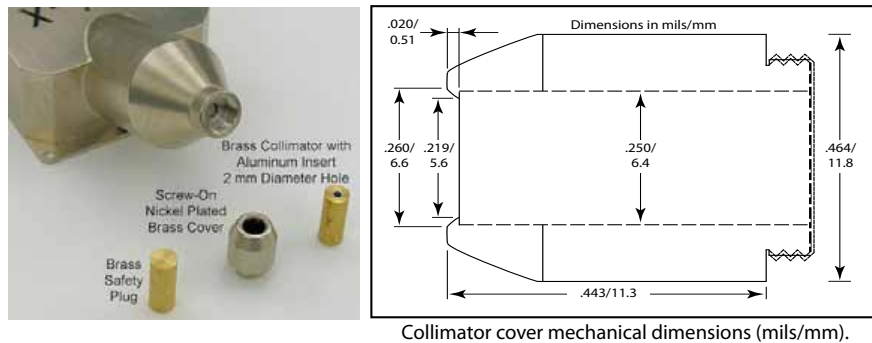
Filters

There are many reasons to use filters on the x-ray tube. They can help eliminate low energy photons to create a clean background and they can filter the characteristic lines of the tube's target. Keep in mind that when any filter is used it reduces the flux coming out of the tube. An Al filter reduces the flux much less than a Mo or Ag filter. The higher the Z of the filter or the thicker the filter, the less flux will be available. It is therefore necessary to raise the current of the x-ray tube to compensate.

Please see http://www.amptek.com/minix.html for output spectra with various filters.

Filters Provided		
Material	Thickness (µm/mils)	# Provided
Al	1016 / 40	5
Al	254 / 10	5
Cu	25.4 / 1	3
Mo	25.4 / 1	2
Ag	25.4 / 1	1
W	25.4 / 1	1

The Mini–X shown with the Amptek XR-100CR X-Ray Detector and PX5 Digital Pulse Processor.

The Mini–X mounted on MP1 with X-123SDD.

The Mini–X (previous version) shown and XR-100CR with vacuum couplings.

OEM X-Ray Tubes for XRF

The OEM X-ray tubes are not the same as the Mini-X.

The Mini-X has a USB interface to control the voltage and current through PC software. The Mini-X is an end-user, packaged device.

The OEM versions are controlled by user supplied analog voltages.

Radiation Precautions

The Mini–X Is intended to generate x-ray radiation during normal operation. The Mini–X has been designed to focus radiation in the designated output direction, however radiation in other directions is possible and should be addressed with shielding and/or monitoring in the final application.

Radiation Levels external to the X-ray tube housing with the brass safety plug ON do not exceed 25 µS/h (2.5 mrem/h) measured 5 cm from the surface of the housing in accordance with Requirements 5.2.2.1.1 and 5.2.2.2.2 of the National Bureau of Standards (NBS) Handbook for Radiation Safety for X-Ray Diffraction and Fluorescence Analysis Equipment.

Examples of Shielding (that comply with the above standard)

    1 mm (0.040 inch) of Pb will result in radiation levels of 0.5 mrem/h.

    6.35 mm (0.250 inch) of Fe will result in radiation levels of 0.5 mrem/h.

    3.18 mm (0.125 inch) of Brass will result in radiation levels of 2.5 mrem/h.

The inside of the housing can also be lined with 3.18 mm (0.125 inch) of aluminum (Al) in order to absorb the XRF from the shielding material.

Caution

The Mini-X is only one component of an X-ray instrument. It is the responsibility of the user, the OEM customer, or experimenter to provide a fail safe metal enclosure to prevent escaping radiation while using this product. The final product (turn-key system) must comply with local government regulations to protect personnel from exposure to radiation. Amptek Inc., bears no responsibility for the incorrect use of this product.

Caution

This device produces X-Rays when energized. To be operated only by qualified personnel.
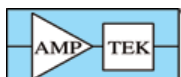
Bibliography

[1] AMPTEK INC. Mini-X, Miniature X- Ray Source. `www.amptek.com`.

[2] KETEK. AXAS-D, Analytical X-ray Acquisition System. `www.ketek.net`.

[3] W.C. Röntgen. *Eine neue Art von Strahlen*. Number Bd. 1 in Collection Léo Pariseau. Stahel, 1896.

[4] Nobel Media AB 2014 Nobelprize.org. The nobel prize in physics 1901. `http://www.nobelprize.org/nobel_prizes/physics/laureates/1901/`, Nov 2015.

[5] Nobel Media AB 2014 Nobelprize.org. The nobel prize in physics 1903. `http://www.nobelprize.org/nobel_prizes/physics/laureates/1903/`, Nov 2015.

[6] W. D. Coolidge. A powerful röntgen ray tube with a pure electron discharge. *Physical Review*, 2(6):409–430, Dec 1913.

[7] H.G.J. Moseley. Lxxx. the high-frequency spectra of the elements. part ii. *Philosophical Magazine Series 6*, 27(160):703–713, Apr 1914.

[8] Nobel Media AB 2014 Nobelprize.org. The nobel prize in physics 1914. `http://www.nobelprize.org/nobel_prizes/physics/laureates/1914/`, Nov 2015.

[9] Nobel Media AB 2014 Nobelprize.org. The nobel prize in physics 1915. `http://www.nobelprize.org/nobel_prizes/physics/laureates/1915/`, Nov 2015.

[10] Nobel Media AB 2014 Nobelprize.org. The nobel prize in physics 1917. `http://www.nobelprize.org/nobel_prizes/physics/laureates/1917/`, Nov 2015.

[11] Nobel Media AB 2014 Nobelprize.org. The nobel prize in physics 1922. `http://www.nobelprize.org/nobel_prizes/physics/laureates/1922/`, Nov 2015.

[12] N. BOHR. Atomic structure. *Nature*, 107(2682):104–107, Mar 1921.

[13] Nobel Media AB 2014 Nobelprize.org. The nobel prize in physics 1924. `http://www.nobelprize.org/nobel_prizes/physics/laureates/1924/`, Nov 2015.

[14] B. Beckhoff, B. Kanngießer, N. Langhoff, R. Wedell, and H. Wolff. *Handbook of practical X-ray fluorescence analysis*. Springer, Berlin ; New York, 2006.

[15] R. van Grieken and Andrzej Markowicz, editors. *Handbook of X-ray spectrometry*. Number v. 29 in Practical spectroscopy. Marcel Dekker, New York, 2nd ed., rev. and expanded edition, 2002.

[16] J. Als-Nielsen and Des McMorrow. *Elements of modern X-ray physics*. Wiley, Hoboken, 2nd ed edition, 2011.

[17] Wikipedia. `https://commons.wikimedia.org/wiki/File:X-ray_range.svg`.

[18] F. L. Hunt W. Duane. On x-ray wave-lengths. *Physical Review*, 6(2):166–172, Aug 1915.

[19] W. BOTHE, P. EWALD, F. KIRCHNER, H. KULENKAMPFF, and STEINKE E. G., editors. *Röntgenstrahlung Ausschliesslich Röntgenoptik*. Springer Science + Business Media, 1933.

[20] R. Jenkins, R. Manne, R. Robin, and C. Senemaud. IUPAC nomenclature system for x-ray spectroscopy. *X-Ray Spectrom.*, 20(3):149–155, Jun 1991.

[21] Dennis J Kalnicky and Raj Singhvi. Field portable XRF analysis of environmental samples. *Journal of Hazardous Materials*, 83(1-2):93–122, May 2001.

[22] Pierre Auger. Sur l'effet photoélectrique composé. *J. Phys. Radium*, 6(6):205–208, 1925.

[23] Thomas Langer. *Untersuchung ultradünner Schichten mit AUGER Spektroskopie*. PhD thesis, Universität Osnabrück, 2008.

[24] Wolfgang Demtröder and Wolfgang Demtröder. *Atoms, molecules and photons: an introduction to atomic-, molecular- and quantum-physics*. Number Wolfgang Demtröder ; Bd. 3 in Experimentalphysik. Springer, Berlin, 4., überarb. aufl edition, 2010.

[25] K. H. Lieser. G. zschornack: Atomdaten für die röntgenspektralanalyse. *Berichte der Bunsengesellschaft für physikalische Chemie*, 94(9):1048–1048, Sep 1990.

[26] D. Iwanenko and I. Pomeranchuk. On the maximal energy attainable in a betatron. *Physical Review*, 65(11-12):343–343, Jun 1944.

[27] European Synchrotron Radiation Facility. `http://www.esrf.eu/`.

[28] A. Einstein. über einen die erzeugung und verwandlung des lichtes betreffenden heuristischen gesichtspunkt. *Annalen der Physik*, 322(6):132–148, 1905.

[29] Glenn F. Knoll. *Radiation detection and measurement.* Wiley, New York, 3rd ed edition, 2000.

[30] Pavel Rehak, Emilio Gatti, Antonio Longoni, J. Kemmer, Peter Holl, Robert Klanner, Gerhard Lutz, and Andrew Wylie. Semiconductor drift chambers for position and energy measurements. *Nuclear Instruments and Methods in Physics Research Section A: Accelerators, Spectrometers, Detectors and Associated Equipment*, 235(2):224–234, Apr 1985.

[31] P. Lechner, C. Fiorini, R. Hartmann, J. Kemmer, N. Krause, P. Leutenegger, A. Longoni, Soltau, and et al. Silicon drift detectors for high count rate x-ray spectroscopy at room temperature. *Nuclear Instruments and Methods in Physics Research Section A: Accelerators, Spectrometers, Detectors and Associated Equipment*, 458(1-2):281–287, Feb 2001.

[32] P. Wobrauschek. Methods of quantitative x-ray fluorescence analysis. Vorlesungsskriptum.

[33] J Sherman. The correlation between fluorescent x-ray intensity and chemical composition. *ASTM Special Publication*, 157:27, 1954.

[34] Jacob Sherman. The theoretical derivation of fluorescent x-ray intensities from mixtures. *Spectrochimica Acta*, 7:283–306, Jan 1955.

[35] Toshio Shiraiwa and Nobukatsu Fujino. Theoretical calculation of fluorescent x-ray intensities in fluorescent x-ray spectrochemical analysis. *Japanese Journal of Applied Physics*, 5(10):886–899, Oct 1966.

[36] Geneva International Organization for Standardization (ISO). Iso guide 30:2015, reference materials – selected terms and definitions. `www.iso.org/iso/home/store/catalogue_ics/catalogue_detail_ics.htm?csnumber=46209`, 2015.

[37] J. W. Criss and L. S. Birks. Calculation methods for fluorescent x-ray spectrometry. empirical coefficients versus fundamental parameters. *Anal. Chem.*, 40(7):1080–1086, Jun 1968.

[38] Peter Allinger. Construction and development of a Marko-XRF facility. Technical report, TU Wien, 2014.

[39] Dassault Systems. 3D CAD design software SolidWorks. `www.solidworks.com`.

[40] Spex SamplePrep. Kapton window film. `http://www.spexsampleprep.com/equipment-and-accessories/accessory_product.aspx?partnumber=3511`.

[41] Alexander Utz. Zweidimensionale Röntgenfluoreszenzanalyse zur Darstellung biologischer Proben in stark streuender Matrix. Master's thesis, TU Wien, 2012.

[42] ARDUINO. MICRO. `www.arduino.cc/en/Main/ArduinoBoardMicro`.

[43] XRF Group, IAEA laboratories Seibersdorf. Quantitative X-ray Analysis System. `www.iaea.org/OurWork/ST/NA/NAAL/pci/ins/xrf/pciXRFdown.php`.

[44] WaveMetrics. Igor pro, scientific graphing, data analysis, curve fitting & image processing software. http://www.wavemetrics.com/index.html.

[45] USAF. Usaf 1951 3-bar resolving power test chart, from mil-std-150a, section 5.1.1.7, resolving power target. `www.efg2.com/Lab/ImageProcessing/TestTargets/{#}USAF1951`.

[46] MathWorks. MATLAB. `http://de.mathworks.com/products/matlab/`.

[47] Breitenfeld Edelstahl AG. steel plant. `http://www.breitenfeld.at/`.

USER MANUAL Makro-XRF
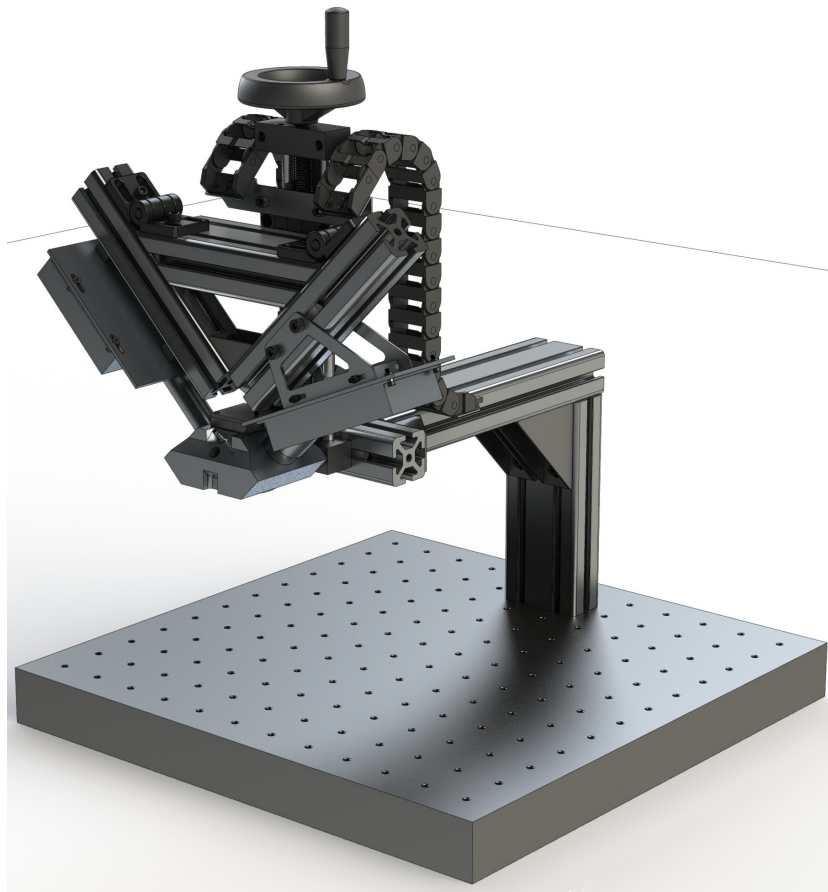
Ing. Allinger Peter, BSc

December 4, 2015   version: 1.1

Contents

Chapter 1

Getting started

There are several important tasks to perform before any kind of measurement can be made. This chapter will describe these tasks as short and concise as possible. It starts with a checklist followed by a short explanation of each item.

1.1 Checklist

- Windows: Start X-Spect (main program)

- Windows: Are all USB-ports connected to the virtual machine?

- External: Is the KETEK [1] power-supply turned on?

- Program: Start the WEBCAM

- Program: Connect MCA (usually COM8)

- Program: Start ARDUINO [2] light-controls

- Program: Set current position as new zero?

1.2 USB-ports

Unfortunately some of the software requires Windows XP to run, therefore a Virtual Machine (VM) is used to emulate the operating system. On the top of the screen you should see a small bar, which tells you that you are running the VM and provides a function called USB. If you click on the USB menu, you should see something like this:
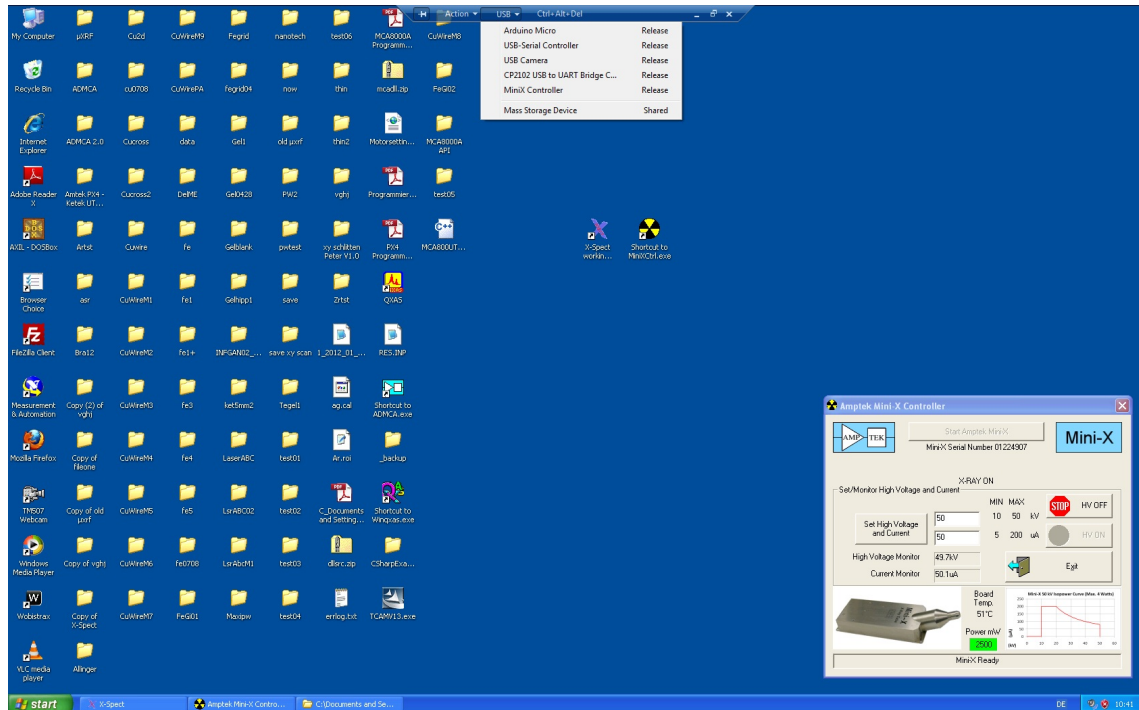
Figure 1.1: Virtual Machine - USB connections

Make sure everything is attached! (If attached, you should see a **RELEASE** next to the item). You need at least the motor controls and the detector (MCA). Other parts like the Mini-X [3] x-ray tube, the Webcam or the Arduino [2] light-controls are optional.

Here is a list of the hardware names that should be enumerated in the USB menu:

- Motor controls: CP2102 USB to UART Bridge C...

- KETEK detector (MCA): USB-Serial Controller

- Mini-X x-ray tube: MiniX Controller

- Thrustmaster Webcam: USB Camera

- Arduino light-control: Arduino Micro

1.3 KETEK power supply

There is an external power supply for the peltier cooling of the KETEK SDD (**S**ilicon **D**rift **D**etector) [1]. Make sure it is turned on in the correct order depicted below!
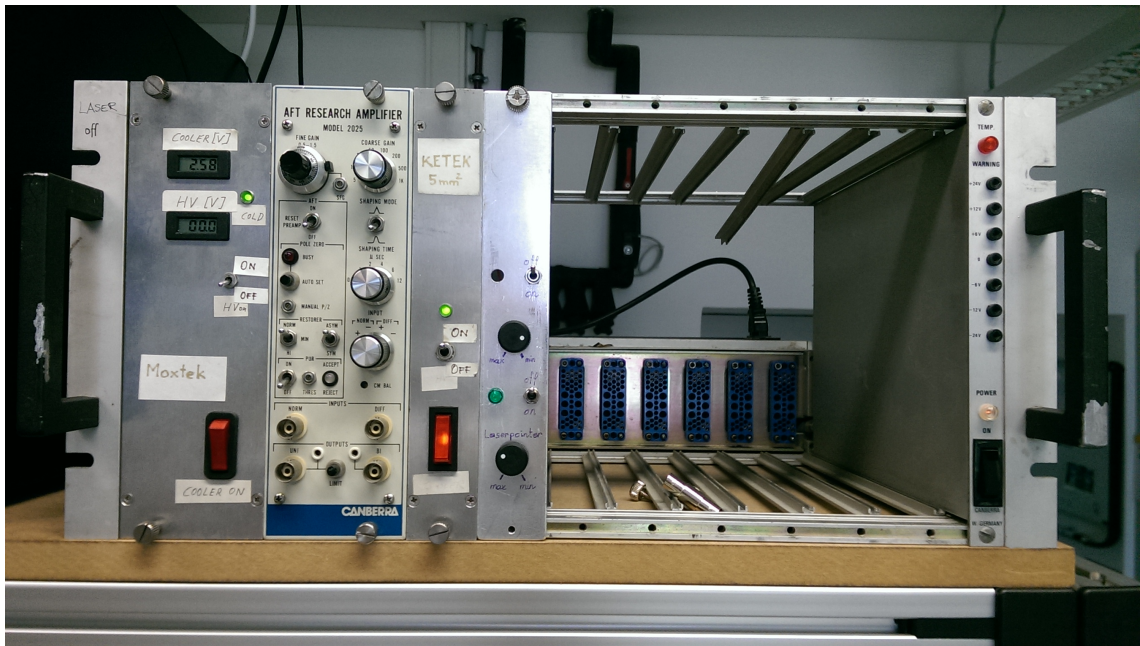
Figure 1.2: KETEK power supply

1.4 WEBCAM

Due to some issues with the VM (**V**irtual **M**achine), the webcam driver sometimes fails and needs to be reinstalled. There is a file called TCAMV13.exe on the desktop. Simply double click it and follow the instructions. When the installer asks you to plug in the webcam, it is sufficient to detach it in the USB menu on the top corner of the VM and re-attach it. Please ignore all notifications of the windows hardware manager.

If the webcam driver is working properly it needs to be started in the X-Spect program by selecting WEBCAM from the menu and by clicking on the button START. The webcam feed should be displayed immediately in the button left corner of the program.

1.5 Connecting the MCA

If the MCA is attached in the USB-port menu of the VM, simply select MCA from the X-Spect program menu and click CONNECT. A pop-up window should open, requesting the COM-port of the detector. The standard setting is COM8, but this may change and you can verify the current port in the hardware manager (picture 1.3): Press START → CONTROL PANEL → SYSTEM → HARDWARE (register) → DEVICE MANAGER → PORTS (COM & LPT).

After pressing OK it will take some time before it is connected. If an error occurs, a notification window will pop-up and you should check if the USB-port is attached and the COM settings are correct.
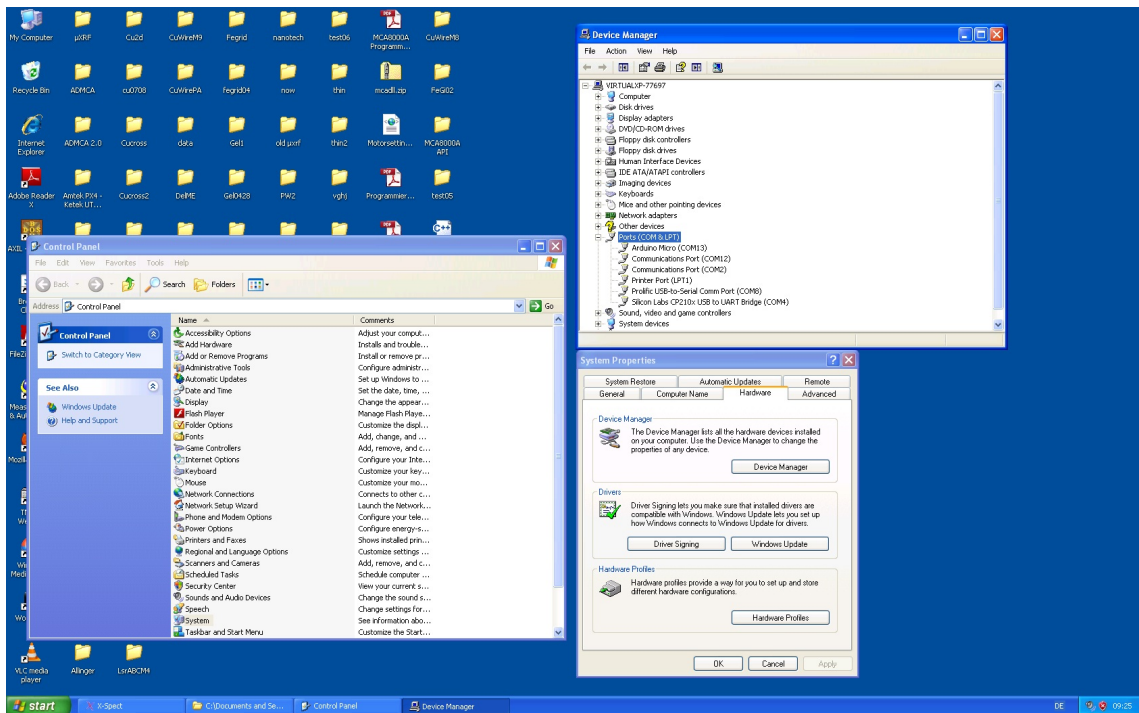
Figure 1.3: Windows system manager, ports display

1.6 Arduino light-controls

Verify if the USB-port of the arduino [2] is attached to the VM and press the START ARDUINO button in the program. The program should determine the correct COM port and start the light and the laser pointers at 45% and 20% power respectively. You can adjust the brightness by moving the corresponding sliders (picture 1.4).

Figure 1.4: Arduino light controls

1.7 Setting the zero position

Usually the XY-table is not in the absolute zero position (origin), but rather in the last position of a previous measurement. It still might be convenient to start at this unknown position, especially if you´d like to repeat some measurements with different settings or pick up at a position set before. The button SET NEW ZERO will read the current motor position and set it as local zero. Every motor value or measurement will now treat the current position as the new origin. If you need to reset it, simply press RESET ZERO POSITION!
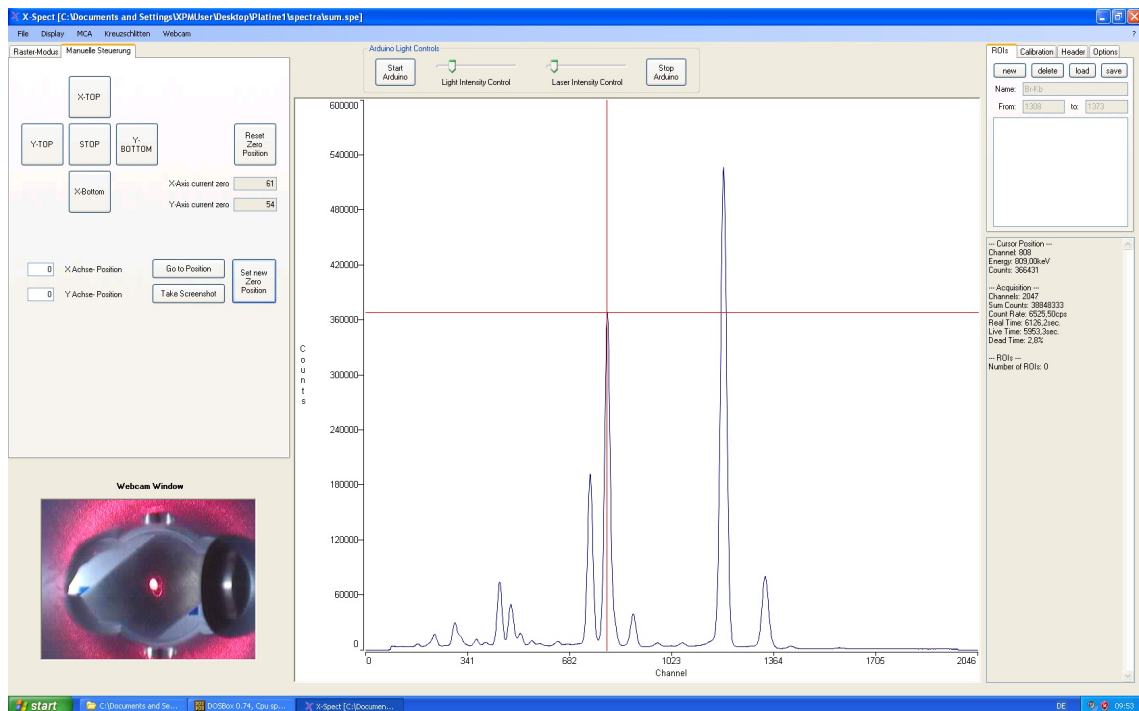
Figure 1.5: Manual motor controls

Chapter 2

AMPTEK Mini-X Controller
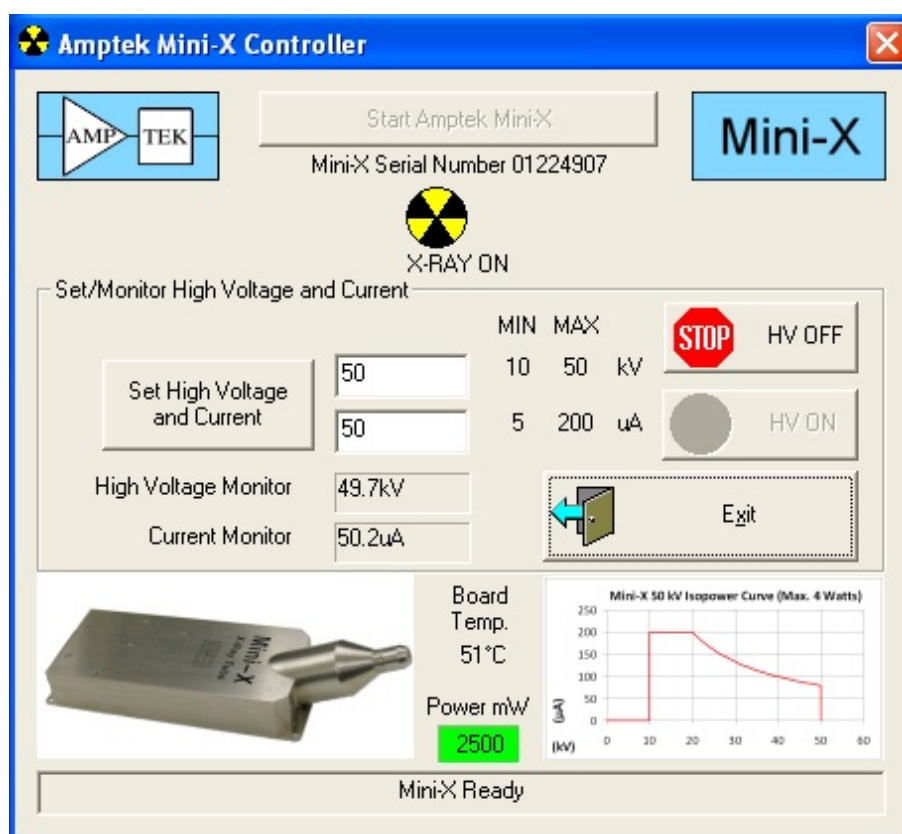
Figure 2.1: AMPTEK Mini-X control program [3]

The x-ray tube AMPTEK Mini-X [3] is operated with a separate software. There should be a link on the desktop called MiniXCtrl.exe. When you start the program, a small window (see picture 2.1) should open.

Make sure the Mini-X is attached to the VM (see chapter 1.2) and start it with the button START AMPTEK MINI-X. The program is fairly easy and self-explanatory.

In order to switch on the HV (**H**igh **V**oltage), one first has to set the desired voltage and current. They are in units of kV and μA respectively. Be sure not to exceed 4 W ($P = U \cdot I$). A small diagram visible on the lower right part of the control window depicts the characteristic voltage curve over the corresponding current value.

Once satisfied with the settings you can start the HV with the **HV ON** button. A beeping sound and a red blinking LED on the backside of the x-ray tube will indicate that the HV is on and x-rays emitted.

To change or stop the HV, press the **HV OFF** button and enter the new values or close the program with the **EXIT** button.
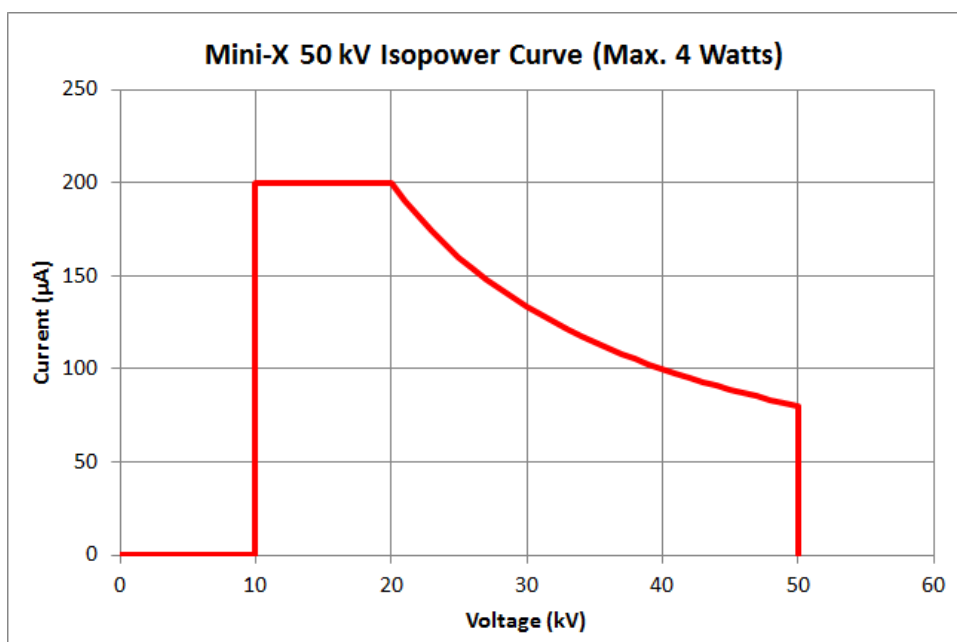
Figure 2.2: AMPTEK Mini-X isopower curve [3]

Chapter 3

Single spot measurement

3.1 Positioning

In the **MANUELLE STEUERUNG** register on the left side of the screen, several buttons are available for positioning and scan area selection. A set of directional movement control buttons (**X-TOP, X-BOTTOM, Y-TOP, Y-BOTTOM**) in a cross formation allows the user to move step by step in either direction by clicking on them. The **STOP** button in the middle is used to cancel all movements immediately. With the **RESET ZERO POSITION** control the user can reset all position settings and the X-Y table will move to it´s absolute zero position. This step is usually performed after some reference zero position has been set with the **SET NEW ZERO POSITION** button below. The actual zero position used for all movements performed by the program itself in case of an automated grid measurement or the user is displayed between these two buttons. For quick positioning and scan area evaluation, the **GO TO POSITION** button can be used, by entering the desired x and y coordinates in the field to the left and then confirming them with the button itself. Finally a **TAKE SCREENSHOT** button allows the user to manually take a screenshot of the current position.
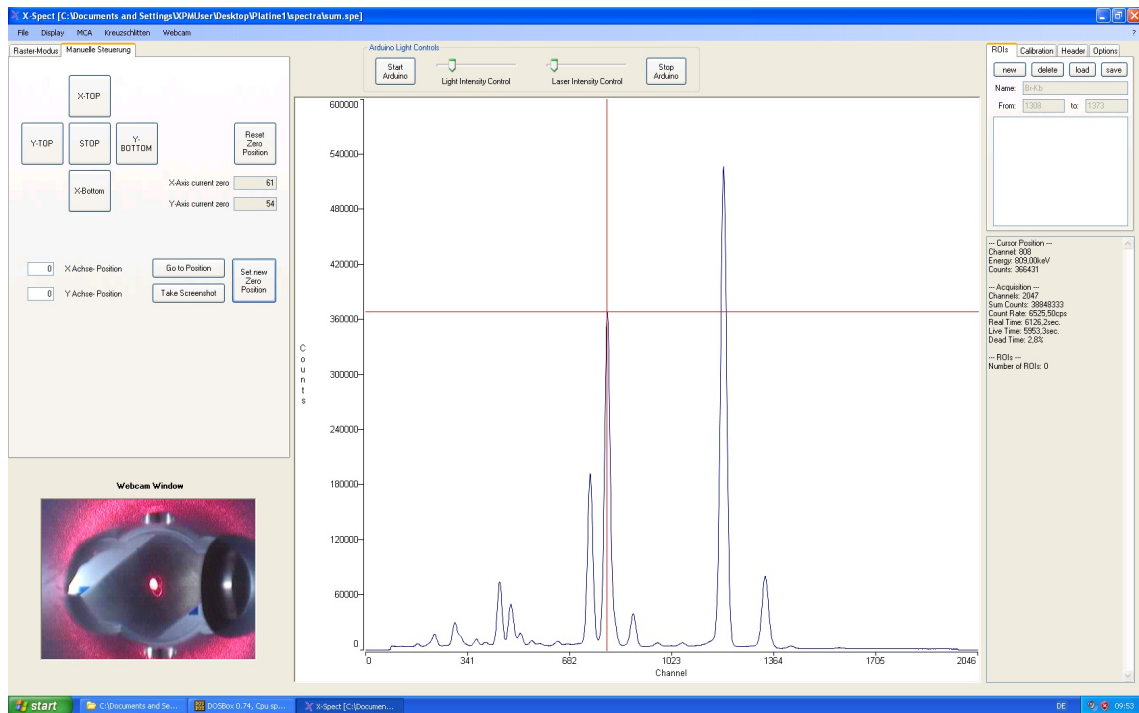
Figure 3.1: X-Y table movement controls, located in the **MANUELLE STEUERUNG** register on the left side of the interface

3.2 Acquisition

The **ACQUIRE** register is used to manually start or stop the acquisition of a single spectrum at the current spot, to clear the display and to save a single spectrum. Furthermore it is possible to define the acquisition time, by entering the desired value and confirm it with the **SET** button.

The program is also able to distinguish between realtime (the total time the detector is actually counting) and livetime (time from pressing start until completion, including program-, computing- and other dead-times). Remember to confirm your settings with the **SET** button. For user information, a progress bar and a status information window is also included on the right hand side (picture 3.2).
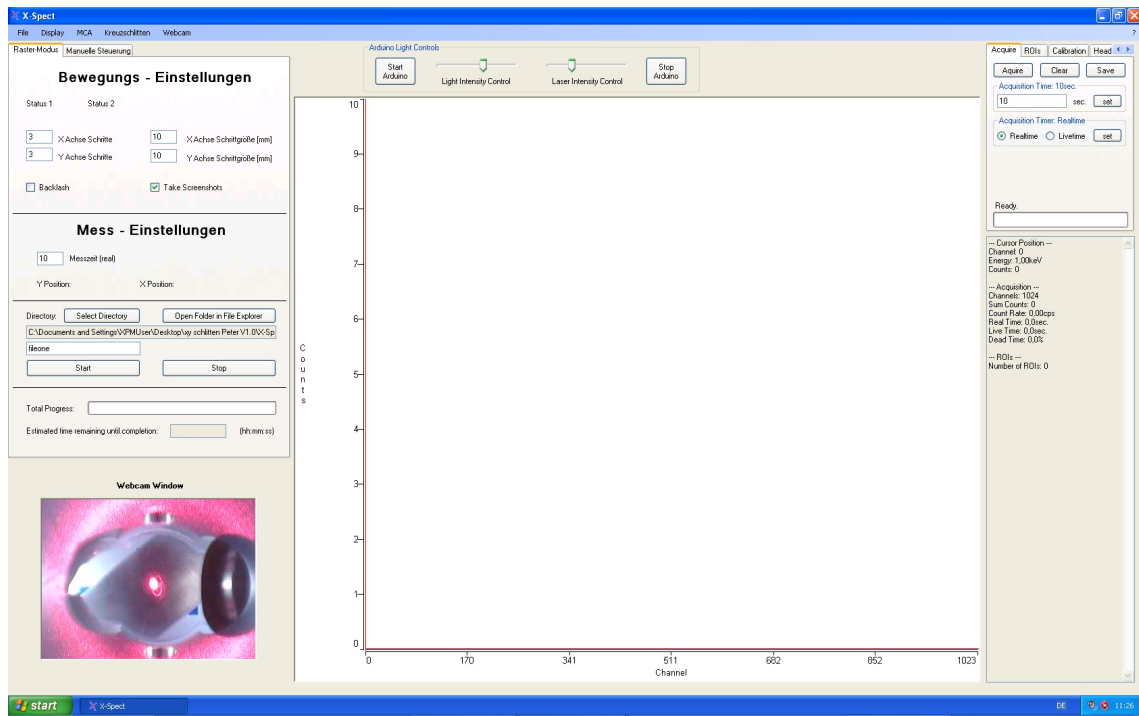
Figure 3.2: Acquire window with 10sec. acquisition time set and realtime selected. The info text **ready** above the empty progress bar signalizes, that no measurement is running and the user may start a new one anytime.

3.3 ROIs

On the next register called **ROIs**, the user can define start and points for peak evaluation. In order to do this, a new ROI has to be generated first, by clicking on the button called **NEW**. In the box the below a new 'unnamed' ROI has been generated. To modify it, select it with the left mouse button. Now you can rename it and either manually define the min and max energy channel or simply **CTRL+Leftclick** to set the preferred starting point in the spectrum window and **ALT+Leftclick** to set the end-point. An new textblock containing all information like net channel, gross and net counts, background, etc. about the ROI should now be visible in the info-display on the right side of the screen.
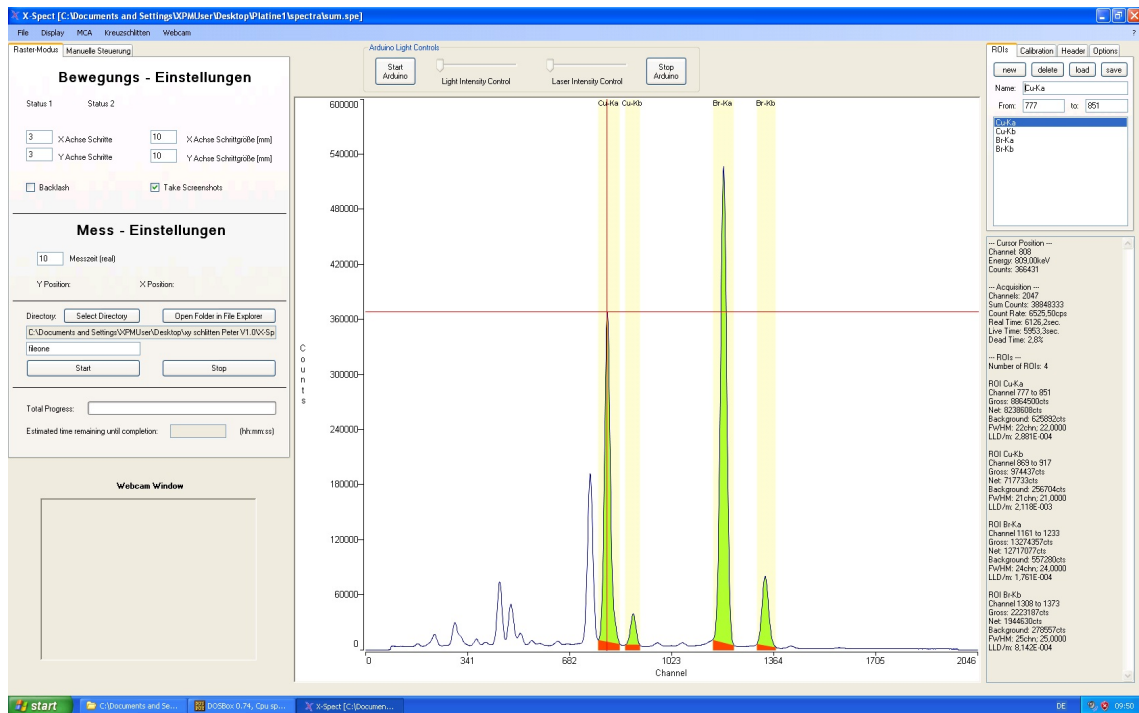
Figure 3.3: ROIs register depicting an example spectrum with several ROI´s set and the corresponding information on the right

3.4 Calibration

It is possible to perform an energy calibration by assigning a specific channel number to the corresponding line energy. In order to do this, left-click in the spectrum window and select a peak, where you are absolutely sure about the corresponding element. A red line will appear and you can read off the channel number and the energy on the right side of the screen in the info window. Memorize the channel number and add a new calibration point with the **ADD** button. Select it in the list below, enter the channel number and the corresponding line energy. Repeat this procedure with at least another peak for standard calibration.

If you are not satisfied or do not need some calibration points, simply select the corresponding one and delete it with the **REMOVE** button. It is also possible to

save or load a calibration with the remaining two buttons. Make sure to check a loaded calibration for its validity.
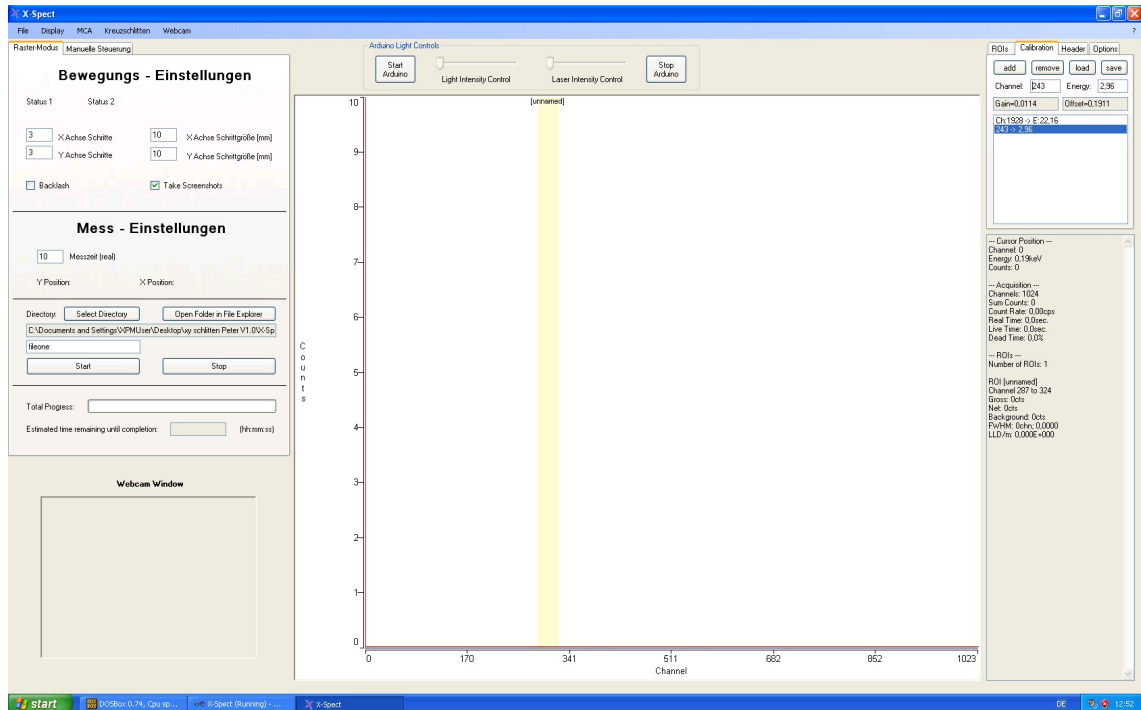
Figure 3.4: Calibration

3.5 Header

The **HEADER** menu is used to add custom information to the spectrum files generated with each measurement. It is fairly simple: Click **ADD** to add a new textline and **REMOVE** to delete it. Once a new textline is added, select it with the left mouse button and enter the desired text below. Optionally you can add a timestamp with the field below.
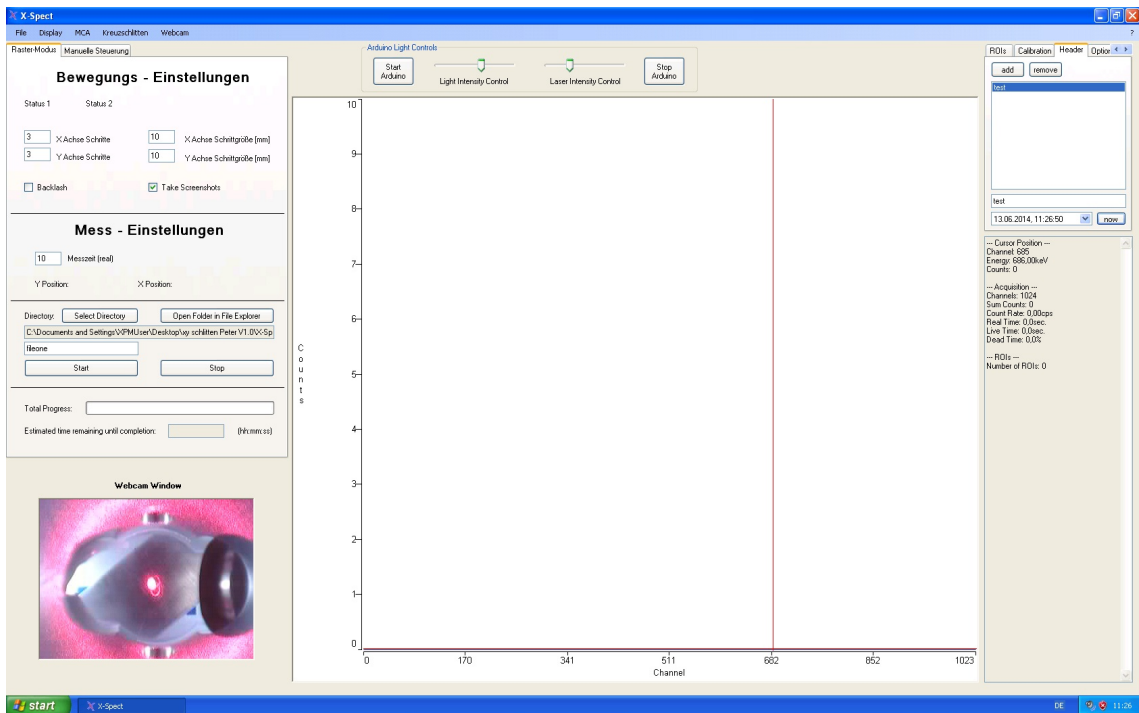
Figure 3.5: Header

3.6 Options

The last register **OPTIONS** is used to alter settings, like file format, file names, secondary save formats for AXIL evaluation (.spe) and the option to save the sum spectrum, which is usually a good idea. All standard values have been set for immediate measurements and should not be changed unless absolutely necessary.
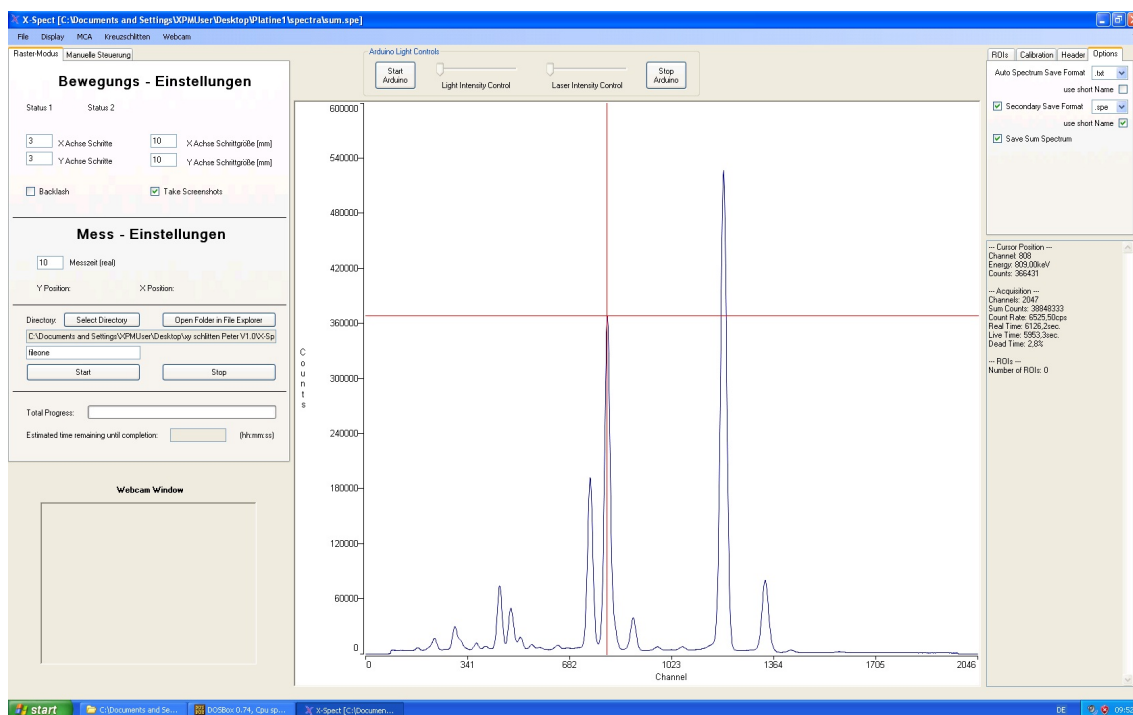
Figure 3.6: Options

Chapter 4

Automated measurement

4.1 Preparations

The basics, like positioning, acquiring a sample spectrum, etc. have already been explained in the previous chapters. Feel free to re-read them if you seem to miss something.

In order to perform an automated measurement of a sample, you have to define the boundaries of the region you would like to scan. For this purpose switch to **'Manuelle Steuerung'**, set your starting position and figure out the X- and Y-values. Make sure to define a slightly bigger region to avoid unwanted cutoffs! Do not hesitate to turn, move or otherwise reposition the sample on the X-Y table by hand as convenient. It is highly recommended to manually move along the boundaries to make sure everything is correct before starting. This will only take a minute and might save you from repeating a long term measurement.

4.2 Movement-settings

Once the preparations are complete, switch back to the register **'Raster-Modus'** and carefully check all settings. The first line displays the status text of both spindle

motors and should read 'OK'. Now fill in the X and Y limits, but be careful to add one step since the zero position will be counted as well and enter the corresponding step size in mm. There are two check boxes below: 'Backlash' and 'Take Screenshots'. A backlash might occur when a spindle changes its moving direction, due to the play of the spindle thread. This option turns the spindle a few degrees every time direction is changed to prevent misalignments. Its standard setting is off, since it rarely makes a noticeable difference. The other box 'Take Screenshots' is checked as default, so the program will take a screenshot at every measurement position.
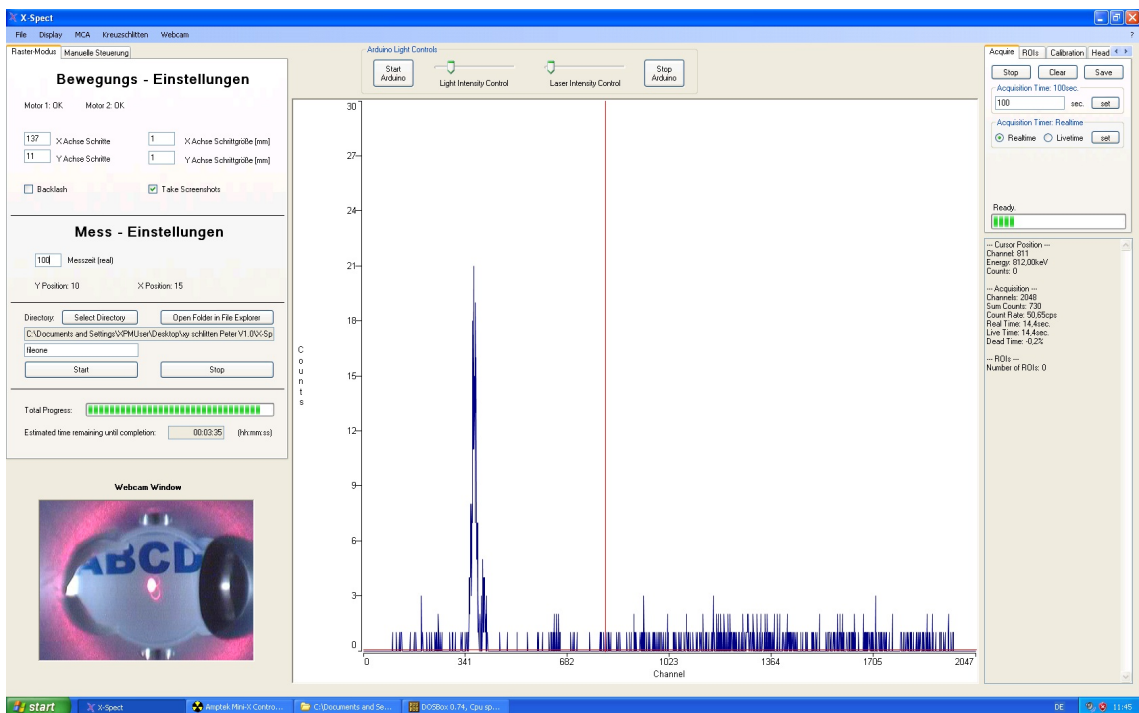
Figure 4.1: Automated grid measurement

4.3 Measurement-settings

The next section called 'Mess-Einstellungen' will let you enter the measuring time at each position in seconds and displays info text about the current X- and Y-position. Below the horizontal line the user may change the directory, where all data will

be stored by pressing the **Select Directory** button and open a windows explorer window containing the current directory with the button **Open Folder in File Explorer** next to it. This function is useful for renaming the sample folder after a measurement is complete and quickly copying it to the Desktop for AXIL-evaluation (see chapter 5). Below these buttons is a textbox with the current path and a field with the standard sample name 'fileone', which the user can rename to an 8 character custom name (8 because of the DOS limitations for AXIL evaluation).

Finally, if you are sure all settings are correct, the measurements can be started with the **START** button, or aborted with the **STOP** button. The last field contains status information, like a progress bar and the estimated time remaining until completion, which will be calculated after the first measurement.
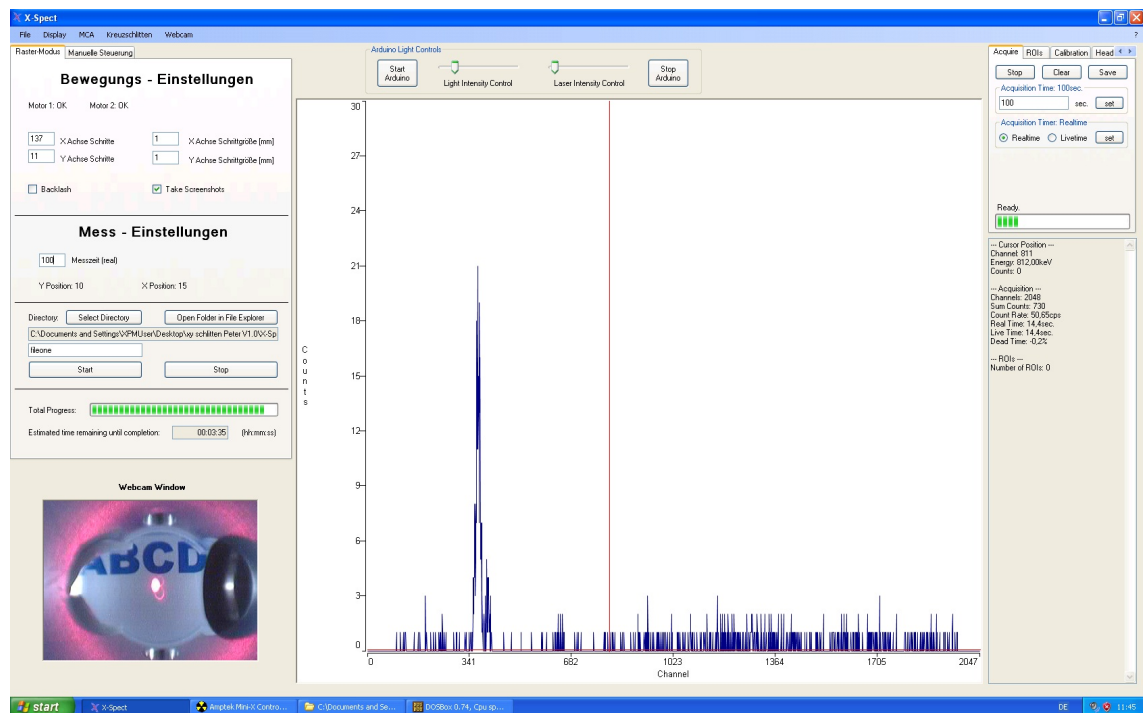
Figure 4.2: Automated grid measurement

Chapter 5

Spectrum evaluation - AXIL

For convenience, the data folder of your sample you wish to analyze should be copied to the desktop. This is easily done by clicking on the button OPEN FOLDER IN FILE EXPLORER → right click on the folder → select **COPY** → and finally right click on the desktop → **PASTE**.

The program AXIL is used for spectrum fitting and batch processing of multiple spectrum data files. Unfortunately it only works in DOS. On the desktop should be a link called AXIL - DOSBox, double clicking it will start a new window that looks like this:
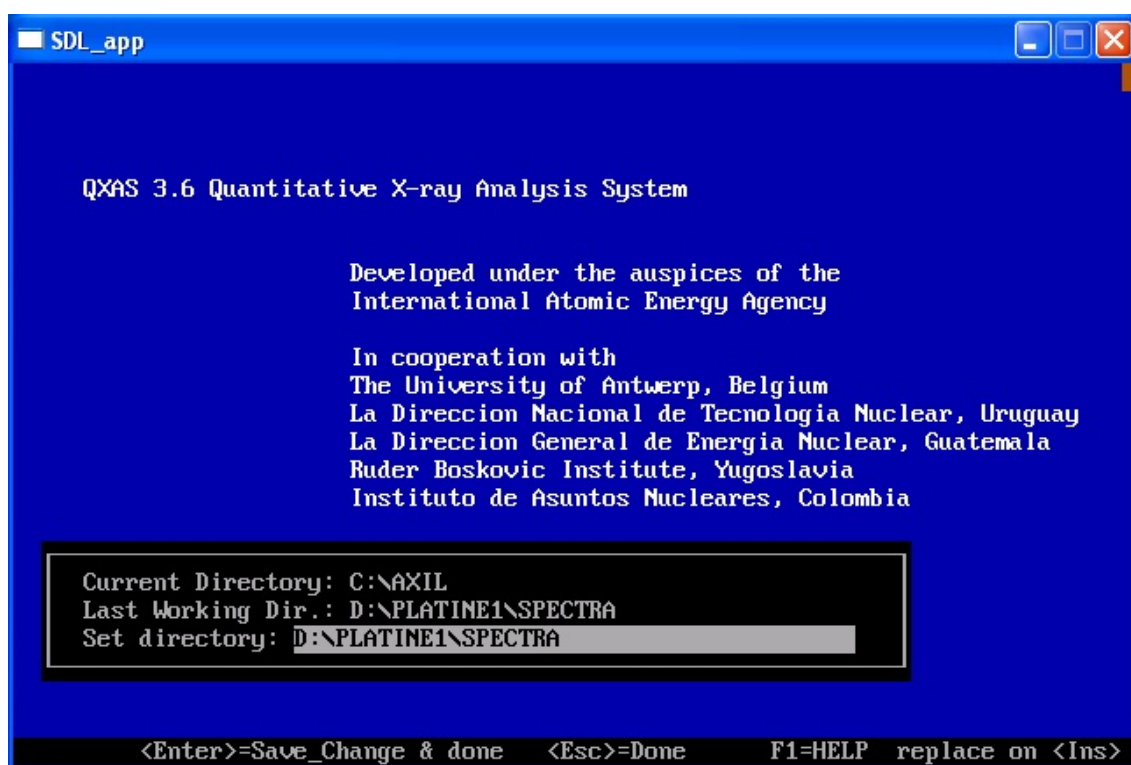
Figure 5.1: AXIL - selecting the working directory

It is usually a good idea to analyze the sum spectrum of a measurement first and generate a model for batch processing, since every element found in different spots will be contained. To do so simply type in the path of the sample **D:\SampleName\spectra\spe**. Next select spectrum fitting and then AXIL (& Voigt peak profiles option for high energy K-lines). In the next menu ther are three options available: **analyse spectra**, **select model** and **save model**. If you click on analyse spectra, a black screen will appear and you can load the sum spectrum by entering **L D** and **ENTER**.
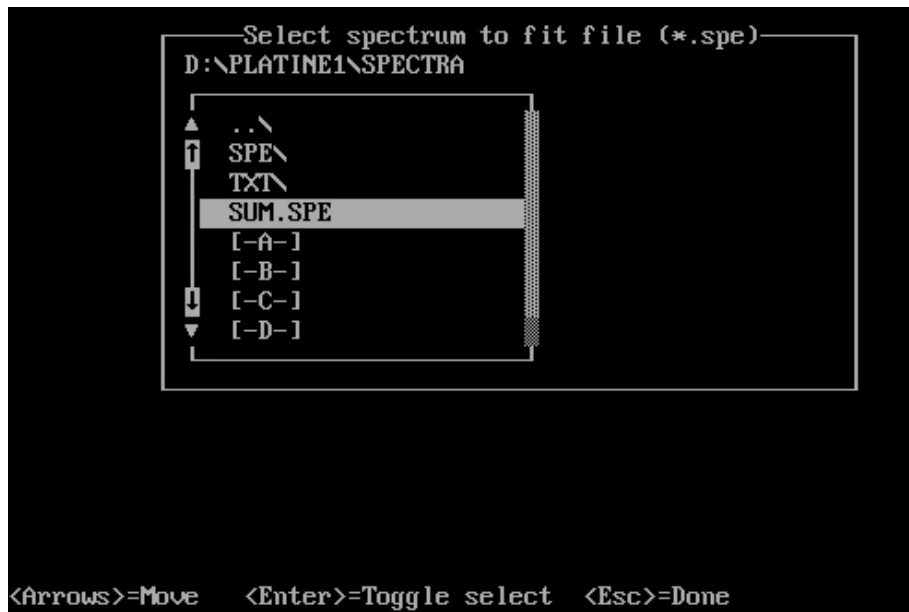
Figure 5.2: AXIL - file browser dialog

This will open a folder menu, where you can select the sum.spe file (you can go one folder up with **..**) for the sum spectrum, or any other .spe file. A spectrum should now be visible and your next step will be to analyse it.
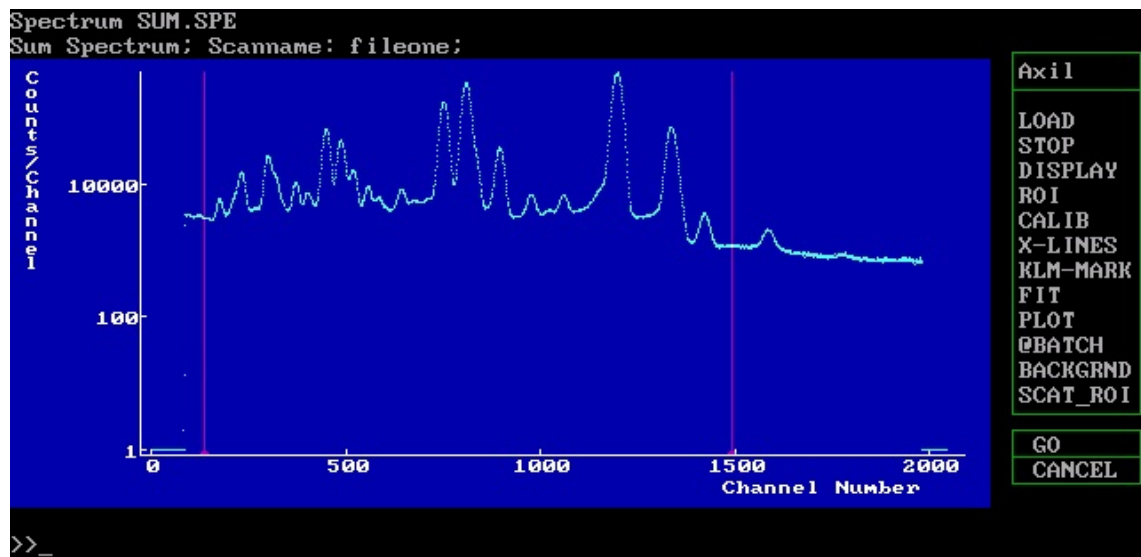
Figure 5.3: AXIL - sum spectrum loaded

For this reason you have several tools available, all of them are listed on the right side of the program screen. *Hint: It is usually sufficient to type only the starting letter(s) of a function, depending on the uniqueness, followed by a space.* A detailed description and manual of every command is available online [4], but for most cases only some functions are necessary and listed below.

Important AXIL commands:

1. ROI - define a region of interest

2. DISPLAY - zooming and lin/log options

3. CALIB - for energy calibration

4. KLM-MARK - helpful tool that displays element specific K,L,M lines

5. X-LINES - define which elements you wish to evaluate

6. BACKGRND - for background settings

7. FIT - to evaluate the spectrum

8. Save model - the only one not in this command list

9. @BATCH - for batch processing

5.1 ROI

It is recommended to set a ROI (**R**egion **of I**nterest) first. To do so type **R** and press **SPACE**. The display changes and there are new commands available and listed on the right side of the screen.
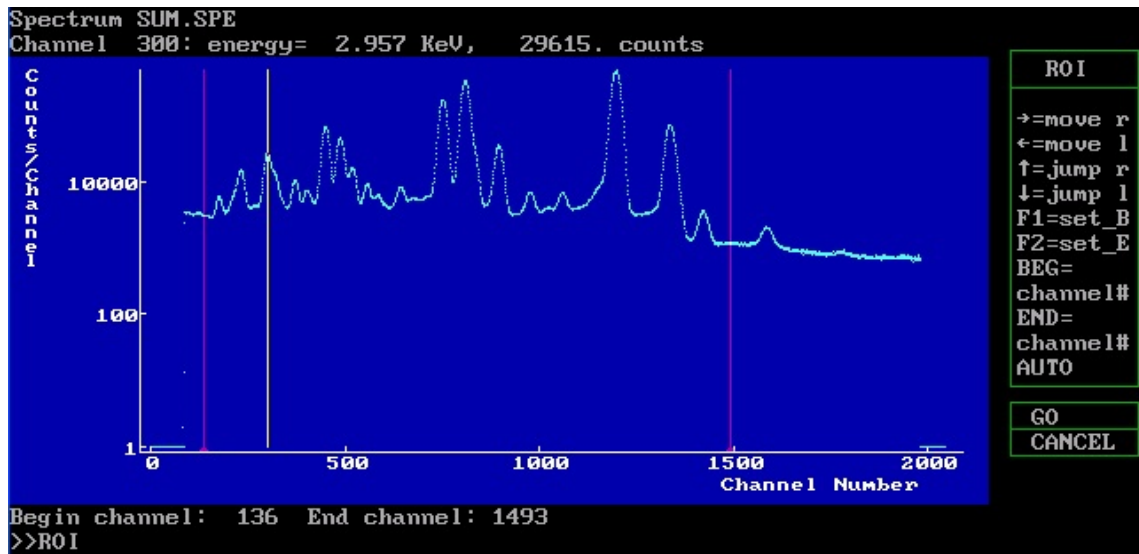
Figure 5.4: AXIL - defining a range of interest (ROI)

With the **ARROW** keys navigate to a point you´d like to define as start, press **F1** and hit **ENTER**. *Hint: jump between major peaks with the **UP** and **DOWN** arrow keys and fine tune it with the **RIGHT** and **LEFT** keys!* Repeat the procedure to define your end point, but this time press **F2** and **ENTER**. If you forget to press **ENTER** no ROI will be set and you have to do it again.

5.2 DISPLAY

If you have defined a ROI you can zoom in your x-axis by **D ROI ENTER**. Furthermore you can define a MIN and/or MAX value for your y-axis. This is useful if you have a very high background or are not interested in the high peaks and rather looking for smaller ones. In case you are not satisfied or want to zoom out, press **D SPECTR ENTER**.
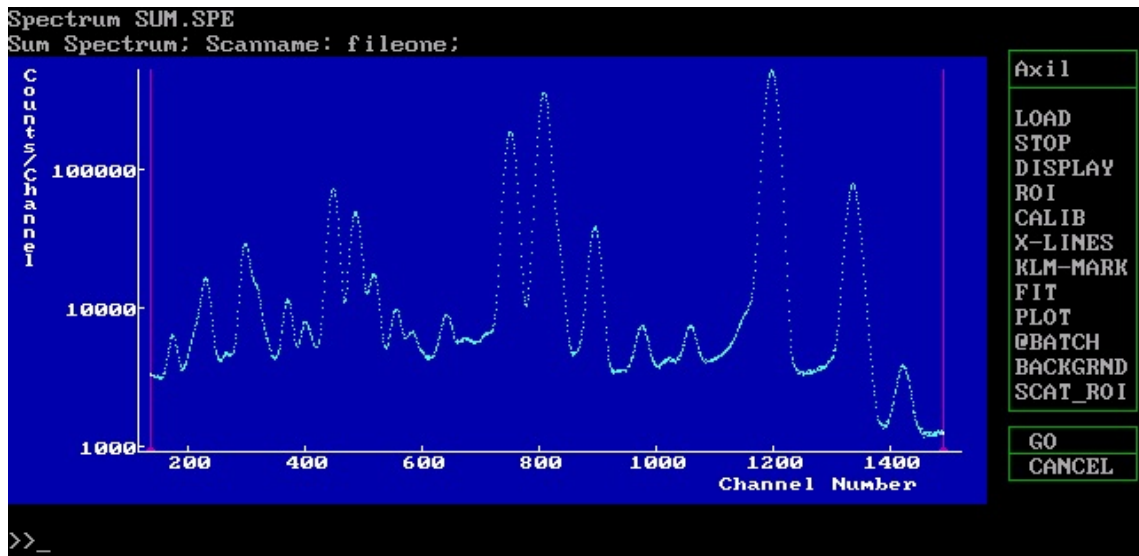
Figure 5.5: AXIL - only the ROI starting at 1000cts is displayed

5.3 CALIB

This function should be treated with caution, as one can easily falsify the measurements with a bad calibration. Usually this procedure is only performed if you have reason to believe, that there is something wrong with the current settings.

In order to perform a calibration, you need at least two peaks, where you are absolutely sure about the elment and caracteristic line! A useful tool to check for corresponding elements is the KLM-Marker. Shift through your spectrum, pick some distinctive peaks of which you are sure, that these elements have to be in your sample and remember them. If you are conducting measurements in air, Ar at 2,957eV is a good choice.

To start with the calibration process, enter **CALIB** and press **F1** in order to perform an energy calibration. A vertical yellow line should appear. Move it with the arrow keys until it coincides with the maximum of a peak, enter the corresponding line (FE-KA, FE-KB,...) and press space. Now select a second peak with the marker enter the element again and confirm your calibration with the **ENTER** key.
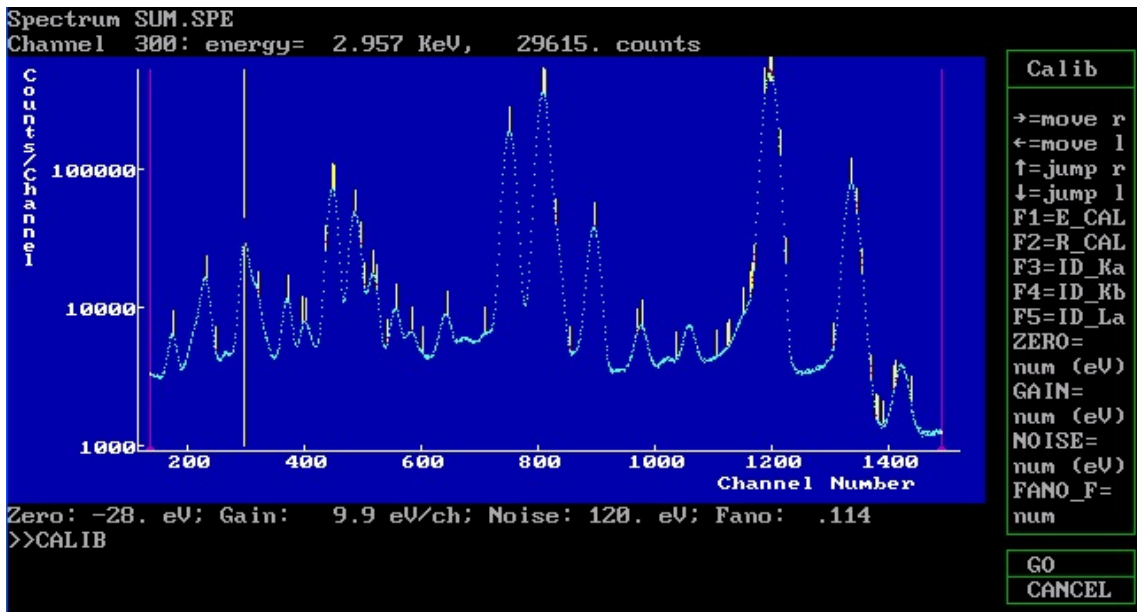
Figure 5.6: AXIL - calibration process with the yellow marker at the Ar peak

5.4 KLM-MARK

The KLM-Markers are selected by typing **KLM ENTER** and are useful to check the elemental correspondence of a peak. The vertical yellow lines that appear represent the $K\alpha, K\beta, L\alpha, L\beta, ...$ lines corresponding to the currently selected element, which you can cycle with the **LEFT** and **RIGHT** arrow keys. Be careful not to confuse escape or sum peaks with actual elements!
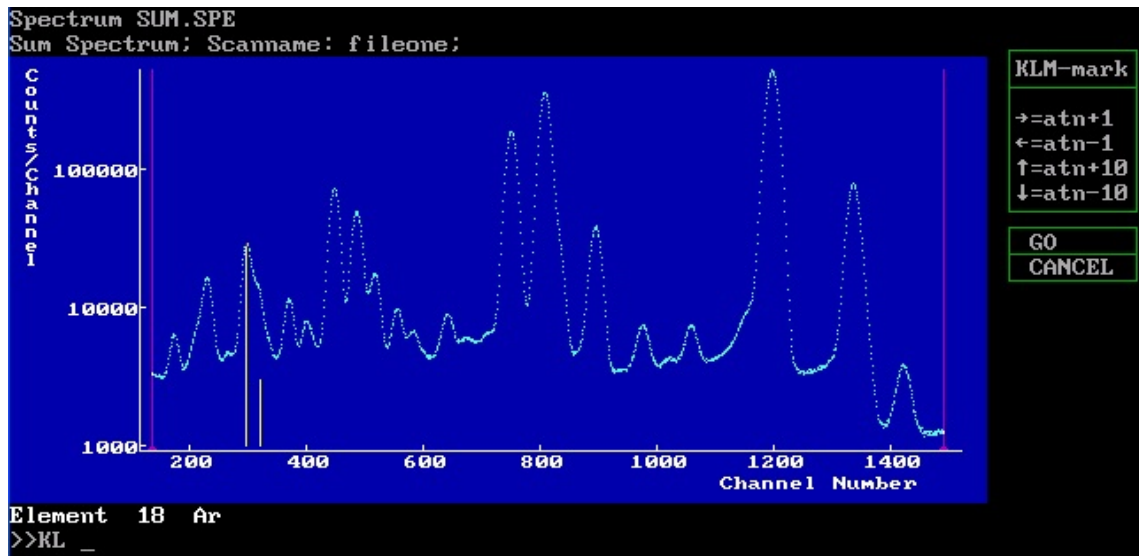
Figure 5.7: AXIL - KLM-Marker example of Ar ($K\alpha$ and $K\beta$)

5.5 X-LINES

The command **X-Lines** is used to specify which elements you wish to evaluate in your fit. You can check with the KLM-Markers which peak corresponds to which element and add it by pressing **X ADD** followed by the international element abbreviation. This way, the whole set of lines for this element will be included. It is also possible to include only a single line by adding the line name after the element, for example: FE-KA or CU-KB. In some cases this may yield better results.
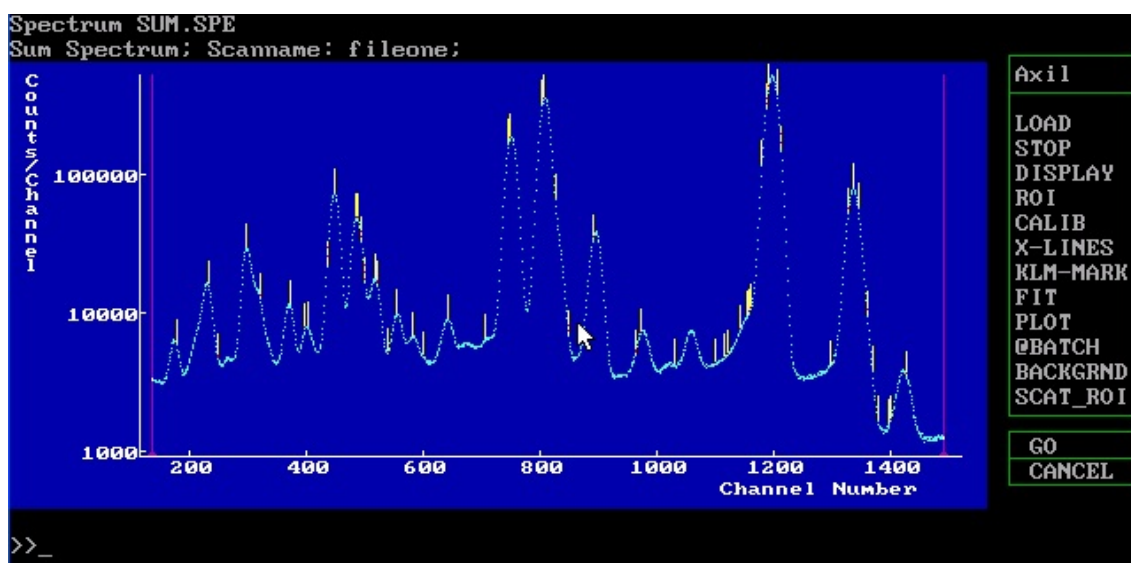
Figure 5.8: AXIL - example of several X-Lines added and represented as short yellow
  bars on top of the peaks

It is also possible to remove unneeded ones with the **REMOVE** command and
display a list with the **SHOW** function. Some special commands are needed to
add a sum or escape peak: **SUM Fe** to add the sum peak of iron and **Fe+** for the
escape peak.

```
Spectrum SUM.SPE
                                                              ┌─────────┐
═══════════════════════════════════════════════════════════  │  Show   │
                                                              ├─────────┤
           List of X-ray lines in the fitting model           │  <↑>    │
                                                              │  <↓>    │
Line group              energy        rel.int.                │ <Pg Up> │
                                                              │ <Pg Dn> │
   1 Si-K      KA1       1.740         1.000000                │ <Home>  │
                                                              │ <End>   │
   2 S -K      KA1       2.307          .941900                │ <Esc>   │
               KB1       2.464          .058100                ├─────────┤
                                                              │  GO     │
   3 Ar-K      KA1       2.957          .907400                │ CANCEL  │
               KB1       3.191          .092600                └─────────┘

   4 Ca-K      KA1       3.691          .888300
               KB1       4.013          .111700


═══════════════════════════════════════════════════════════

>>_
```

Figure 5.9: AXIL - list of X-ray lines in the fitting model with the corresponding designation, the energy and the relative intensity

5.6 BACKGRND

In order to correctly deconvolute the spectrum, proper background settings are required. There are three functions available: LINEAR, EXPONENTIAL and OR-THOGONAL POLYNOMIAL. They all have different parameters which you can set by typing **BACK PARAM=#**. You should always check your new setting with a fit, described in the next section.
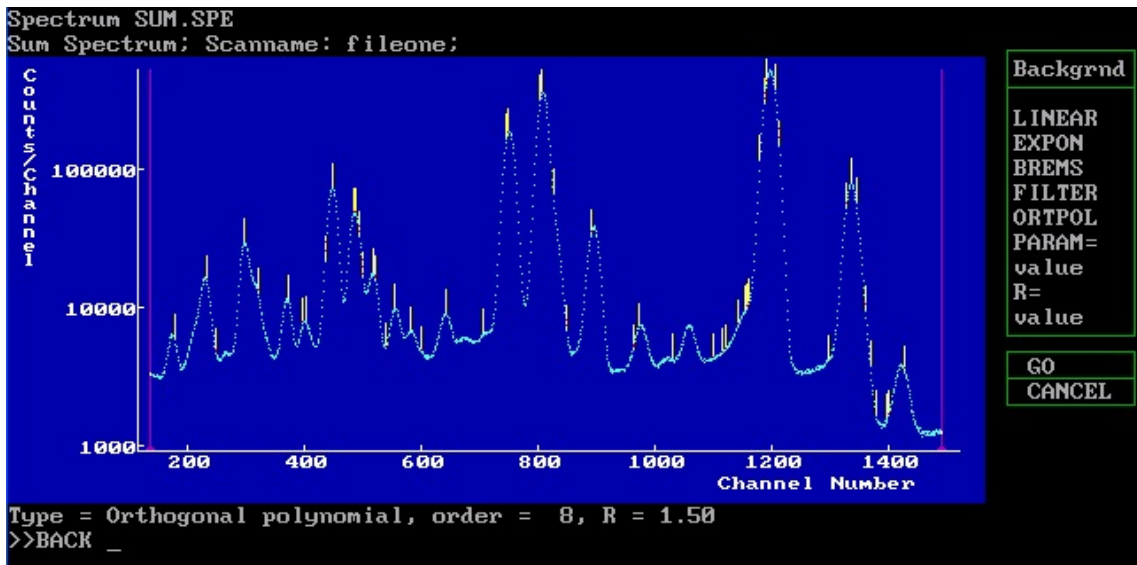
Figure 5.10: AXIL - BACKGRND menu options

5.7 FIT

When you are finished and satisfied with your settings it´s time to try a fit. Press **FIT N=##**, where ## represents the maximum number of iterations you´d like the program to conduct before stopping. 10 to 15 is usually a good number, but in most cases the fit will converge after 3-7 runs. After each iteration you can see the chi-square value and iteration number on the top of the screen. If you are not satisfied with your chi-square, try changing your background settings or adding X-Lines you might have missed, like sum, escape or overlapping peaks for deconvulution! You can also save the results of your current fit with **SAVE_RES** and **ENTER**.
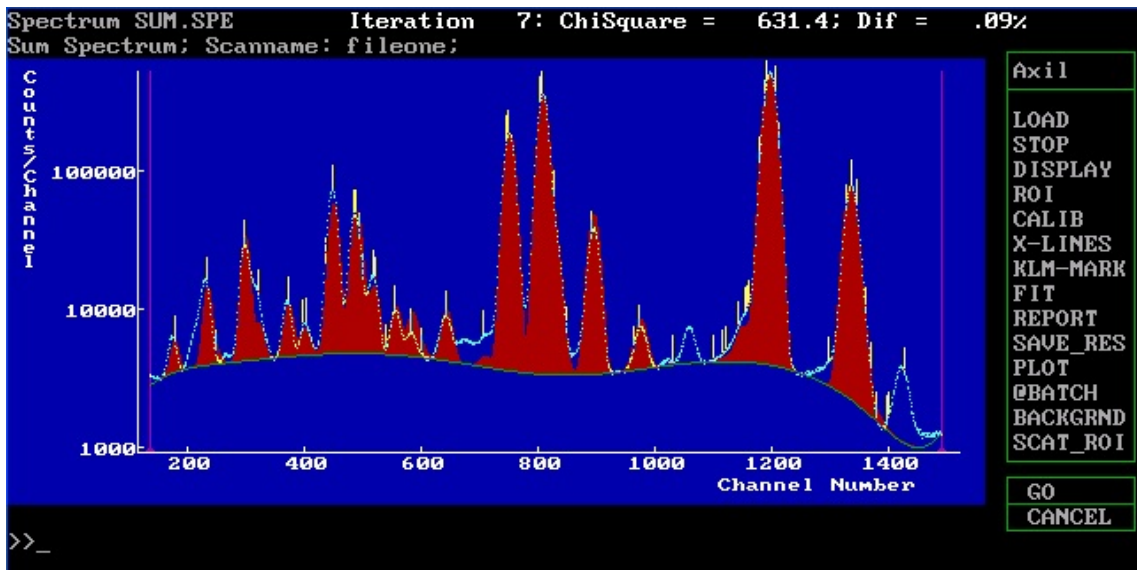
Figure 5.11: AXIL - Fitted spectrum, with information like the number of iterations, chi-square and the deviation between the last two iterations displayed on top

5.8 Save model

Once satisfied with your fit, you can save your current model, which will include the settings for your X-Lines, calibration, ROI, background and fitting. To do this you first have to go back one step by typing **STOP** and confirming it with **ENTER**. You now see a different menu, where you can select to save your model either in the current model file, a new one or an existing one. Just be careful not to overwrite a model you´d like to preserve!

Figure 5.12: AXIL - The current model file used can be seen on top and the user has the choice to save the current model or load an existing one.

5.9 Batch processing

As most measurements will consist of more than one spectrum, it is possible to automatically evaluate each one of them by using a so called batch file. In order to do this, it is necessary that you have selected the **D:\SampleName\spectra\spe** folder, containing all the .spe files and the fitall.bat file as your current working folder, as described at the beginning of this chapter. Now select spectrum fitting, AXIL (& Voigt peak profiles option for high energy K-lines), make sure your previously saved model is active and select analyse spectra.

A more or less empty black screen, with only a few commands will appear and as a last step you have to type **@BATCH FITALL.BAT** and press **ENTER**. The program will now evaluate all files according to your selected model and generate

.asr files containing the elemental information about all X-Lines specified, which you will need for further processing in MATLAB [5]. To speed up the process it is recommended to increase the emulated computer power by pressing **CTRL+F12**, but for stability reasons a maximum of about 30000 to 35000 cycles should not be exceeded. If you wish to decrease the speed again, press **CTRL+F11**.

Chapter 6

Graphical evaluation - MATLAB

6.1 Preparations

Before MATLAB [5] is started, the user has to copy the folder containing all files already evaluated by AXIL from the VM to the Windows 7 Computer. Simply right click the folder, select copy, then minimize the VM by clicking on the small underline symbol on top of the screen and finally paste the folder on the desktop or in any other location.

There should be three files located on the desktop called Datamove.m, Datamove3d.m and Xray.txt. These files contain the MATLAB program code for graphical evaluation and have to be copied into the same folder, where the .asr files are located. This should be '**...\samplename\spectra\spe**'.

6.2 Datamove.m & Datamove3d.m

The file Datamove3d.m is used for data evaluation of a measurement performed with a 3 mm stepsize. It will interpolate the data accordingly and generate a 2D map of the elemental distribution. If any other stepsize was utilized, the file Datamove.m has to be used for spectrum evaluation.

6.3 Data evaluation

In order for MATLAB to recognize the correct working directory, it is easiest to start it by double clicking on either Datamove.m or Datamove3d.m in your sample folder. The difference between these two files was already explained in section 6.2.

Once the program has finished loading, it should look like picture 6.1 below.
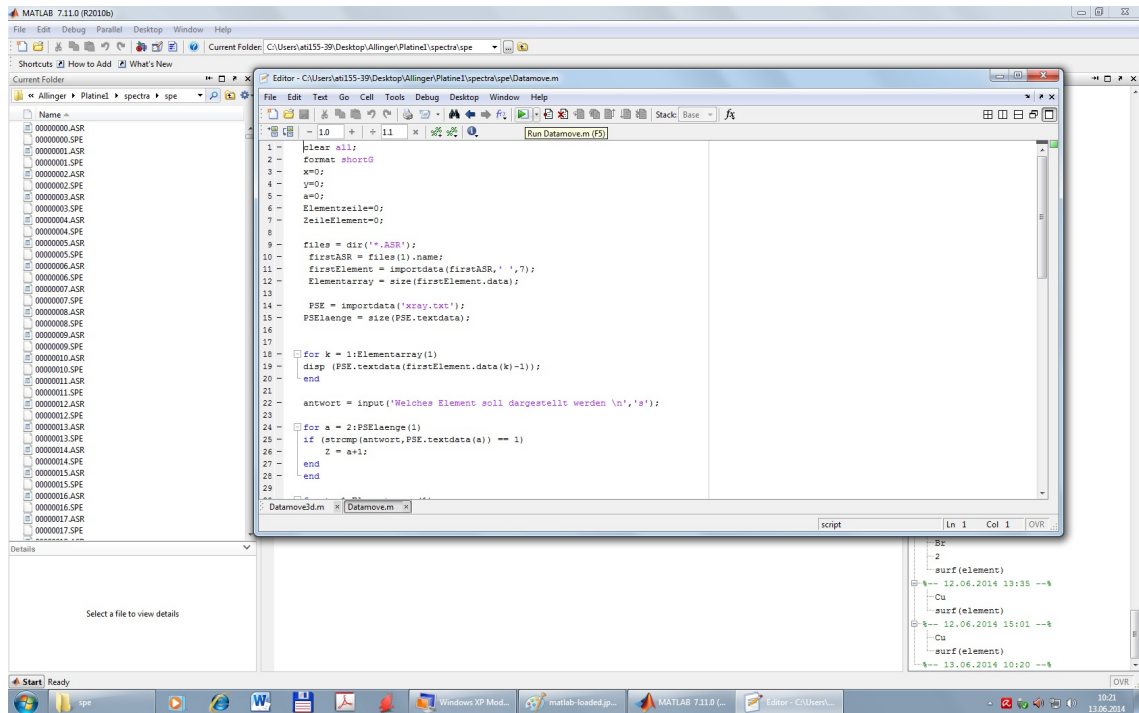
Figure 6.1: MATLAB - Freshly started session

To finally start the evaluation script, click on the green arrow symbol or press **F5**. MATLAB will now process the data and once finished, prompt for the element you´d like to display (see picture 6.2). *Hint: MATLAB is case sensitive, this means you should enter the element exactly as displayed above.* After entering the desired element, a new window will open, displaying a two dimensional color map correlating to the distribution of this element.
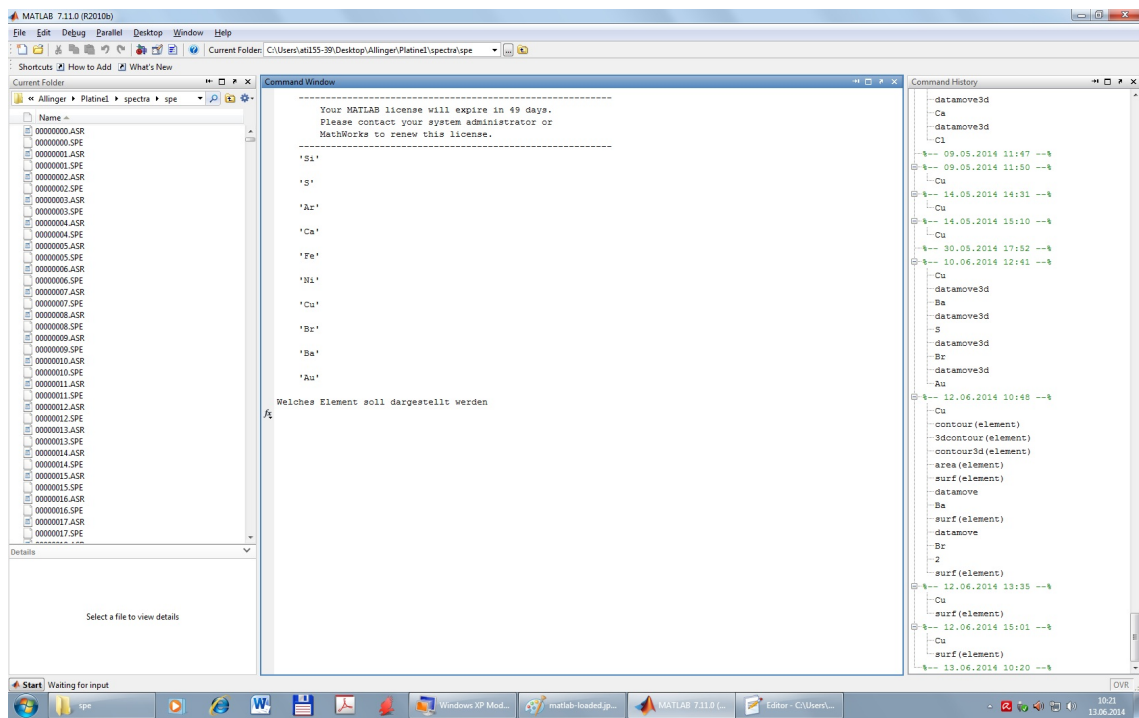
Figure 6.2: MATLAB - Requesting user input for element evaluation
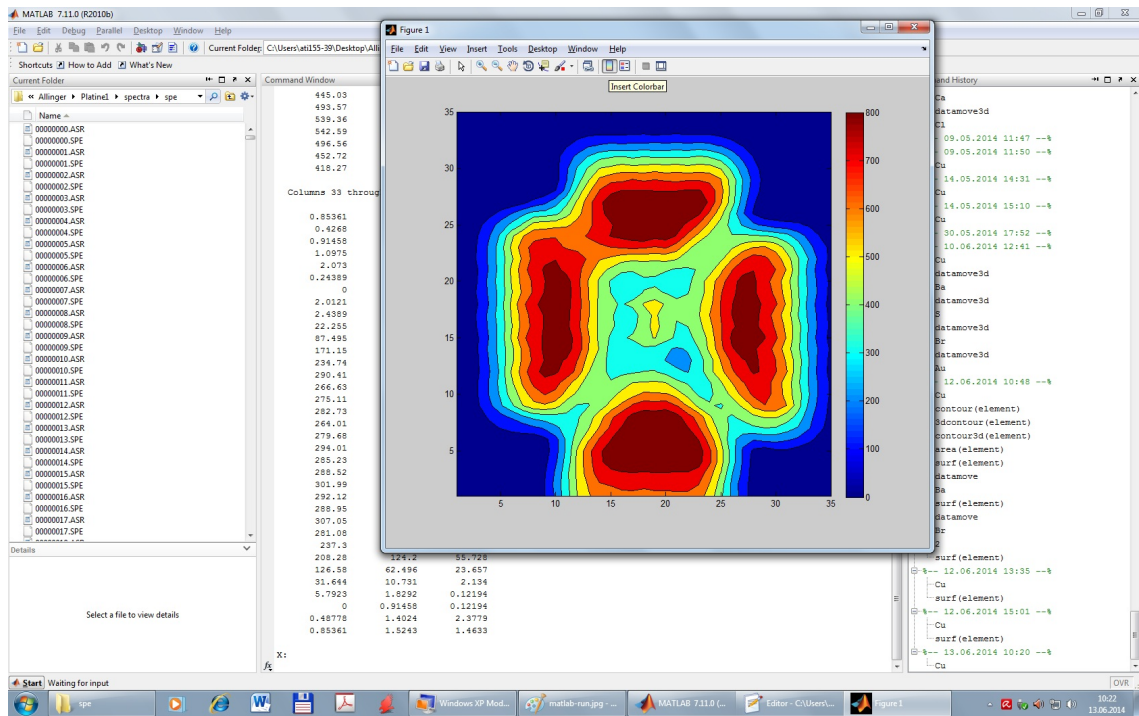
Figure 6.3: MATLAB - 2D color graph example

6.4 Modifying the graph

The graph can be modified just like any other diagram you might know from different programs. You can add a legend, axis labels or display the color bar for z-axis values. All of the settings, like grid thickness, axis standoff, x- and y-range, labels, colors,... can be adjusted with the property editor. For easier use, you can click on an item you´d like to change and then open the property editor. In this way the corresponding settings will already be selected. Once satisfied it is possible to save the current graph in several formats.

For an in depth documentation, please visit the website [5] or consult the Internet, there are many tutorials available on all topics in either text or video format.

Bibliography

[1] KETEK. AXAS-D, Analytical X-ray Acquisition System. `www.ketek.net`.

[2] Massimo Banzi and David Cuartielles. ARDUINO. `www.arduino.cc`.

[3] AMPTEK INC. Mini-X, Miniature X- Ray Source. `www.amptek.com`.

[4] XRF Group, IAEA laboratories Seibersdorf. Quantitative X-ray Analysis System. `www.iaea.org/OurWork/ST/NA/NAAL/pci/ins/xrf/pciXRFdown.php`.

[5] MATLAB. `www.mathworks.de/products/matlab/`.

Index